Transverse Λ polarization from a transversely polarized proton target at the COMPASS experiment

vorgelegt von

Teresa Negrini

aus Bonn

Angefertigt mit Genehmigung der Mathematisch–Naturwissenschaftlichen Fakultät
der Rheinischen Friedrich–Wilhelms–Universität Bonn

Diese Dissertation ist auf dem Hochschulschriftenserver der ULB Bonn
$http://hss.ulb.uni-bonn.de/diss\_online$ elektronisch publiziert.

1. Gutachter: Prof. Dr. J. Bisplinghoff

2. Gutachter: Prof. Dr. K. Maier

Tag der Promotion: 17.12.2009

Erscheinungsjahr: 2010

Abstract

The measurement of the transverse spin quark distribution functions $\Delta_T q(x_{Bj})$ is an important part of the physics program of the COMPASS experiment at CERN. These transversity distributions, being chiral-odd objects, are not accessible in inclusive deep-inelastic scattering (DIS), requiring the presence of another chiral-odd object. At COMPASS, $\Delta_T q(x_{Bj})$ can be measured in semi-inclusive deep-inelastic scattering (SIDIS), where a promising channel is the spin transfer to the Λ hyperons. Here, the fragmentation functions $\Delta_T D_q^\Lambda(z)$ provide the other chiral-odd object. In this thesis, the semi-inclusive Λ production mechanism is introduced to show the connection between a potentially measured Λ polarization P_Λ and the $\Delta_T q(x_{Bj})$ functions. An expression for the angular distribution of the weak decay $\Lambda \to p\pi^-$ is used which allows to extract P_Λ independent of acceptance effects of the spectrometer. In 2007 a 160 GeV/c longitudinally polarized muon beam and a transversely polarized NH_3 target were employed in the COMPASS experiment. Based on the full 2007 statistics with transverse target spin configuration, the Λ and $\overline{\Lambda}$ polarizations are analyzed as a function of x_{Bj} and z. The Λ and $\overline{\Lambda}$ hyperons are unpolarized within their statistical errors and show no dependence on either x_{Bj} or z.

Contents

Chapter 1

Introduction

The atomic nucleus consists of nucleons, the protons and neutrons. During the mid 1960s it became clear that the nucleons are not the elementary particles they were assumed to be, which means that they are not fundamental constituents of the nucleus. Protons and neutrons have their own inner structure, i.e. they are built out of even smaller particles, the quarks. Baryons for example are particles which are made up of three quarks and carry a half-integer spin, while mesons are particles with an integer spin and made of a quark-antiquark pair. Both, baryons and mesons are members of a larger family comprising all particles which are made of quarks, the strongly interacting hadrons. A hyperon is a member of the baryon family and contains one or more strange quarks, but no charm or bottom quarks. The lightest hyperon, the Λ hyperon, consists of each a u quark, a d quark and a s quark.

The properties of the nucleons and hyperons at low energies can be described by the Quark Parton Model (QPM) in which a baryon consists of three constituent quarks. Each of those quarks possesses a mass of approximately one third of the baryon mass. The proton consists of two u quarks with charge $+2/3e$ and one d quark with charge $-1/3e$. The neutron consists of two d quarks and one u quark. In the QPM, the u quarks have a spin $1/2$ in the upwards, the d quarks a spin $1/2$ in the downwards direction. Quarks are described as fundamental, point-like particles with no inner structure, whose interactions take place through the exchange of vector bosons, the gluons, in strong interaction. The quarks were first introduced by M. Gell-Mann [1] and G. Zweig [2] and later described in the QPM framework as so-called partons by R. Feynman [3]. This simplifying picture had to be modified to accommodate an abundance of fluctuating quark-antiquark pairs (sea quarks) and gluons which bind the valence quarks by strong interaction. Thus, the QPM was extended to include a Quantum Chromodynamic (QCD) description for the strong interaction between the partons via the exchange of gluons.

The inner structure of the nucleon can be investigated experimentally by scattering a high-energy beam of leptons off a target nucleon. When the incident lepton beam energy is high compared to the nucleon mass it is then possible to glance into the

internal structure of the nucleon. Thus, the acquisition of the first data on polarized deep-inelastic scattering (DIS) with a large momentum transfer kindled the interest towards further exciting discoveries of the nucleon structure. It was quite a surprise when the EMC experiment published in 1988 that only a small fraction ($\Delta\Sigma = 0.12 \pm 0.09 \pm 0.14$) of the proton spin originates from the spins of the three constituent quarks [4, 5], contradicting the QPM. This "nucleon spin crisis" urged further intense experimental and theoretical investigations in an attempt to find the missing components of the nucleon spin. Several DIS experiments on protons, deuterons and ^{3}He (SMC at CERN, E143, E155 at SLAC, and HERMES at DESY) have confirmed the original EMC discovery, establishing a spin contribution of the quarks to the nucleon spin, $\Delta\Sigma$, between 25 % and 30 %. So, which other components of the nucleon could be responsible to carry part of the nucleon spin? A relation was derived [6] to include components which were neglected before,

$$S_N = \frac{1}{2} = \frac{1}{2}\Delta\Sigma + \Delta G + L_q + L_g.$$

This equation states that the total nucleon spin must arise from a combination of three distinct sources,

- The spin distribution of the quarks ($\Delta\Sigma$)

- The spin distribution of the gluons (ΔG)

- The orbital angular momenta of quarks and gluons (L_q, L_g)

The quark spin contribution can be further split up and assigned to different quark flavours, i.e. $\Delta\Sigma = \Delta u + \Delta\overline{u} + \Delta d + \Delta\overline{d} + \Delta s + \Delta\overline{s}$. The contributions of charm or heavier quarks is anticipated to be very small and is, thus, neglected. In a recent publication it has indeed been shown that the largest contribution to the nucleon spin stems from the valence u and d quarks, while the polarizations of the sea quarks, $\Delta\overline{u}$ and $\Delta\overline{d}$, are all consistent with zero [7].

It was found in the early 1980s that three functions are needed to explain the spin structure of the nucleon in leading order, without considering quark transverse momenta. Those three functions have a probabilistic interpretation in the QPM and are conventionally named $q(x_{Bj})$, $\Delta q(x_{Bj})$ and $\Delta_T q(x_{Bj})$. The first one depicts the distribution of unpolarized quarks in an unpolarized nucleon, whereas the second function gives the distribution of helicity of a longitudinally polarized parent nucleon among the quarks. The third one, the so-called transversity distribution function $\Delta_T q(x_{Bj})$ was at first assumed to be negligible in the DIS domain, since the interpretation in the QPM is usually given in a framework where the nucleon is boosted in the longitudinal direction. This implicitly states that effects connected to transverse spin and transverse quark momenta are negligible. However, in the infinite momentum frame with the nucleon spin transverse to the direction of motion, the transversity distribution $\Delta_T q(x_{Bj})$ quotes the number of quarks with their spin

aligned in the transverse direction parallel to the nucleon spin minus the number of quarks with their spin aligned antiparallel to the nucleon spin. In the rest frame of the nucleon, the probability to find a quark spin aligned along the nucleon spin is not correlated with the orientation of the nucleon spin. However, if the nucleon is boosted to a very high momentum in the direction of its spin, the alignment probability corresponds to the helicity distribution. The transversity distribution is an independent property which cannot be found, e.g., through rotational transformation of the helicity distribution. Therefore, it is nowadays recognized as the missing crucial piece of information about the nucleon spin structure.

The importance of transverse spin effects at high energy in hadronic physics was first recognized in 1976 through the stunning discovery that Λ hyperons were produced polarized in unpolarized collisions of a 300 GeV proton beam on various targets (Be, and p) at the E8 experiment at Fermilab [8]. This behaviour was completely unexpected and impossible to explain with so far existing models. Nevertheless, the transversity distribution was not known until 1979 when Ralston and Soper [9] explained its behaviour in their study of Drell-Yan spin asymmetries for transversely polarized baryons. Due to the chiral structure of $\Delta_T q(x_{Bj})$ a measurement in the DIS domain is impossible, which is a reason for the scarce experimental data on these important functions. Instead, semi-inclusive deep-inelastic scattering (SIDIS) has to be used where another chiral-odd coupling partner is provided and where at least one hadron in the final state must be detected. This other chiral-odd coupling partner is the fragmentation function $\Delta_T D_q^\Lambda(z)$ in SIDIS. Here, the understanding of the hadronization mechanism is crucial for the interpretation of SIDIS. In the 1990s the experimental and theoretical interest in transversity was kindled anew [10, 11].

An intriguing way to gather complementary information on the transverse polarization of quarks and antiquarks is the investigation of the hadronization of transversely polarized quarks into transversely polarized Λ hyperons. The weak decay of the Λ hyperon, $\Lambda \rightarrow p\pi^-$, has the unique feature of a "self-analyzing" decay, which means that the angular distribution of the Λ decay products is strictly correlated to the Λ polarization. The asymmetry of the Λ decay $\alpha = 0.64$ is rather large. At the same time, the Λ decay is experimentally easily accessible through detection of its two daughter particles p and π^- with a large enough branching ratio of this decay of 64 %.

COMPASS is a fixed target experiment at the SPS M2 beamline at CERN. Two of the most important experimental investigations, which COMPASS is designed to tackle, are a precision measurement of the gluon contribution towards the nucleon spin, ΔG, and the measurement of the transverse spin effects, specifically extracting the transverse polarized quark distribution functions $\Delta_T q(x_{Bj})$. At COMPASS, transverse spin effects were measured for the first time on a deuteron target in 2002-2004.

In the presented thesis, the Λ and $\overline{\Lambda}$ polarizations are extracted from the data

which were recorded in 2007 at COMPASS with a longitudinally polarized 160 GeV muon beam and a transversely polarized proton target. The theory of transverse Λ polarization is reviewed in Chapter 2, introducing the factorization of the SIDIS process into distribution and fragmentation functions and explaining the method to extract the Λ polarization from the data. A detailed description of the COMPASS spectrometer and the data acquisition system is given in Chapter 3. In Chapter 4 the selection procedure as well as kinematic observations of the final Λ and $\overline{\Lambda}$ sample are shown. The results of this analysis along with systematic studies on data stability are presented in Chapter 5, and the extracted Λ and $\overline{\Lambda}$ polarizations are discussed in Chapter 6. The summary and outlook in Chapter 7 complete this thesis.

Chapter 2

Transverse Λ Polarization

2.1 Polarized Deep-Inelastic Scattering

One aim at the COMPASS experiment is to investigate the transverse spin structure
of the nucleon by looking at semi-inclusive deep-inelastic scattering reactions of
muons on a polarized nucleon target. The nucleon spin is composed of the spins of
valence quarks, sea quarks, gluons, and their orbital angular momenta. The nucleon
spin S_N in units of $\hbar$ is expressed in [6] as

$$S_N = \frac{1}{2} = \frac{1}{2}\Delta\Sigma + \Delta G + L_q + L_g, \tag{2.1}$$

where $\Delta\Sigma$ contains the sum of the spin contributions from quarks and antiquarks,
ΔG contains the spin contribution from gluons, L_q is the contribution from the
orbital angular momenta of quarks and L_g is the contribution from the orbital an-
gular momenta of gluons. The deep-inelastic scattering (DIS) technique plays an
important role to gain knowledge about the different contributions. The theoretical
background presented in this chapter is analogous to [12].

To obtain knowledge on the spin structure of hadrons, longitudinally polarized lep-
tons are scattered off target nucleons which are either longitudinally or transversely
polarized. Consider a DIS event as shown in Fig. 2.1, where a charged lepton l is
scattered inelastically off a nucleon N with a large momentum transfer,

$$l(k) + N \rightarrow l'(k') + X. \tag{2.2}$$

In this scattering process a virtual vector boson is exchanged between the lepton
and one of the partons inside the target nucleon. The high four-momentum which is
exchanged leads to breaking up the nucleon and a final hadronic state X is formed.
This process is called inclusive DIS when only the final lepton l' is detected. In a
semi-inclusive DIS process, at least one of the produced hadrons is detected,

$$l(k) + N \rightarrow l'(k') + h(P_h) + X. \tag{2.3}$$

When the final hadronic state X is fully reconstructed, the event is called exclusive.

2.1.1   Kinematics
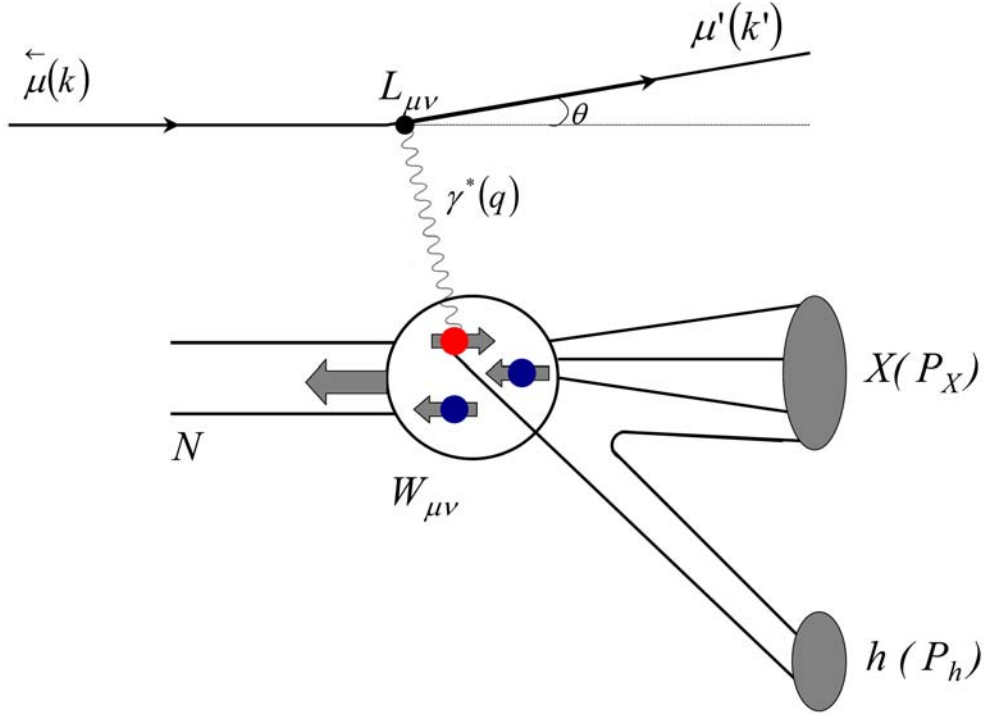
Figure 2.1: Overview of a deep-inelastic muon-nucleon scattering process.

An example for a muon-nucleon DIS process is illustrated in Fig. 2.1. The kinematic quantities necessary to quantify the process will be explained in the following paragraphs.

The squared momentum transfer Q^2 is a measure for the spatial resolution of the process. In the DIS domain, Q^2 is in the order of 1 to 100 $(\text{GeV/c})^2$ and, thus, large enough to resolve the constituents of the nucleons. The cross section is expressed as a function of the negative squared four-momentum transfer Q^2 and the energy loss ν of the scattered particle. The four-momentum squared of the virtual photon is given by

$$q^2 = (k - k')^2, \tag{2.4}$$

where k and k' denote the lepton four-momentum of the incoming and scattered muon, respectively. The angle between the incoming and scattered muon in the laboratory system is given by θ. Neglecting the lepton rest mass gives

$$-q^2 = Q^2 \cong 4EE' \sin^2 \frac{\theta}{2}, \tag{2.5}$$

where E and E' are the energy of the incoming and scattered lepton, respectively. The energy transfer from the virtual photon to the nucleon is given by

$$\nu = \frac{P \cdot q}{M} = E - E'. \tag{2.6}$$

In the case of the COMPASS experimental setup, the target nucleon with mass M is at rest in the laboratory frame. Therefore, the four-momentum of the target nucleon is given by $P = (M, \vec{0})$ and the invariant mass squared of the hadronic final state W^2 is given as

$$W^2 = (P + q)^2 = M^2 + 2M\nu - Q^2. \tag{2.7}$$

Events in the DIS domain are characterized by a value of $1/Q$ which is smaller than the size of the nucleon, resulting in the leptons scattering off a single parton. Additionally, W^2 has to be larger than $4\ (\mathrm{GeV/c^2})^2$ to ensure a complete break-up of the nucleon instead of forming hadronic resonances.

To fully describe a DIS process, another two dimensionless scaling variables are necessary. The Bjorken scaling variable x_{Bj} is a measure for the inelasticity of the scattering process. It can be considered as the fractional momentum of the target nucleon carried by the struck quark for large values of Q^2, and ranges between 0 and 1. In an elastic process, the target remains intact which results in $x_{Bj} = 1$. The variable y is identified with the energy fraction of the projectile transferred from the incoming lepton to the nucleon.

$$x_{Bj} = \frac{Q^2}{2P \cdot q} = \frac{Q^2}{2M\nu} \tag{2.8}$$

$$y = \frac{P \cdot q}{P \cdot k} = \frac{\nu}{E} \tag{2.9}$$

Additional kinematic variables, z and x_F, are used to characterize each detected hadron in processes of semi-inclusive deep-inelastic scattering. These variables will be introduced in the context of semi-inclusive Λ production later in this chapter. All kinematic quantities which are important in this analysis are summarized in Table 2.1.

2.1.2 Cross Sections

The differential cross section of lepton-nucleon scattering to detect the final lepton in the solid angle $d\Omega$ and in the final energy range $(E', E' + dE')$ in the laboratory frame can be calculated by contracting the leptonic tensor $L_{\mu\nu}$ and the hadronic tensor $W^{\mu\nu}$, as shown in [13],

$$\frac{d^2\sigma}{dE'd\Omega} = \frac{\alpha^2}{2Mq^4}\frac{E'}{E}L_{\mu\nu}W^{\mu\nu}, \tag{2.10}$$

Kinematic quantity	Description
$Q^2 = -q_\mu q^\mu \overset{lab}{\approx} 4EE' \sin^2 \frac{\theta}{2}$	Squared momentum transfer
$W^2 = (P^\mu + q^\mu)^2 \overset{lab}{=} M^2 + 2M\nu - Q^2$	Squared mass of the hadronic final state
$\nu = \frac{P_\mu q^\mu}{M} \overset{lab}{=} E - E'$	Energy transfer from lepton to target nucleon
θ	Lepton scattering angle in laboratory system
$s = (P^\mu + k^\mu)^2 \overset{lab}{=} 2ME + M^2$	Squared center-of-mass energy
$q^\mu = k^\mu - k'^\mu = (\nu, \vec{q})$	Four-momentum transfer to the target
$x_{Bj} = \frac{Q^2}{2P_\mu q^\mu} \overset{lab}{=} \frac{Q^2}{2M\nu}$	Bjorken scaling variable
$y = \frac{P_\mu q^\mu}{P_\mu k^\mu} \overset{lab}{=} \frac{\nu}{E}$	Fractional energy transfer to the nucleon
$P_h^\mu = (E_h, \vec{p_h})$	Four-momentum of a detected final state hadron h
$P_{||}^* = \vec{P_h^*} \cdot \frac{\vec{q^*}}{|\vec{q^*}|}$	Longitudinal momentum of the hadron h in the $\gamma^* N$ center-of-mass system
$x_F = \frac{P_{||}^*}{|\vec{q^*}|} \cong \frac{2P_{||}^*}{W}$	Feynman scaling variable
$z = \frac{P_\mu P_h^\mu}{P_\mu q^\mu} \overset{lab}{=} \frac{E_h}{\nu}$	Fraction of the virtual photon energy carried by a hadron h

Table 2.1: Kinematic variables used to describe a DIS process; the lower 4 quantities are descriptive of semi-inclusive DIS processes, respectively. The label "lab" denotes the laboratory frame in case of a fixed target experiment, neglecting the lepton mass.

where Ω is the solid angle in the laboratory frame and $\alpha = \frac{1}{137}$ is the electromagnetic fine-structure constant. The differential cross section can also be formulated as

$$\frac{2\pi M\nu}{E'} \frac{d^2\sigma}{dE'd\Omega} = \frac{d^2\sigma}{dx_{Bj}dy} = x_{Bj}(s - M^2)\frac{d^2\sigma}{dx_{Bj}dQ^2}, \qquad (2.11)$$

where s denotes the center-of-mass energy squared of the lepton-nucleon system. By using the Dirac matrices γ_μ and spinors $u, \overline{u}$, the tensor $L_{\mu\nu}$ which describes the interaction at the leptonic vertex in the 1-photon exchange can be expressed as

$$L_{\mu\nu}(k, k', s) = \sum_{s'} \overline{u}(k', s')\gamma_\mu u(k, s)\overline{u}(k, s)\gamma_\nu u(k', s'). \qquad (2.12)$$

The muon displays behaviours which can be understood in relation to an intrinsic angular momentum, the muon spin. The incoming muon is described by its spin four-vector s^ν by

$$s^\nu = \frac{1}{2m}\overline{u}(k, s)\gamma^\nu \gamma^5 u(k, s), \qquad (2.13)$$

where in the rest frame of the particle it is chosen to be $s^\nu = (0, \vec{s})$ and m is the mass of the muon. This normalization results for the spin vector s to be dimensionless. Summing over the lepton spins of the final state results in the expressions

$$
\begin{aligned}
L_{\mu\nu}(k, k', s) &= Tr\left[(\not{k}' + m)\gamma_\nu(\not{k} + m)\frac{m + \gamma_5\not{s}}{2m}\gamma_\mu\right] \\
&= 2(k_\mu k'_\nu + k_\nu k'_\mu - (kk' - m^2)g_{\mu\nu}) + 2im\epsilon_{\mu\nu\alpha\beta}s^\alpha(k - k')^\beta \\
&\approx 2(k_\mu k'_\nu + k_\nu k'_\mu - kk'g_{\mu\nu}) + 2im\epsilon_{\mu\nu\alpha\beta}s^\alpha(k - k')^\beta \\
&= L_{\mu\nu}^{(S)}(k, k') + L_{\mu\nu}^{(A)}(k, k', s)
\end{aligned}
\tag{2.14}
$$

where $g_{\mu\nu}$ is the metric tensor and $\epsilon_{\mu\nu\alpha\beta}$ is the antisymmetric Levi-Civita tensor [14]. The spin-independent components of the leptonic tensor $L_{\mu\nu}$ are symmetric, as indicated by (S), while the spin-dependent terms are antisymmetric, denoted by (A), when the μ and ν indices are exchanged. The leptonic tensor can be exactly computed in QED, while this is not possible for the hadronic tensor $W_{\mu\nu}$ due to the complex inner structure of the nucleon. Therefore, a parameterization of the hadronic tensor is given by a set of structure functions F_1, F_2, g_1 and g_2, which contain the momentum and spin distribution functions, respectively. The symmetric part of the hadronic tensor $W^{\mu\nu}$ can be expressed through two dimensionless structure functions $F_1(x_{Bj}, Q^2)$ and $F_2(x_{Bj}, Q^2)$ when symmetry arguments such as the Lorentz invariance, gauge invariance and the symmetry of the strong interaction under charge and parity transformation are applied. In the same way, the antisymmetric part of the hadronic tensor is parametrized by two other dimensionless structure functions $g_1(x_{Bj}, Q^2)$ and $g_2(x_{Bj}, Q^2)$ such that

$$
W^{\mu\nu}(P, q, S) = W_{(S)}^{\mu\nu} + W_{(A)}^{\mu\nu}, \tag{2.15}
$$

with

$$
\begin{aligned}
W_{(S)}^{\mu\nu}(P, q) &= \left(-g^{\mu\nu} + \frac{q^\mu q^\nu}{q^2}\right)F_1(x_{Bj}, Q^2) + \\
&\quad \left(P^\mu - \frac{P_\lambda q^\lambda}{q^2}q^\mu\right)\left(P^\nu - \frac{P_\lambda q^\lambda}{q^2}q^\nu\right)\frac{F_2(x_{Bj}, Q^2)}{P_\lambda q^\lambda},
\end{aligned}
\tag{2.16}
$$

$$
\begin{aligned}
W_{(A)}^{\mu\nu}(P, q, S) &= iM\epsilon^{\mu\nu\rho\sigma}q_\rho \cdot \left[\frac{S_\sigma}{P_\lambda q^\lambda}g_1(x_{Bj}, Q^2)\right] + \\
&\quad iM\epsilon^{\mu\nu\rho\sigma}q_\rho \cdot \left[\frac{S_\sigma(P_\lambda q^\lambda) - P_\sigma(S_\lambda q^\lambda)}{(P_\lambda q^\lambda)^2}g_2(x_{Bj}, Q^2)\right].
\end{aligned}
\tag{2.17}
$$

The differential cross section as given in Eq. 2.10 results from combining the expressions for the leptonic tensor $L_{\mu\nu}$ and hadronic tensor $W^{\mu\nu}$. The unpolarized

and, thus, spin-independent cross section can be extracted from the contraction of the symmetric parts of $L_{\mu\nu}$ and $W^{\mu\nu}$. In the same way the antisymmetric parts can be contracted to find the polarized cross section. The spin-independent and spin-dependent cross sections are

$$\frac{d^2\sigma}{dE'd\Omega} = \frac{4\alpha^2 E'^2}{Q^4}\left[\frac{2F_1(x_{Bj},Q^2)}{M}\sin^2\frac{\theta}{2} + \frac{F_2(x_{Bj},Q^2)}{\nu}\cos^2\frac{\theta}{2}\right] \qquad (2.18)$$

$$\frac{d^2\Delta\sigma}{dE'd\Omega} = \frac{4\alpha^2}{Q^2 M\nu}\frac{E'}{E}\left[(E + E'\cos\theta)\cdot g_1(x_{Bj},Q^2) - \frac{Q^2}{\nu}\cdot g_2(x_{Bj},Q^2)\right] \qquad (2.19)$$

where $\Delta\sigma = \sigma^{\overrightarrow{\Leftarrow}} - \sigma^{\overrightarrow{\Rightarrow}}$ expresses the difference in the cross sections for the nucleon spin antiparallel and parallel with respect to the beam spin direction. In the case of longitudinally polarized leptons, either with their spin in the direction along ($\rightarrow$) or opposite ($\leftarrow$) to the direction of motion, the nucleons at rest are polarized along ($\Rightarrow$) or opposite ($\Leftarrow$) with respect to the incoming lepton direction of motion. The spin-dependent cross section depends on the polarized structure functions g_1 and g_2. The relevant variables of the structure functions are x_{Bj} and Q^2.

2.2   Quark Parton Model

In 1969, Richard Feynman proposed the Quark Parton Model (QPM) as a way to analyze high-energy hadron collisions [15]. He applied the QPM to electron-proton deep-inelastic scattering [16]. In the QPM, a hadron, such as a proton, is composed of a number of non-interacting point-like constituents, the so-called partons. In high-energy collisions it is a valid approximation to assume that the hadron is in a reference frame where it has infinite momentum. This allows to consider the partons as massless and moving parallel to the nucleon, neglecting the transverse component of the parton momenta. The QPM describes DIS processes on a nucleon as the sum of incoherent elastic scattering amplitudes on partons. The partons were later matched to be quarks and gluons.

The nucleon's reference frame of infinite momentum results in negligible rest masses as well as negligible transverse momenta with respect to the direction of motion of the partons. The partons carry a fraction of the four-momentum of the nucleon x_{Bj}. In leading order the electrically neutral gluons do not interact with the virtual photon, thus, only quarks are coupled to the virtual photon. The momentum transfer Q^2 of the photon needs to be sufficiently large in order to resolve individual partons. In the QPM the limits $Q^2 \rightarrow \infty$ and $\nu \rightarrow \infty$ are applicable which leads to the fact that the structure functions do not depend on Q^2 but are a function of $x_{Bj} = Q^2/2M\nu$ only. The structure functions in the QPM are expressed as

$$
\begin{aligned}
F_1(x_{Bj}) &= \frac{1}{2} \cdot \sum_f e_f^2 \left(q_f(x_{Bj}) + \bar{q}_f(x_{Bj}) \right), \\
F_2(x_{Bj}) &= x_{Bj} \cdot \sum_f e_f^2 \left(q_f(x_{Bj}) + \bar{q}_f(x_{Bj}) \right), \\
g_1(x_{Bj}) &= \frac{1}{2} \cdot \sum_f e_f^2 \left(\Delta q_f(x_{Bj}) + \Delta \bar{q}_f(x_{Bj}) \right), \\
g_2(x_{Bj}) &= 0,
\end{aligned}
\tag{2.20}
$$

where e_f denotes the fractional charge of the quark flavour f. By summing over the flavours of quarks and antiquarks the presented formalism in the QPM, therefore, leads to the definition of the structure functions F_1, F_2, g_1 and g_2. The correlation between F_1 and F_2 is stated in the Callan-Gross relation [17], which is a consequence of the spin 1/2 of quarks,

$$
F_2(x_{Bj}) = 2x_{Bj}F_1(x_{Bj}). \tag{2.21}
$$

The distributions $q(x_{Bj})$ are the unpolarized parton density functions (or quark distribution functions), and $\Delta q(x_{Bj})$ are the polarized quark distribution functions, which are defined as probability distributions with their respective fraction x_{Bj} ranging from 0 to 1. The probabilistic definition of the unpolarized quark distribution function $q(x_{Bj})$ is the sum over the quark distribution functions with parallel and antiparallel quark spin, while the polarized quark distribution function $\Delta q(x_{Bj})$ is given as the difference between the quark distribution functions with parallel and antiparallel quark spin,

$$
\begin{aligned}
q(x_{Bj}) &= q^{\rightarrow}(x_{Bj}) + q^{\leftarrow}(x_{Bj}), \\
\Delta q(x_{Bj}) &= q^{\rightarrow}(x_{Bj}) - q^{\leftarrow}(x_{Bj}).
\end{aligned}
\tag{2.22}
$$

The polarized and unpolarized parton distribution functions (PDFs) can be interpreted as the probability to find a polarized and an unpolarized quark of a certain flavour with the fractional momentum x_{Bj} in the nucleon. In the domain of DIS, only the combined contribution of both quarks and antiquarks to the spin can be derived. The total momentum carried by quarks is given by the integral over the unpolarized parton density function. In earlier experiments it has been found that the nucleon momentum is not completely carried by quarks - gluons carry about one half of the momentum of the nucleon [14]. Accordingly the integration over x_{Bj} of the polarized quark distribution function in the nucleon reveals the fraction of the nucleon spin which is carried by quarks,

$$
\Delta q = \int_0^1 \Delta q(x_{Bj}) dx_{Bj}. \tag{2.23}
$$
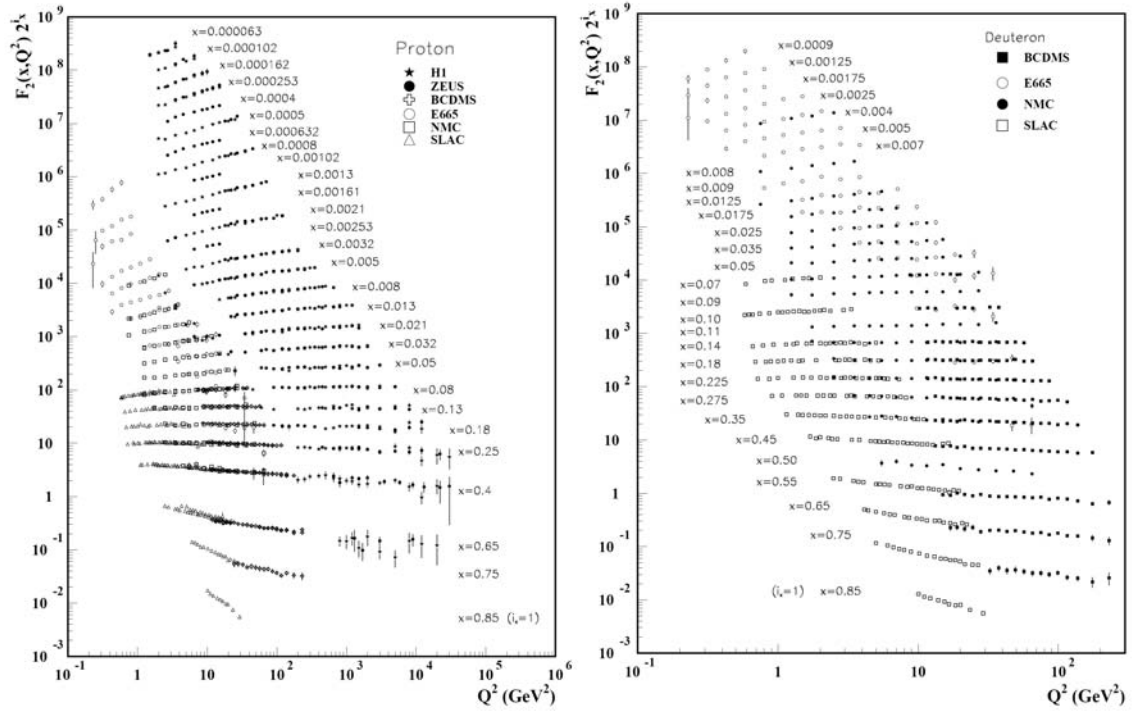
Figure 2.2: The unpolarized proton (left) and deuteron (right) structure function $F_2^{p,d}(x_{Bj}, Q^2)$ measured in deep-inelastic lepton-nucleon scattering at the following experiments: H1 [18], ZEUS [19], BCDMS [20], SLAC [21], E665 [22] and NMC [23]. For clarity, $F_2^{p,d}$ has been multiplied by 2^{i_x} where i_x is the number of the x_{Bj} bin. Statistical and systematic errors are shown. The data are plotted as a function of Q^2 for fixed values of x_{Bj}. The figure has been taken from [24].

A notable result regarding the unpolarized structure functions is the Bjorken scaling violation. The assumptions made for the QPM formalism were that the constituents of the nucleon were point-like and behaved like free particles. These assumptions lead to the fact that the structure functions in Eq. 2.20 do not depend on Q^2. This phenomenon is the Bjorken scaling. Now the experimental results for $F_2^p(x_{Bj}, Q^2)$ and $F_2^d(x_{Bj}, Q^2)$, presented in Fig. 2.2 as a function of Q^2 for several fixed values of x_{Bj}, show a dependence on Q^2. In the range $x_{Bj} < 0.05$ and $x_{Bj} > 0.3$ the structure function $F_2^p(x_{Bj}, Q^2)$ is significantly dependent on Q^2, a behaviour which is contradictory to the naive QPM. For small values of x_{Bj}, $F_2^p(x_{Bj}, Q^2)$ increases with increasing Q^2. A similar behaviour is observed for $F_2^d(x_{Bj}, Q^2)$. The opposite effect takes place at large values of x_{Bj}, where the structure function F_2 decreases with increasing Q^2.

When citing the polarized distribution functions it is important to keep in mind that they are necessarily exclusively in the DIS domain when the target nucleons and scattering leptons are polarized. The spin structure functions $g_1(x_{Bj}, Q^2)$ and $g_2(x_{Bj}, Q^2)$ are derived through photon-nucleon asymmetries A_1 and A_2 with

a longitudinally polarized lepton beam and either a longitudinally or a transversely polarized target, as in [25],

$$
A_1(x_{Bj}, Q^2) = \frac{\sigma_T^{\frac{1}{2}} - \sigma_T^{\frac{3}{2}}}{\sigma_T^{\frac{1}{2}} + \sigma_T^{\frac{3}{2}}} = \frac{g_1 - \gamma^2 g_2}{F_1},
$$

$$
A_2(x_{Bj}, Q^2) = \frac{2\sigma_{TL}}{\sigma_T^{\frac{1}{2}} + \sigma_T^{\frac{3}{2}}} = \frac{\gamma(g_1 + g_2)}{F_1}. \tag{2.24}
$$

Here, the indices $\frac{1}{2}$ and $\frac{3}{2}$ display the sum of the photon spin antiparallel ($\frac{1}{2}$) and parallel ($\frac{3}{2}$) with respect to the virtual photon axis. σ_T denotes the photo-absorption cross section for transverse photons, while σ_{TL} is the interference between the transverse and longitudinal photon cross sections. The ratio R of the transversely and longitudinally polarized photo-absorption cross sections is given as

$$
R = \frac{\sigma_L}{\sigma_T} = (1 + \gamma^2)\frac{F_2(x_{Bj}, Q^2)}{2x_{Bj}F_1(x_{Bj}, Q^2)} - 1, \tag{2.25}
$$

with γ being the kinematic factor $2Mx_{Bj}/\sqrt{Q^2}$. The expressions for the photon-nucleon asymmetries A_1 and A_2 are included in the definitions of g_1 and g_2 such that

$$
g_1(x_{Bj}, Q^2) = \frac{F_2}{2x_{Bj}(1 + R)}(A_1 + \gamma A_2),
$$

$$
g_2(x_{Bj}, Q^2) = \frac{F_2}{2x_{Bj}(1 + R)}(\frac{A_2}{\gamma} - A_1). \tag{2.26}
$$

It is possible to extract $g_1(x_{Bj}, Q^2)$ from a measurement of the photon asymmetry A_1 in a DIS process, when neglecting the second asymmetry A_2 due to kinematic suppression and using the earlier measured structure function F_2 as well as the ratio R. The extracted asymmetry A_1 is related to the experimental asymmetry $A_{\parallel}$,

$$
A_1 \approx \frac{A_{\parallel}}{D} = \frac{1}{D}\frac{\sigma_{\overrightarrow{\Leftarrow}} - \sigma_{\overrightarrow{\Rightarrow}}}{\sigma_{\overrightarrow{\Leftarrow}} + \sigma_{\overrightarrow{\Rightarrow}}} \tag{2.27}
$$

where the arrows indicate the parallel and antiparallel spin orientations of the lepton beam with respect to the target nucleon, and $D = 2(1 - y)/(1 + (1 - y)^2)$ is the virtual photon depolarization factor. Like for the unpolarized structure functions, it is assumed that the polarized structure function $g_1(x_{Bj}, Q^2)$ is significantly dependent on Q^2 due to radiative QCD effects. In Fig. 2.3 it is shown that in various experiments the dependence of the polarized structure function $g_1(x_{Bj}, Q^2)$ on Q^2 is verified. The polarized quark distributions for the proton were extracted from global fits to inclusive DIS data from the experiments EMC, SMC and HERMES. For the neutron and the deuteron the dependence of $g_1(x_{Bj}, Q^2)$ on Q^2 could not be established yet due to statistical limitations. The published results for g_1^n can be
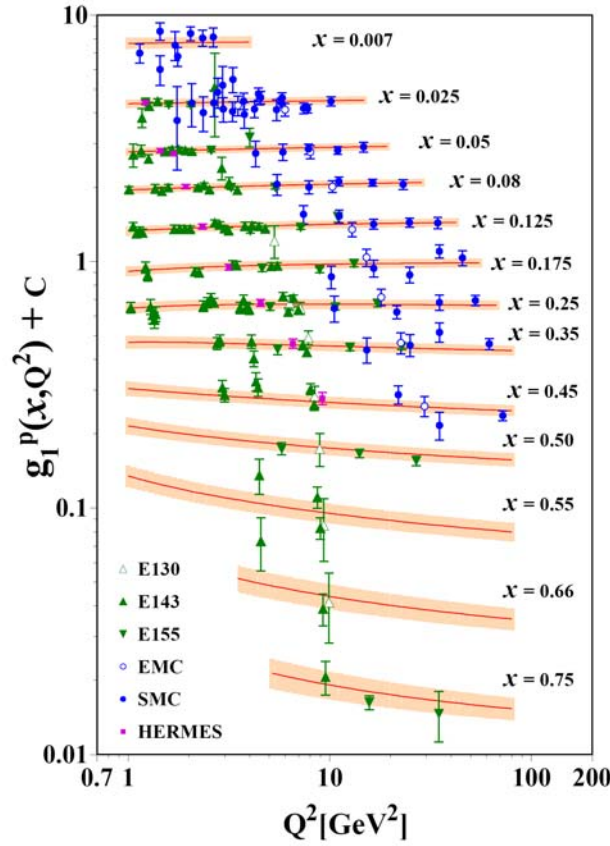
Figure 2.3:   The polarized structure function $g_1^p(x_{Bj}, Q^2)$ is measured in deep-inelastic lepton-nucleon scattering at the following experiments: E130 [26], E143 [27], E155 [28], EMC [5], SMC [29] and HERMES [30]. For clarity, a constant C is added to g_1^p. The data are plotted as a function of Q^2 for fixed values of x_{Bj}. The Asymmetry Analysis Collaboration [31] performed the global fits. The error bars contain the respective statistical and systematic errors.

found in Refs. [32, 33, 34, 35].

The QPM is an approximation in which the binding of the partons neglect the large-transverse-momentum reactions. Also it is not possible to calculate g_2 within the QPM [13], as shown in Eq. 2.20, because the quark mass is assumed to be negligible in the QPM. In the Operator Product Expansion it is possible to connect g_2 to quark-gluon interactions, assign an intrinsic Fermi motion inside the nucleon to the quark [13], and consecutively calculate g_2 which is extremely sensitive to transverse momenta and whether the quark mass is neglected or not [36]. The structure function g_2 has been measured for the proton [27, 37], neutron [38] and deuteron [37] within a kinematic range of $0.02 < x_{Bj} < 0.8$ and $1 < Q^2 < 30$ (GeV/c)^2. The integration of $x_{Bj} g_2$ is found to be consistent with zero for the proton, neutron and deuteron.

2.3 QCD-Improved Quark Parton Model

In the naive QPM some simplistic approximations have been applied. After the "spin crisis" when the spin 1/2 of the nucleon could not be verified in the QPM by measurements of the EMC experiment [13], a modification of the QPM was needed. Some nucleon constituents are missing in the naive QPM, which were found to be the gluons. The gluons do not interact directly with the virtual photon, nevertheless gluons are mediators for the strong interactions. Thus, a perturbative Quantum Chromodynamics (QCD) correction of the QPM needs to be applied which allows for interactions of quarks and gluons, e.g. quarks can radiate gluons, which can themselves either be re-absorbed by the quarks to produce quark-antiquark pairs or radiate further gluons. This QCD perturbative correction includes parton number densities to depend upon Q^2 in a way which is calculable in QCD. This changes the naive QPM only in a way that each of the densities $q(x_{Bj})$ are now a function of Q^2 as well, thus, being replaced by $q(x_{Bj}, Q^2)$. Therefore, the structure functions F_2 and g_1 are also dependent on Q^2. This is the dynamic breaking of the Bjorken scaling.

QCD is the non-Abelian gauge field theory of strong interactions, with gluons as mediators for the strong force through different colours. The gluons interact with each other with a scale-dependent coupling strength

$$\alpha_s(Q^2) = \frac{4\pi}{(11 - \frac{2}{3}n_f)\ln(Q^2/\Lambda_{QCD}^2)}, \qquad (2.28)$$

where $\Lambda_{QCD} \approx 0.3$ GeV is the QCD scale parameter of strong interactions. It indicates a lower limit for the domain of this perturbative correction. n_f is the number of quark flavours f which have a mass smaller than the momentum scale Q^2. The above equation is valid only for $Q^2 >> \Lambda_{QCD}^2$. The asymptotic freedom predicts that the strong force is weaker at short distances (corresponding to large values of Q^2), which means that the strong coupling constant is sufficiently small at short distances so that the QCD process can still be calculated with a perturbative expansion. At low energies the strong coupling constant increases significantly though, which makes the perturbative expansion not applicable anymore. The value of α_s depends on Q^2, and for $Q^2 \to \infty$ it vanishes logarithmically. Therefore, at small distances the quarks fit into the approximation of the naive QPM of being free point-like partons. An appropriate value to apply this regime is $Q^2 \approx 1$ (GeV/c)^2. For higher values of Q^2 the resolution power increases and surrounding sea quarks and gluons are resolved, which is demonstrated in Fig. 2.4. Each of the sea quarks carries a part of the proton momentum x_{Bj}, which corresponds to a decreasing number of partons at high x_{Bj} with increasing Q^2.

The evolution of the quark distribution functions with Q^2 is given by the Dokshitzer-Gribov-Lipatov-Altarelli-Parisi (DGLAP) equations [39, 40, 41]
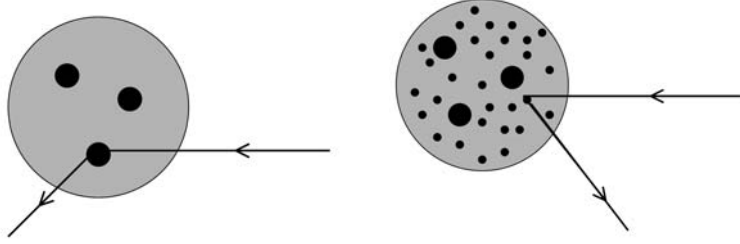
Figure 2.4: An incoming particle scatters off a parton inside a hadron. On the left, the scattering process takes place at low values of Q^2, where the incoming particle only sees valence quarks. On the right, the incoming particle also detects sea quarks due to its high resolution power which is correlated to Q^2.

$$\frac{d}{d\ln Q^2}\Delta q_{ns}(x_{Bj}, Q^2) = \frac{\alpha_s(Q^2)}{2\pi}\left[\Delta P_{qq}^{ns} \otimes \Delta q_{ns}\right](x_{Bj}, Q^2), \tag{2.29}$$

$$\frac{d}{d\ln Q^2}\begin{pmatrix} \Delta\Sigma(x_{Bj}, Q^2) \\ \Delta G(x_{Bj}, Q^2) \end{pmatrix} = \frac{\alpha_s(Q^2)}{2\pi}\left[\begin{pmatrix} \Delta P_{qq}^s & 2n_f\Delta P_{qg}^s \\ \Delta P_{gq}^s & \Delta P_{gg}^s \end{pmatrix} \otimes \begin{pmatrix} \Delta\Sigma \\ \Delta G \end{pmatrix}\right](x_{Bj}, Q^2),$$

in which the operator $\otimes$ defines a convolution integral as

$$[a \otimes b](x_{Bj}, Q^2) = \int_{x_{Bj}}^1 \frac{dy}{y}a\left(\frac{x_{Bj}}{y}, Q^2\right)b(y, Q^2). \tag{2.30}$$

The splitting functions P_{fi} represent the probability for finding a parton, either a quark or a gluon, carrying a momentum fraction x_{Bj} in the final state, while originating from an initial parton i with momentum fraction y. Here, a spin dependent case is considered and, thus, separate quark and gluon distribution functions with helicity-dependent splitting functions ΔP_{fi} are applied. Basically the DGLAP equations express the fact that a quark with the momentum fraction x_{Bj} could come from a parent quark with a larger momentum which has radiated a gluon, or from a parent gluon creating a $q\bar{q}$ pair. If the PDFs are known at a certain Q^2 scale, they can be computed at any other scale using the DGLAP equations. The flavour non-singlet distribution $\Delta q_{ns}(x_{Bj}, Q^2)$, the flavour singlet quark distribution $\Delta\Sigma(x_{Bj}, Q^2)$ and the gluon distribution $\Delta G(x_{Bj}, Q^2)$ are used as well. The flavour singlet distribution $\Delta\Sigma(x_{Bj}, Q^2)$ and non-singlet distribution $\Delta q_{ns}(x_{Bj}, Q^2)$ are defined as

$$\Delta\Sigma(x_{Bj}, Q^2) = \sum_i \Delta q_i = (\Delta u + \Delta\overline{u}) + (\Delta d + \Delta\overline{d}) + (\Delta s + \Delta\overline{s}), \tag{2.31}$$

$$\Delta q_{ns}(x_{Bj}, Q^2) = \sum_i \frac{e_f^2 - \langle e^2 \rangle}{\langle e^2 \rangle}\Delta q_i = (\Delta u + \Delta\overline{u}) - \frac{1}{2}(\Delta d + \Delta\overline{d}) - \frac{1}{2}(\Delta s + \Delta\overline{s}).$$

The expression $\langle e^2 \rangle = \sum_f e_f^2 / n_f$ contains the number of quarks n_f with their respective flavour f.

In the naive QPM the sum of the spin contributions of all quark and antiquark flavours, $\Delta\Sigma$, is assumed to be directly connected to the total nucleon spin as

$$S_N = \frac{1}{2} \sum_q \Delta q = \frac{\Delta\Sigma}{2}. \tag{2.32}$$

The structure function g_2 given in Eq. 2.20, which vanishes in the naive QPM, does not vanish in the QCD-improved QPM, instead its non-zero value arises from quark-gluon interactions. By taking the perturbative expansion of the QCD-improved QPM into account, Eq. 2.32 becomes

$$S_N = \frac{1}{2} = \frac{1}{2}\Delta\Sigma + \Delta G + \langle L_z \rangle, \tag{2.33}$$

where the possible contribution from the gluons is ΔG and from the quark and gluon orbital angular momenta is $\langle L_z \rangle$. Therefore, it is an important task at the COMPASS experiment to measure ΔG. This is also part of the scientific programme at HERMES (a polarized semi-inclusive DIS experiment) and at the high energy polarized pp scattering experiment at RHIC.

2.4 Transversity

In the previous chapter two PDFs, namely the unpolarized quark distribution function $q(x_{Bj})$ and the polarized quark or helicity distribution function $\Delta q(x_{Bj})$, were introduced. To fully describe the quark spin composition of the nucleon in leading order, an additional PDF is needed. This third distribution is the quark transverse polarization distribution $\Delta_T q(x_{Bj})$, which is called transversity distribution [10] and was first introduced in 1979 by Ralston and Soper [9]. In the 1990s the transversity distribution function moved into the focus of interest of theoretical research, when Jaffe and Ji [10], and Artru and Mekhfi [11] extensively investigated theoretical models. At the same time the first proposals were stated on how to measure the transversity distribution functions experimentally [42, 43].

The deep-inelastic scattering off nucleons can be described as elastic scattering off the quarks. According to the optical theorem, the hadronic tensor is related to the imaginary part of the forward virtual Compton scattering amplitudes $T_{\mu\nu}$ [44, 45]

$$W_{\mu\nu} = \frac{1}{2\pi} \Im (T_{\mu\nu}). \tag{2.34}$$

Therefore, the leading-order distribution functions, which are expressed in the tensor parametrization, can be given in terms of the imaginary part of the quark-nucleon forward amplitudes.
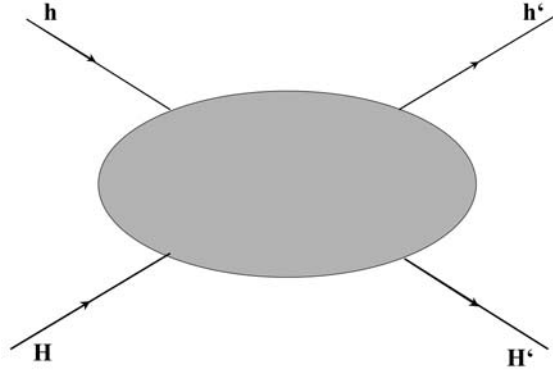
Figure 2.5: Sketch of the forward scattering amplitudes with helicities of quarks (h, h') and hadrons (H, H').

The forward scattering amplitude is shown in a "handbag" diagram in Fig. 2.5. Generally, the quark (h, h') and hadron (H, H') helicities take on the values $\pm 1/2$. Due to helicity conservation, the sum rule $H + h \rightarrow H' + h'$ applies. Under time reversal, the initial (H, h) and final (H', h') amplitudes are interchanged, parity operation transforms $h \rightarrow -h$ and so on. According to these restrictions [46], exactly three independent sets of helicity amplitude labels of the operation $(H, h) \rightarrow (H', h')$ exist,

$$
\begin{array}{cccc}
\dfrac{1}{2} & \dfrac{1}{2} & \rightarrow & \dfrac{1}{2} & \dfrac{1}{2} \\[2mm]
\dfrac{1}{2} & -\dfrac{1}{2} & \rightarrow & \dfrac{1}{2} & -\dfrac{1}{2} \\[2mm]
\dfrac{1}{2} & -\dfrac{1}{2} & \rightarrow & -\dfrac{1}{2} & \dfrac{1}{2}.
\end{array}
\tag{2.35}
$$

The first two amplitudes are diagonal in the helicity basis, since the quark does not flip its helicity. The third amplitude is off-diagonal, the quark flips its helicity. These three independent sets of helicity amplitudes can be grouped into the three quark distribution functions which measure the spin average $q(x_{Bj})$, the helicity difference $\Delta q(x_{Bj})$ and the transversity distribution $\Delta_T q(x_{Bj})$,

$$
\begin{aligned}
q &\leftrightarrow \left(\frac{1}{2} \quad \frac{1}{2} \rightarrow \frac{1}{2} \quad \frac{1}{2} \right) + \left(\frac{1}{2} \quad -\frac{1}{2} \rightarrow \frac{1}{2} \quad -\frac{1}{2} \right) \\
\Delta q &\leftrightarrow \left(\frac{1}{2} \quad \frac{1}{2} \rightarrow \frac{1}{2} \quad \frac{1}{2} \right) - \left(\frac{1}{2} \quad -\frac{1}{2} \rightarrow \frac{1}{2} \quad -\frac{1}{2} \right) \\
\Delta_T q &\leftrightarrow \left(\frac{1}{2} \quad -\frac{1}{2} \rightarrow -\frac{1}{2} \quad \frac{1}{2} \right).
\end{aligned}
\tag{2.36}
$$
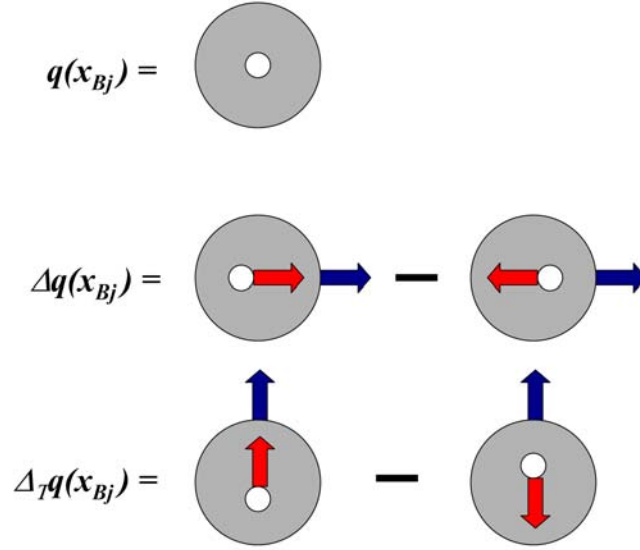
Figure 2.6: Probabilistic interpretation of leading order integrated parton distribution functions. Here, $q(x_{Bj})$ describes the unpolarized quark distribution. The helicity distribution $\Delta q(x_{Bj})$ describes longitudinally polarized quarks inside a longitudinally polarized nucleon. The transversity distribution $\Delta_T q(x_{Bj})$ describes transversely polarized quarks inside a nucleon polarized transversely with respect to its momentum.

A complete picture of the nucleon in leading order in terms of the PFDs is shown in Fig. 2.6. The sum and the difference of the probability to find a quark polarized along and against the polarization of a nucleon in a helicity eigenstate, respectively, results in the unpolarized quark distribution function $q(x_{Bj})$ and the helicity distribution function $\Delta q(x_{Bj})$. The transversity distribution function $\Delta_T q(x_{Bj})$ does not seem to have a probabilistic interpretation, although $\Delta_T q(x_{Bj})$ in the basis of transverse spin eigenstates can be interpreted as the probability to find a quark with its spin aligned along the transverse spin of the nucleon minus the probability to find it oppositely aligned.

An important boundary condition exists which restricts the distribution functions. From the definition of the unpolarized quark distribution function $q(x_{Bj}) = q^{\rightarrow}(x_{Bj}) + q^{\leftarrow}(x_{Bj})$ and the polarized quark distribution function $\Delta q(x_{Bj}) = q^{\rightarrow}(x_{Bj}) - q^{\leftarrow}(x_{Bj})$ it can be derived that

$$|\Delta q(x_{Bj})| \ \leq \ q(x_{Bj}). \tag{2.37}$$

Accordingly, it can be derived that the in the transversity base unpolarized distribution function $q(x_{Bj}) = q^{\uparrow}(x_{Bj}) + q^{\downarrow}(x_{Bj})$ and the in the transversity base polarized distribution function $\Delta_T q(x_{Bj}) = q^{\uparrow}(x_{Bj}) - q^{\downarrow}(x_{Bj})$ lead to the fact that

$$|\Delta_T q(x_{Bj})| \;\; \leq \;\; q(x_{Bj}). \tag{2.38}$$

Similar restrictions apply for the antiquark distributions. A combination of boundary conditions on $q(x_{Bj})$, $\Delta q(x_{Bj})$ and $\Delta_T q(x_{Bj})$ is united in the important Soffer inequality [47], which must be satisfied by the leading-order distribution functions,

$$q(x_{Bj}) + \Delta q(x_{Bj}) \geq 2\left|\Delta_T q(x_{Bj})\right|. \tag{2.39}$$

The transversity distribution function $\Delta_T q(x_{Bj})$ is a chiral-odd quantity that requires the helicity of the quark to be flipped. Since the quark helicity is conserved and the helicity flip is forbidden in all DIS processes, as shown at the top of Fig. 2.7, it is impossible to access $\Delta_T q(x_{Bj})$ in inclusive deep-inelastic scattering processes. An additional coupling partner is required to measure the transversity distribution. As shown at the bottom of Fig. 2.7, this coupling partner is provided by the transversely polarized fragmentation function $\Delta_T D_q^\Lambda(z)$ in semi-inclusive DIS (SIDIS), which will be introduced in Section 2.6.1. Due to the coupling of this chiral-odd partner, a helicity flip is allowed, and, thus, the measurement of transversity is possible in SIDIS.

In contrast to the longitudinally polarized distribution, a gluonic contribution towards transversity does not exist. A hypothetical $\Delta_T G(x_{Bj})$ would require a gluon-nucleon amplitude with helicity flip which does not exist due to helicity conservation. Gluons have helicity ± 1, but the nucleon cannot change its helicity by ± 2. This results in a different Q^2 evolution for transversity and helicity distributions. Therefore, even if they have the same value for a fixed value of Q^2, the function may look differently at another scale.

2.5   Λ Hyperon as a Spin Polarimeter

In a naive picture it is not expected to find polarization effects in a one-particle inclusive reaction like $a + b \rightarrow c + X$ where only particle c is detected in the final state. Depending on the available center-of-mass energy $\sqrt{s}$ there are many possibilities for X. In the considered inclusive reactions all available inelastic channels are summed over which should have random magnitudes and signs of polarizations. Thus, the average sum of polarization is expected to be zero. Contrary to this expectation, in 1975 it was discovered that Λ hyperons produced in pp collisions at low energies of 6 GeV/c are polarized [48]. Even at higher energies when unpolarized 300 GeV protons were scattered off a Be target at Fermilab in 1976, polarized Λ hyperons with a polarization of up to $P = 0.28 \pm 0.08$ were detected [8]. The polarization of inclusively produced Λ hyperons has since been observed in various
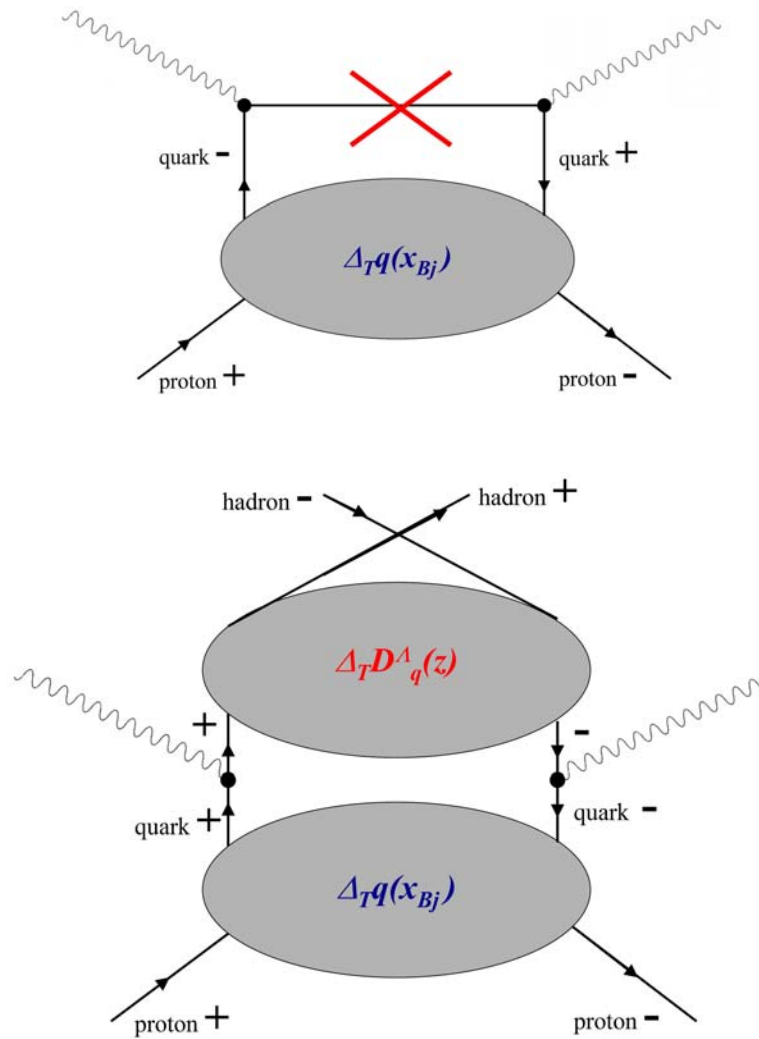
Figure 2.7: Top: "Handbag" diagram for the measurement of transversity, which is forbidden in DIS due to the helicity-flip of the quark. Bottom: "Handbag" diagram in SIDIS with an additional chiral-odd coupling partner $\Delta_T D_q^\Lambda(z)$ to allow for the required quark helicity-flip to measure transversity.

energies, ranging from a 12 GeV proton beam at KEK [49] to a $\sqrt{s} = 62$ GeV beam for proton-proton-collisions at CERN [50]. The observation of a non-zero polarization was completely unexpected. Theoretical expectation reasoned that spin effects should diminish and finally disappear at high energies due to the large number of possible channels contributing to the production cross section, which leads to the expected average polarization in inclusive high-energy processes to be zero. This expectation was contradicted. The observed polarization of Λ hyperons does not depend on the spin states of beam or target particle and is, therefore, sometimes

called spontaneous polarization [51]. The polarization of Λ hyperons has been observed in various environments and further reactions since. Yet it is not possible to describe this behaviour comprehensively. It is suspected that the Λ polarization originates from several sources which are either related to the structure of the nucleon itself or to the production process. Theoretical models include attempts to ascribe the polarization to either simply the constituent quarks or parametrizations based on perturbative QCD [52, 53]. An overview of the experimental and theoretical status is available in Refs. [54, 55, 56].

The Λ hyperon belongs to the $J^P = \frac{1}{2}^+$ baryon octet. Its mass is $m_\Lambda = 1115.683$ MeV/c^2 and its strangeness is $s = -1$. The two predominant decay channels are two body nonleptonic decays [24]

$$\begin{aligned}
\Lambda \to p + \pi^- \quad &: \qquad B.R. = 63.9 \pm 0.5\%, \\
\Lambda \to n + \pi^0 \quad &: \qquad B.R. = 35.8 \pm 0.5\%.
\end{aligned} \qquad (2.40)$$
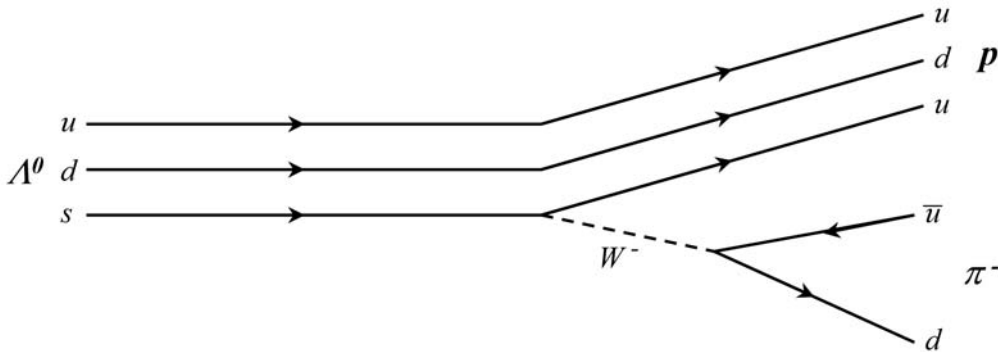
Figure 2.8: Decay of Λ into p and π^- via an intermediate W^- Boson in weak interaction.

Generally, the measurement of the polarization is very difficult since the spin distribution is not directly accessible. However, the Λ hyperon decays via a weak process, in which a s quark decays into an u quark and an additional π^-. This main decay channel $\Lambda^0 \to p\pi^-$ is shown in Fig. 2.8 and has a lifetime of $(2.632 \pm 0.020) \times 10^{-10}$ s, which equals a $c\tau$ of 7.89 cm. This short range of decay allows to identify the decaying Λ hyperon effectively. Both daughter particles of this decay are easily detected, therefore, this decay has been extensively studied in the past. The described process of Λ hyperon decay is parity-violating, which means that the daughter particles with respect to the direction of the parent Λ spin have a large asymmetry in the angular distribution. The angular distribution of the decay products reveal the polarization itself, which is called a self-analyzing decay. This feature of self-analyzing angular distribution makes the Λ decay particularly interesting for spin physics. In order to

take advantage of the self-analyzing property, the angular distribution has to be investigated in the Λ rest frame. This is shown in Fig. 2.9, where the z-axis is defined along the Λ spin direction. The quantum numbers of the p and π^- are $J^P = \frac{1}{2}^+$ and $J^P = 0^-$, respectively. The total angular momentum of the Λ is $J^P = \frac{1}{2}^+$ and must be conserved in the Λ decay. Therefore, the angular momentum l of the two decay products can either be $l = 0$ or $l = 1$. If parity was conserved in this decay, only p-waves with $l = 1$ were allowed due to $P = (-1)^l$. Since the weak decay violates parity, the s-waves with $l = 0$ contribute to the decay amplitude as well as the p-waves. The total wave function for the s- and p-waves expressed with the Clebsch-Gordan coefficients are
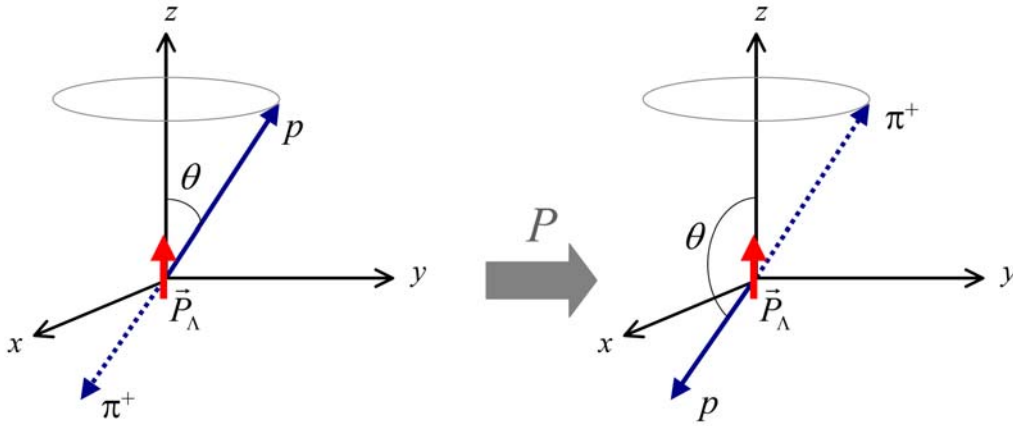
Figure 2.9: The Λ decay process in the Λ rest frame and the effect of the parity operation on the Λ decay [12]: Λ spin direction and momentum vectors of the decay products are given by red and blue arrows, respectively. Due to parity violation the proton prefers to go in the direction of the Λ spin.

$$\Psi_s = a_s Y_0^0 \chi^+,$$
$$\Psi_p = a_p \left(\sqrt{\frac{2}{3}} Y_1^1 \chi^- - \sqrt{\frac{1}{3}} Y_1^0 \chi^+ \right), \tag{2.41}$$

where $\chi^\pm (m_z = \pm\frac{1}{2})$ are Dirac spinors, Y_l^m are the corresponding spherical harmonics, and a_s and a_p are the complex amplitudes of the s- and p-waves, respectively [57]. The Dirac spinors have two possible spin states of the daughter particles with respect to the parent Λ spin direction: The parity-violating s-wave consist of proton and pion with no relative angular momentum $l = 0$ and parallel Λ and proton spin $m_\Lambda = m_p = +1/2$. The p-wave consists of two components, namely one with $m_l = +1$, where the spins of Λ and proton are antiparallel $m_\Lambda = -m_p = +1/2$,

and another one with $m_l = 0$, where the spins are parallel. The differential angular distribution of the decay particles is derived from the probability to be

$$\Psi\Psi^* \propto \frac{dN}{d\cos\theta d\phi} = \frac{N}{4\pi}\left(1 + \alpha\cos\theta\right), \tag{2.42}$$

with

$$\alpha = -\frac{2\Re(a_s a_p^*)}{|a_s|^2 + |a_p|^2} \tag{2.43}$$

being the asymmetry parameter which is a means to measure the parity violation of the Λ decay. The interference of the $s-$ and $p-$waves causes the decay baryon to be preferentially emitted either along or opposite to the Λ spin, depending on the sign of α. α has been measured in the decay $\pi^- p \rightarrow \Lambda K^0$ and its value is $\alpha = 0.642 \pm 0.013$ [24]. The angle θ is the angle between the direction of the Λ spin and the momentum vector of the outgoing proton in the Λ rest frame. The integration over the azimuthal angle results in a normalization constant of $N/2$.

If the direction of the initial Λ spin was not exactly pointing in direction of the z-axis, the differential angular distribution is expressed through the average Λ polarization with respect to the defined quantization axis P to be

$$\frac{dN}{d\cos\theta} = \frac{N}{2}\left(1 + \alpha P_\Lambda \cos\theta\right), \tag{2.44}$$

The angle θ can only be defined with respect to a well-defined reference axis, because the angular distribution might be additionally distorted if the initial spin state of the Λ hyperon P was not stated correctly. Therefore, the choice of a well-defined quantization axis is very important.

In principle, the product of α and P in the above formula can be accessed by a counting rate asymmetry. The number $N^\uparrow$ defines the number of Λ hyperons with their spin pointing along the quantization axis, while the number $N^\downarrow$ assigns the number of Λ hyperons with their spin pointing opposite to the direction of the quantization axis. By integrating the angular distribution the numbers $N^\uparrow$ and $N^\downarrow$ are found to be

$$\begin{aligned} N^\uparrow &= \int_0^1 \frac{N}{2}\left(1 + \alpha P\cos\theta\right) d\left(\cos\theta\right) = \frac{N}{2}\left(1 + \frac{\alpha P}{2}\right), \\ N^\downarrow &= \int_{-1}^0 \frac{N}{2}\left(1 + \alpha P\cos\theta\right) d\left(\cos\theta\right) = \frac{N}{2}\left(1 - \frac{\alpha P}{2}\right). \end{aligned} \tag{2.45}$$

Introducing an asymmetry between the spin-up and spin-down states of the Λ hyperons with respect to the quantization axis, the polarization can be simplified to [58]

$$\alpha P = \left[\frac{N^\uparrow - N^\downarrow}{N^\uparrow + N^\downarrow} \right]. \tag{2.46}$$

If the average number of particles with their spin pointing parallel or antiparallel to the quantization axis deviates from zero, the decay is polarized. By measuring the number of particles with their spin parallel and antiparallel to the quantization axis, it is possible to derive the product of αP from this measurement. Obviously, to be able to measure a non-zero polarization, both the asymmetry parameter α and the polarization P must not be zero. If the value of α is large, it is more likely to measure an asymmetry between the spin-up and spin-down states, hence it is easier to measure P. If on the other hand α is small, it gets more difficult to measure P and a larger data sample as well as small systematic errors must be accomplished to measure P. The asymmetry parameters which are measured for the two predominant decay channels are [24]

$$
\begin{aligned}
\Lambda \to p + \pi^- \quad &: \quad \alpha = 0.642 \pm 0.013, \\
\Lambda \to n + \pi^0 \quad &: \quad \alpha = 0.65 \pm 0.05.
\end{aligned}
\tag{2.47}
$$

It is a convention to use the angular distribution of the decay baryon (i.e. proton for Λ) to determine the polarization. Under observation of the CP invariance, the asymmetry parameter for the charge-conjugated decay $\overline{\Lambda}$ keeps the absolute value while receiving the opposite sign, thus, $\alpha_\Lambda = -\alpha_{\overline{\Lambda}}$. Since the value of α is known, it is in principle possible to find the Λ polarization P as described in Eq. 2.46 if an appropriate choice of the quantization axis is made. Along with the high branching ratio of 64 % into two charged particles, this makes the Λ decay experimentally easily accessible while its polarization can be detected in connection with the sufficiently high asymmetry parameter $\alpha = 0.64$.

2.6 Λ Production in Semi-Inclusive DIS

2.6.1 Fragmentation in SIDIS

In 1981, F. Baldracchini and others [59] proposed to consider Λ and $\overline{\Lambda}$ hyperons as spin polarimeters to investigate the quark spin in semi-inclusive DIS (SIDIS) reactions. In SIDIS reactions, the spin of the transversely polarized nucleon within the target material is transferred to the final-state Λ particle, which is created by the exchange of a virtual photon between the longitudinally polarized beam and a transversely polarized target. A theoretical overview of the spin transfer mechanism and transversely polarized parton densities, their evolution and measurement can be found in Ref. [60].

The Λ production in SIDIS is shown in Fig. 2.10. Here, a beam muon of negative helicity emits a polarized photon γ^*. Due to helicity conservation the photon is
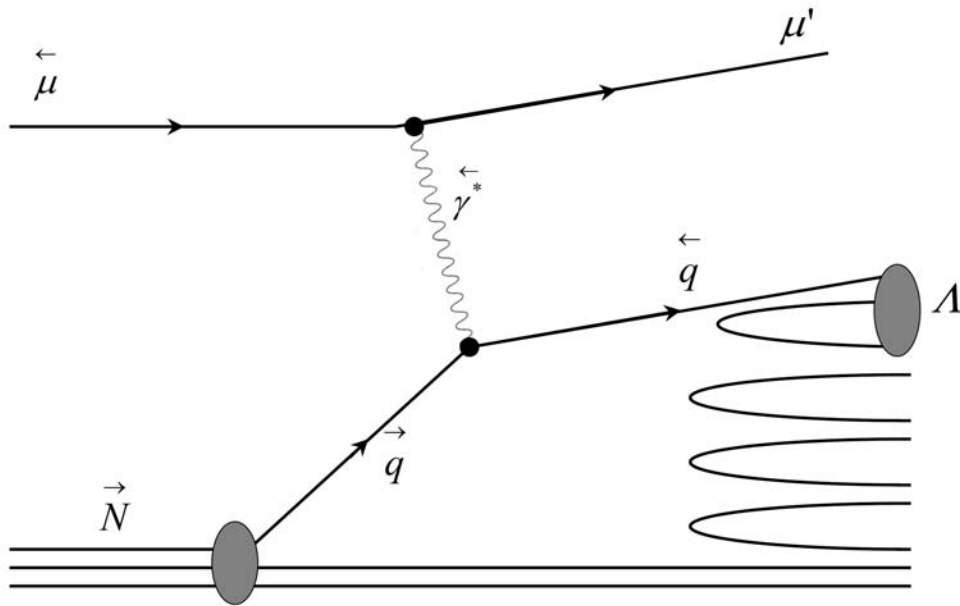
Figure 2.10: Λ production in a SIDIS process. The struck quark q hadronizes into a Λ which is described by the unpolarized $D_q^\Lambda(z, Q^2)$ and polarized $\Delta D_q^\Lambda(z, Q^2)$ fragmentation functions. The superscript arrows indicate the helicities of the particles.

allowed to only scatter off a quark q with opposite helicity. This confines the spin orientation of both the struck and the outgoing quark, which has the same spin orientation as the photon. The final hadron is produced by scattering the virtual photon off either a sea quark or a valence quark. The outgoing quark couples either with an antiquark to hadronize into a meson or with two more quarks to a colour-singlet final state baryon. This process of reassembling into an observable hadron from a struck quark or target remnant is called fragmentation or hadronization, where the produced hadron has a fractional energy $z = \frac{E_h}{\nu}$ of the virtual photon. The SIDIS process, where at least one hadron of the final state X in coincidence with the scattered muon μ' is detected, is investigated to find the contributions of quark spin orientations. The fragmentation process cannot be described in terms of perturbative QCD since the struck quark and the target remnant interact over a large range, which is attributed to an overly large value of the strong coupling constant α_s. Hence the fragmentation process cannot be described in terms of a perturbative expansion in terms of α_s but only as a non-perturbative QCD process.

An approach to calculate the fragmentation functions is to factorize the different components of the whole process, which is valid in the Bjorken limit. Since the fragmentation into the hadronic final state is independent from the absorption of the virtual photon by the quark, the process of hard scattering can be described by perturbative methods, while the fragmentation process is expressed in a scheme

similar to the one outlined in Section 2.3 where quark distribution functions inside the nucleon are described. The cross section for the factorization approach is a convolution of the three sub-processes,

$$\sigma = \text{Quark distribution} \otimes \text{Hard scattering} \otimes \text{Fragmentation}.$$

The differential cross section for the SIDIS process is expressed by

$$\frac{d\sigma}{dx_{Bj}dzdQ^2} = \frac{d\sigma_{incl}}{dx_{Bj}dQ^2} \frac{\sum_q e_q^2 q(x_{Bj}, Q^2) D_q^h(z, Q^2)}{\sum_q e_q^2 q(x_{Bj}, Q^2)}, \tag{2.48}$$

where σ_{incl} is the inclusive DIS cross section and the sum over q denotes all allowed quarks and antiquarks for both the quark distribution and fragmentation functions. The fragmentation functions $D_q^h(z, Q^2)$ express the probability for a quark to fragment into a hadron at a certain momentum scale Q^2 with the energy fraction z. The fragmentation functions are normalized to conserve energy and total average hadron multiplicity,

$$\sum_h \int_0^1 z D_q^h(z, Q^2) dz = 1,$$
$$\sum_h \int_{z_0}^1 D_q^h(z, Q^2) dz = \langle n_h(Q^2) \rangle, \tag{2.49}$$

with z_0 being the threshold energy for producing a hadron with mass m with a minimum multiplicity.

The fragmentation functions are conventionally split into polarized and unpolarized fragmentation functions for a final state hadron with non-zero spin. If a quark q with a given helicity fragments into a hadron with the same helicity ($\uparrow\uparrow$) or opposite helicity ($\downarrow\uparrow$), the unpolarized and polarized fragmentation to produce a single hadron is described by

$$D_q^h(z) = D_{q\uparrow\uparrow}^h + D_{q\uparrow\downarrow}^h,$$
$$\Delta D_q^h(z) = D_{q\uparrow\uparrow}^h - D_{q\uparrow\downarrow}^h. \tag{2.50}$$

For these relationships to hold true it is required that the absolute value of the polarized fragmentation functions is restricted by the value of the unpolarized fragmentation functions, therefore,

$$\left| \Delta D_q^h(z) \right| \leq D_q^h(z). \tag{2.51}$$

Generally for the Λ production, 6 quarks and 6 antiquarks theoretically contribute to a total of 12 possible quark fragmentation functions. In neglecting the heavy flavours and using SU(3) flavour symmetry, two independent fragmentation functions remain,

$$\begin{aligned}
\Delta D_u^\Lambda(z) &= \Delta D_d^\Lambda(z) = \Delta D_s^\Lambda(z), \\
\Delta D_{\bar{u}}^\Lambda(z) &= \Delta D_{\bar{d}}^\Lambda(z) = \Delta D_{\bar{s}}^\Lambda(z).
\end{aligned} \tag{2.52}$$

In SIDIS measurements it is observed that the fragmentation functions for the quarks are more probable and, thus, favoured, while the fragmentation functions for the antiquarks are disfavoured, $\Delta D_q > \Delta D_{\bar{q}}$. The reason for the quark fragmentation functions to be favoured is that the quark content of the Λ hyperon is each an up, down and strange quark. It is obviously easier for the already present quark types to fragment than it is to produce a new antiquark which subsequently fragments. Therefore, the disfavoured antiquark fragmentation functions do not contribute much and are usually suppressed.

2.6.2 Fragmentation in e^+e^- Annihilation

The method of factorization in QCD states that the quark distribution, hard scattering and fragmentation are three independent processes. This implies that the fragmentation can follow the hadronization scheme no matter which hadronization process applies. The hadronization process might be a DIS measurement as well as $q\bar{q}$ pair production in e^+e^- annihilation. Therefore, the e^+e^- annihilation can be considered as another source to creating a Λ hyperon. Contrary to the SIDIS process of hard scattering, the corresponding process $e^+e^- \to Z^0, \gamma^* \to q\bar{q}$ and its scattering cross section can be calculated in electroweak theory. Here, the coupling to fermions violates parity and favours certain helicity states. Therefore, the quarks which are produced at the Z^0 pole are naturally polarized, even if an unpolarized beam is used. The cross section for the semi-inclusive process $e^+e^- \to \Lambda + X$ can be expressed in terms of only its fragmentation part $\sigma \propto \sum_q D_q^\Lambda(z, Q^2)$, where the sum runs over the fragmentation functions of all quark and antiquark flavours. Due to the polarized nature of this process, the extraction of the polarized fragmentation functions $\Delta D_q^\Lambda(z, Q^2)$ for the e^+e^- annihilation is straightforward. More information on the QCD expression of fragmentation functions in e^+e^- annihilation can be found in Ref. [61].

2.6.3 Connection between Distribution and Fragmentation Functions

The two fundamental quantities to describe the structure of the nucleon are the quark distribution function $q(x_{Bj}, Q^2)$ and the quark fragmentation function $D_q^h(z, Q^2)$. Experimental measurements so far provide a good insight into $q(x_{Bj}, Q^2)$, while $D_q^h(z, Q^2)$ is not yet well known. It seems desirable to find a simple connection between these two functions to be able to predict $D_q^h(z, Q^2)$ with the knowledge of $q(x_{Bj}, Q^2)$ in a specified kinematic region.

This connection between the distribution function of quarks and the fragmentation process was stated in 1971 in the Gribov-Lipatov reciprocity relation, where the non-singlet splitting function for DIS and e^+e^- annihilation are equal in leading order [62]. Experimental measurements were not exactly able to prove this relation, since the theoretical prediction of the Gribov-Lipatov reciprocity relation stated a too low value of the structure functions F_1 and F_2 in e^+e^- inelastic annihilation [63]. A revised Gribov-Lipatov relation was found to be approximately correct for large values of z [64],

$$\frac{1}{z}D_q^h(z) = q(2 - \frac{1}{z}).$$ (2.53)

This relation can be further simplified by using $(2 - 1/z) \approx (1/[1 - (1 - 1/z)]) = z$ as $z \to 1$ to be

$$\frac{1}{z}D_q^h(z) = q(z).$$ (2.54)

Using this relation, it is possible to apply measured values of parton distributions in DIS experiments to predict fragmentation functions, which in turn are compared to experimental measurements on nucleon production in e^+e^- annihilation. When a distinction between valence and sea quarks is applied, the revised Gribov-Lipatov reciprocity relation provides a valid theoretical parametrization [64].

An immediate application of the new relation is the investigation of the Λ polarization near the Z resonance in e^+e^- annihilation and in polarized lepton DIS scattering. The fragmentation function of the Λ is assumed to be related to the spin structure of the Λ at $z \to 1$ at an input energy scale Q^2.

In the COMPASS experiment, a longitudinally polarized lepton beam and a transversely polarized nucleon target are used to measure the Λ polarization. There are two potential sources for the Λ polarization, either the polarized beam induced its polarization, or the polarized quarks of the target material pass on their polarization.

The Λ production in SIDIS can take place in two different kinematic regions, which are characterized by the Feynman scaling variable x_F,

$$x_F = \frac{2P_*^{||}}{W}.$$ (2.55)

Here, $2P_*^{||}$ is the longitudinal fraction of the hadron momentum in the γ^*N center-of-mass system. The first kinematic region is the current fragmentation region. It is characterized by a positive value of x_F, the selected particles move forward in the γ^*N rest frame. A Λ production mechanism in the current fragmentation function is shown in Fig. 2.11, where a u quark in the target nucleon absorbs a negatively polarized γ^*. The Λ is composed of the scattered u quark and each an additional d and s quark from the fragmentation process. If the Feynman scaling variable has a
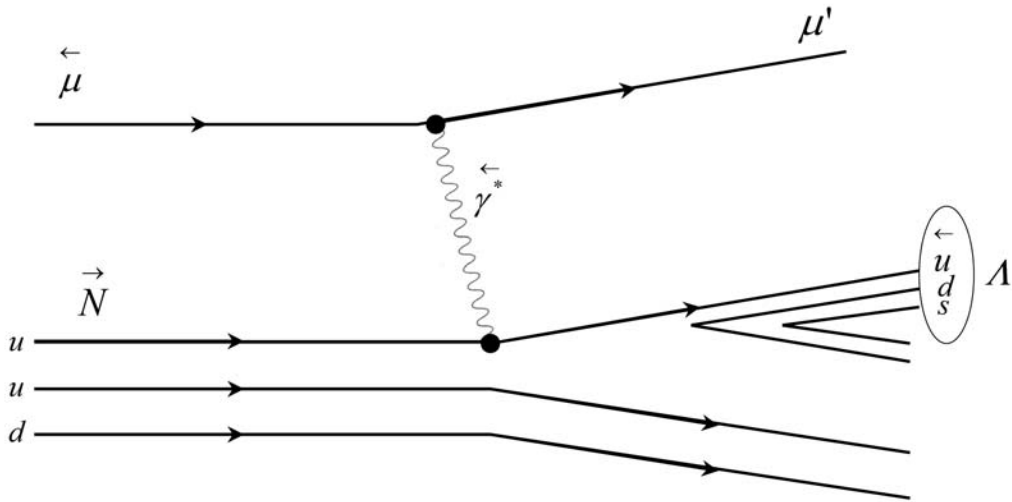
Figure 2.11: Λ production in the current fragmentation region.

high value of x_F, it is very likely that the hadron contains the struck quark.
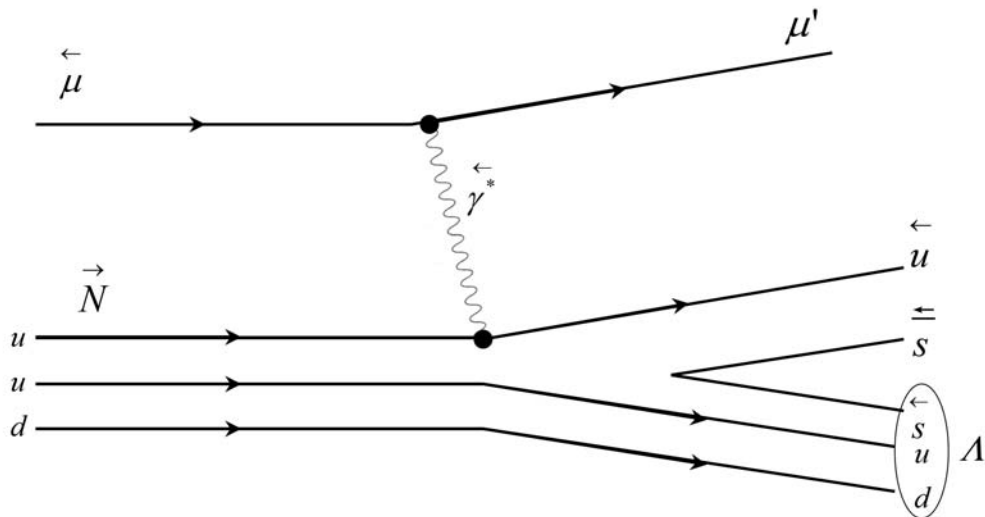
Figure 2.12: Λ production in the target fragmentation region.

The second kinematic region is the target fragmentation region and is characterized by a negative value of x_F. A dominant Λ production mechanism in SIDIS in the target fragmentation region is shown in Fig. 2.12. The hadron is located in the backward part of the $\gamma^* N$ rest frame. Here, the Λ hyperon does not contain the

struck quark. Instead the Λ consists of a remnant diquark and an additional s quark from the sea in the nucleon.

2.7 Extraction of Λ Polarization

2.7.1 Definition of Coordinate System

In this thesis, the production of polarized Λ hyperons in the reaction $\mu N \rightarrow \mu' \Lambda X$ is investigated. In Fig. 2.13 the production of a Λ hyperon in SIDIS is shown in the laboratory frame. The Λ is produced together with unidentified particles X by scattering a virtual photon γ^* which is emitted by the muon beam μ off the target nucleon N. The incoming muon μ and the outgoing muon μ' define the scattering plane, which is rotated by an angle ϕ around the direction of the virtual photon γ^* with respect to the production plane. The production plane is spanned by the virtual photon γ^* and the Λ for the laboratory frame; another way to define it is through the virtual photon γ^* and the target nucleon N for the Λ rest frame. The decay plane is formed by the two decay particles of the Λ hyperon, a positively charged proton and a negatively charged pion, and is rotated by an angle ϕ' around the production plane at the momentum direction of the Λ. The momentum direction of the Λ is defined as the $\vec{n}_\Lambda$ axis [12].
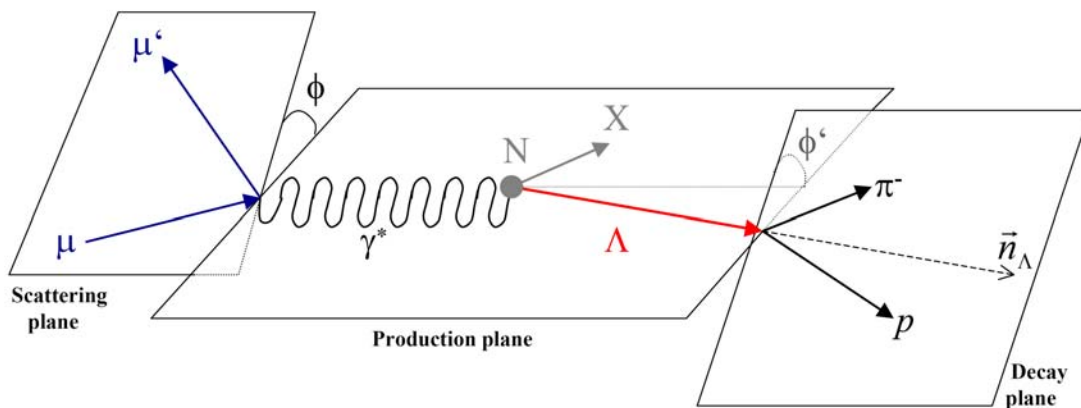
Figure 2.13: Definition of the coordinate system in the laboratory frame for the semi-inclusive production of a Λ hyperon.

In order to determine the Λ polarization, this process needs to be investigated in the Λ hyperon rest frame, where the angular distribution of the positive decay particle is analyzed [65]. For the calculation of the polarization in this analysis, the spin quantization axis of the measurement of transverse Λ polarization is defined by

using the target polarization and the μ - μ' scattering plane.
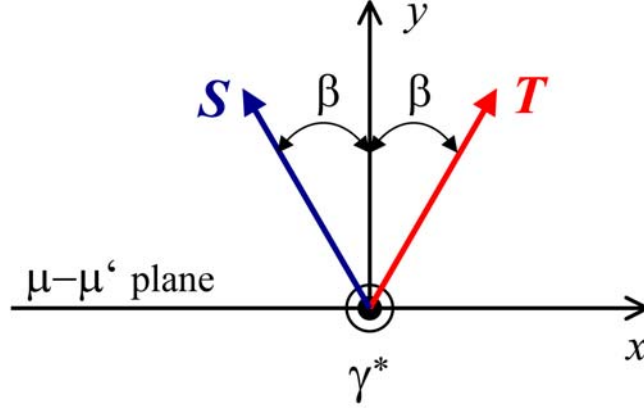
Figure 2.14: Definition of the reference frame: The initial (S) and final (T) transverse quark-spin-polarization vectors are shown with respect to the μ - μ' scattering plane. The virtual photon momentum γ^* is pointing out of the plane [66].

The direction of the target polarization is defined by the vector $\vec{S}$ [66, 67]. The target polarization can, thus, be expressed as $P_T = |\vec{S}|$. Therefore, the spin of the initial quark is oriented parallel to $\vec{S}$. In this case, the scattered quark is emerging with a spin direction defined by

- taking the component of the $\vec{S}$ vector perpendicular to the exchanged γ^*;

- reflecting this component with respect to the normal of the μ - μ' scattering plane, thus, obtaining the $\vec{T}$ vector (as shown in Fig. 2.14).

The directions of the axes are invariant under Lorentz transformation. Finally, the Λ polarization P_Λ with respect to a quantization vector T reveals itself in the angular distribution of the parity violating Λ decay as described in Eq. 2.44,

$$\frac{dN}{d\cos\theta_T} = \frac{N}{2}(1 + \alpha P_\Lambda \cos\theta_T), \tag{2.56}$$

where P_Λ is the average polarization with respect to the defined quantization axis T and α is the asymmetry parameter of the Λ hyperon. The angle θ_T cannot be defined without a reference axis because the angular distribution might be additionally distorted depending on the initial spin state of the Λ. Therefore, a well defined quantization axis needs to be selected. Here, θ_T is the proton emission angle with respect to the quantization axis $\vec{T}$, as shown in Fig. 2.15.
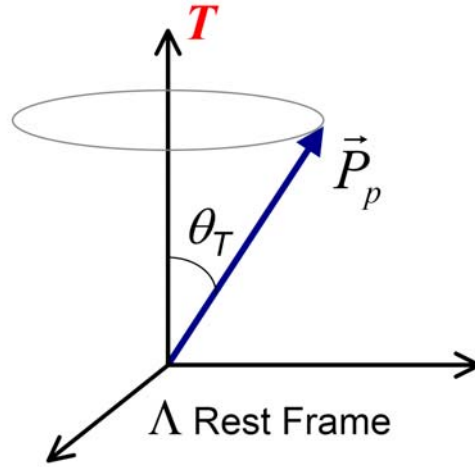
Figure 2.15: Definition of the angle of proton emission θ_T with respect to the quantization axis $\overrightarrow{T}$ in the Λ rest frame. $\vec{P}_p$ is the proton momentum [66].

A quark q which originates from a nucleon with polarization P_T has a probability to have its spin oriented along the $\overrightarrow{T}$ vector of

$$f P_T D(y) \Delta_T q(x_{Bj}). \tag{2.57}$$

If the struck quark fragments into a Λ hyperon, the corresponding polarization P_Λ is given by [68]

$$
\begin{aligned}
P_\Lambda(x_{Bj}, z) &= \frac{d\sigma^{lN^\uparrow \to l'\Lambda^\uparrow X} - d\sigma^{lN^\uparrow \to l'\Lambda^\downarrow X}}{d\sigma^{lN^\uparrow \to l'\Lambda^\uparrow X} + d\sigma^{lN^\uparrow \to l'\Lambda^\downarrow X}} \\
&= f P_T D(y) \frac{\sum_q e_q^2 \, \Delta_T q(x_{Bj}) \Delta_T D_q^\Lambda(z)}{\sum_q e_q^2 \, q(x_{Bj}) D_q^\Lambda(z)},
\end{aligned} \tag{2.58}
$$

where e_q is the charge of the quark and f is the dilution factor. The factor $D(y) = 2(1-y)/(1+(1-y)^2)$ is the spin-transfer coefficient or depolarization factor of the virtual photon with respect to the incident lepton. Here, y is the fraction of the incoming lepton energy carried by the exchanged virtual photon. $q(x_{Bj})$ and $\Delta_T q(x_{Bj})$ are the unpolarized and transversely polarized quark distribution functions of the nucleon, and $D_q^\Lambda(z)$ and $\Delta_T D_q^\Lambda(z)$ are the unpolarized and transversely polarized fragmentation functions, respectively (see Section 2.6.1). It appears that $\Delta_T q(x_{Bj})$ is coupled to $\Delta_T D_q^\Lambda(z)$, showing different factorizations of x_{Bj} and z [69].

Experimentally this means that when a lepton from the incoming beam interacts with one of the quarks of the transversely polarized nucleon, a scattered quark may

leave the nucleon in a polarization state which is determined by its transverse spin distribution function inside the nucleon. The struck quark from a SIDIS reaction hadronizes with a certain probability into a Λ hyperon and transfers a fraction of its polarization to the Λ. By assuming that part of the quark polarization is transferred to the final state hadron in the fragmentation process, which means that $\Delta_T D_q^\Lambda(z)$ must not be zero, then the measurement of the Λ polarization allows to gain insight about the transversity distributions. In [69] it is suggested that by measuring $P_\Lambda(x_{Bj}, z)$ in different bins of x_{Bj} and z, knowledge about $\Delta_T q(x_{Bj})$ by modeling $\Delta_T D_q^\Lambda(z)$ can be gained, or insight on both $\Delta_T q(x_{Bj})$ and $\Delta_T D_q^\Lambda(z)$ in different regions of x_{Bj} and z can be derived.

2.7.2   Method of Polarization Extraction

In general, the transverse polarization P_Λ cannot be directly extracted from the experimental data due to the distortion by the apparatus acceptance. The angular distribution of the decay proton with respect to the quantization axis $\overrightarrow{T}$, as given in Eq. 2.56, cannot be applied to the measurement in a practical way, because the measured angular distributions are convoluted with the detector acceptance. The COMPASS spectrometer has an asymmetric layout due to the dipole magnets. The method to correct for acceptance effects of the COMPASS spectrometer which will be presented here has the great advantage that no Monte Carlo simulation is needed. Monte Carlo simulations are time- and CPU-consuming and might not be able to fully describe the behaviour of an experimental setup in every detail. By applying symmetry arguments of the COMPASS spectrometer the method presented here allows to correct for acceptance distortions without needing to rely on Monte Carlo simulations.

First of all a description of the experimental acceptance as a function of the target spin orientation, the data taking period, the Λ azimuthal angle ϕ and the decay proton emission angle θ_T has to be introduced. With $Acc_{1(2)}^{\uparrow(\downarrow)}(\phi, \theta_T)$ the acceptance for Λ hyperons coming from the target cell with spin orientation $\uparrow$ ($\downarrow$), data taking period 1(2), emitted at an azimuthal angle ϕ and emitting a proton with an angle θ_T in the Λ rest frame is denoted. In an ideal spectrometer setting without any acceptance effects the following relations [66, 67, 70] hold

$$Acc_1^{\uparrow(\downarrow)}(\phi, \theta_T) = Acc_2^{\downarrow(\uparrow)}(\phi, \theta_T), \tag{2.59}$$

because in the second data taking period the polarization of each target cell is reversed. In reality the COMPASS spectrometer shows acceptance effects and, therefore, these relations have to be modified.

In the transversity case the azimuthal angle of the spin vector varies event by event. Therefore, the acceptance functions $Acc(\theta_T)$ are integrated over the ϕ angle. If one introduces the expressions for the number of Λ hyperons emitting a proton in the

angular bin $\cos\theta_T$, the number of particles reconstructed at a given azimuthal angle ϕ and emitting the proton at an angle θ_T with respect to the $\overrightarrow{T}$ vector is given by

$$N_{1(2)}^{\uparrow(\downarrow)}(\theta_T) = \Phi_{1(2)}^{\uparrow(\downarrow)}\left(\frac{d\sigma}{d\Omega}\right)^0 (1 + \alpha P_\Lambda \cos\theta_T)\, Acc_{1(2)}^{\uparrow(\downarrow)}(\theta_T). \tag{2.60}$$

The counting rates $N_{1/2}^{\uparrow/\downarrow}$ are explicitly given for the two target spin orientations ($\uparrow$ or $\downarrow$) and the two data taking periods (1 or 2), which form a pair taken under the same experimental conditions,

$$N_{1(2)}^{\uparrow}(\theta_T) = \Phi_{1(2)}^{\uparrow}\left(\frac{d\sigma}{d\Omega}\right)^0 (1 + \alpha P_\Lambda \cos\theta_T)\, Acc_{1(2)}^{\uparrow}(\theta_T)$$

$$N_{1(2)}^{\downarrow}(\theta_T) = \Phi_{1(2)}^{\downarrow}\left(\frac{d\sigma}{d\Omega}\right)^0 (1 - \alpha P_\Lambda \cos\theta_T)\, Acc_{1(2)}^{\downarrow}(\theta_T). \tag{2.61}$$

The spin of the decay proton is assumed to always point upwards in the laboratory frame. This assumption introduces a minus sign in the second expression of Eq. 2.61, due to the fact that the angle $\cos\theta_T$ is off by a phase of π, resulting in $\cos(\pi - \theta_T) = -\cos(\theta_T)$. Therefore, the following expressions $\mathcal{A}$, $\mathcal{B}$, $\mathcal{C}$ and $\mathcal{D}$ can be defined as

$$\mathcal{A} \equiv \sqrt{\frac{N_1^{\uparrow}(\theta_T)}{\Phi_1^{\uparrow}} \cdot \frac{N_2^{\uparrow}(\theta_T)}{\Phi_2^{\uparrow}}}$$

$$= \left(\frac{d\sigma}{d\Omega}\right)^0 (1 + \alpha P_\Lambda \cos\theta_T) \sqrt{Acc_1^{\uparrow}(\theta_T) \cdot Acc_2^{\uparrow}(\theta_T)}$$

$$\mathcal{B} \equiv \sqrt{\frac{N_1^{\downarrow}(\pi-\theta_T)}{\Phi_1^{\downarrow}} \cdot \frac{N_2^{\downarrow}(\pi-\theta_T)}{\Phi_2^{\downarrow}}}$$

$$= \left(\frac{d\sigma}{d\Omega}\right)^0 (1 + \alpha P_\Lambda \cos\theta_T) \sqrt{Acc_1^{\downarrow}(\pi - \theta_T) \cdot Acc_2^{\downarrow}(\pi - \theta_T)}$$

$$\mathcal{C} \equiv \sqrt{\frac{N_1^{\uparrow}(\pi-\theta_T)}{\Phi_1^{\uparrow}} \cdot \frac{N_2^{\uparrow}(\pi-\theta_T)}{\Phi_2^{\uparrow}}}$$

$$= \left(\frac{d\sigma}{d\Omega}\right)^0 (1 - \alpha P_\Lambda \cos\theta_T) \sqrt{Acc_1^{\uparrow}(\pi - \theta_T) \cdot Acc_2^{\uparrow}(\pi - \theta_T)}$$

$$\mathcal{D} \equiv \sqrt{\frac{N_1^{\downarrow}(\theta_T)}{\Phi_1^{\downarrow}} \cdot \frac{N_2^{\downarrow}(\theta_T)}{\Phi_2^{\downarrow}}}$$

$$= \left(\frac{d\sigma}{d\Omega}\right)^0 (1 - \alpha P_\Lambda \cos\theta_T) \sqrt{Acc_1^{\downarrow}(\theta_T) \cdot Acc_2^{\downarrow}(\theta_T)}. \tag{2.62}$$

Using these abbreviations $\mathcal{A}$, $\mathcal{B}$, $\mathcal{C}$ and $\mathcal{D}$ for the four square roots, the following counting rate asymmetry shall be introduced

$$\epsilon_T(\theta_T) = \frac{[\mathcal{A} + \mathcal{B}] - [\mathcal{C} + \mathcal{D}]}{[\mathcal{A} + \mathcal{B}] + [\mathcal{C} + \mathcal{D}]}. \tag{2.63}$$

The so-called reasonable assumption is given, e.g. in [70],

$$\frac{Acc_1^\uparrow(\theta_T)}{Acc_1^\downarrow(\theta_T)} = \frac{Acc_2^\downarrow(\theta_T)}{Acc_2^\uparrow(\theta_T)}. \tag{2.64}$$

The reasonable assumption states that the ratio of acceptances in the upstream and downstream target cells stays constant between data taking periods, which is a sensible assumption about the performance of the COMPASS spectrometer. Thus, the following equivalences of acceptance functions are valid,

$$
\begin{aligned}
Acc_1^\uparrow(\theta_T)Acc_2^\uparrow(\theta_T) &= Acc_1^\downarrow(\theta_T)Acc_2^\downarrow(\theta_T) \\
Acc_1^\uparrow(\pi - \theta_T)Acc_2^\uparrow(\pi - \theta_T) &= Acc_1^\downarrow(\pi - \theta_T)Acc_2^\downarrow(\pi - \theta_T),
\end{aligned} \tag{2.65}
$$

from which the relation can be derived

$$
\begin{aligned}
\sqrt{Acc_1^\uparrow(\theta_T)Acc_2^\uparrow(\theta_T)} + \sqrt{Acc_1^\downarrow(\pi - \theta_T)Acc_2^\downarrow(\pi - \theta_T)} = \\
\sqrt{Acc_1^\uparrow(\pi - \theta_T)Acc_2^\uparrow(\pi - \theta_T)} + \sqrt{Acc_1^\downarrow(\theta_T)Acc_2^\downarrow(\theta_T)}.
\end{aligned} \tag{2.66}
$$

The acceptance terms in square roots as shown in Eq. 2.62 are canceled out in the counting rate asymmetry in Eq. 2.63, leaving only the term proportional to the Λ polarization.

Since the target cells in the same period have the same muon flux ($\Phi_{1(2)}^\uparrow = \Phi_{1(2)}^\downarrow$), the muon flux can be simplified to

$$\Phi_1^\uparrow \cdot \Phi_2^\uparrow = \Phi_1^\downarrow \cdot \Phi_2^\downarrow = \Phi_1 \cdot \Phi_2. \tag{2.67}$$

It follows from Eq. 2.62, Eq. 2.66 and Eq. 2.67 that

$$
\begin{aligned}
\epsilon_T(\theta_T) &= \frac{[\mathcal{A} + \mathcal{B}] - [\mathcal{C} + \mathcal{D}]}{[\mathcal{A} + \mathcal{B}] + [\mathcal{C} + \mathcal{D}]} \\
&= \alpha P_\Lambda \cos \theta_T
\end{aligned} \tag{2.68}
$$

and the Λ polarization P_Λ can be extracted from the slope of the $\epsilon_T(\theta_T)$ distribution.

This formula is simplified if only two bins in the proton-decay-angle distributions are considered due to the limited statistics in this analysis. For this purpose the expressions for the number of protons emitted in the direction of the polarization axis ($U = \theta_T$) and opposite to it ($D = \pi - \theta_T$) are introduced. The expressions will be separately derived for the two target spin orientations ($\uparrow$ or $\downarrow$) and the two data taking periods (1 or 2), giving rise to eight independent subsamples.

$$
\begin{aligned}
\mathcal{A}^{\uparrow}_{1(2)} &\equiv N^{\uparrow}_{1(2)}(U) \\
&= \int_0^1 \frac{N^{1(2),\uparrow}_{tot}}{2} \left(1 + \alpha P_\Lambda \cos \theta_T\right) Acc^{\uparrow}_{1(2)}(\cos \theta_T) d\cos \theta_T \\
&= \frac{N^{1(2),\uparrow}_{tot}}{2} \left(1 + \frac{\alpha P_\Lambda}{2}\right) Acc^{\uparrow}_{1(2)}(U) \\
\mathcal{B}^{\downarrow}_{1(2)} &\equiv N^{\downarrow}_{1(2)}(D) \\
&= \int_{-1}^0 \frac{N^{1(2),\downarrow}_{tot}}{2} \left(1 - \alpha P_\Lambda \cos \theta_T\right) Acc^{\downarrow}_{1(2)}(\cos \theta_T) d\cos \theta_T \\
&= \frac{N^{1(2),\downarrow}_{tot}}{2} \left(1 + \frac{\alpha P_\Lambda}{2}\right) Acc^{\downarrow}_{1(2)}(D) \\
\mathcal{C}^{\uparrow}_{1(2)} &\equiv N^{\uparrow}_{1(2)}(D) \\
&= \int_{-1}^0 \frac{N^{1(2),\uparrow}_{tot}}{2} \left(1 + \alpha P_\Lambda \cos \theta_T\right) Acc^{\uparrow}_{1(2)}(\cos \theta_T) d\cos \theta_T \\
&= \frac{N^{1(2),\uparrow}_{tot}}{2} \left(1 - \frac{\alpha P_\Lambda}{2}\right) Acc^{\uparrow}_{1(2)}(D) \\
\mathcal{D}^{\downarrow}_{1(2)} &\equiv N^{\downarrow}_{1(2)}(U) \\
&= \int_0^1 \frac{N^{1(2),\downarrow}_{tot}}{2} \left(1 - \alpha P_\Lambda \cos \theta_T\right) Acc^{\downarrow}_{1(2)}(\cos \theta_T) d\cos \theta_T \\
&= \frac{N^{1(2),\downarrow}_{tot}}{2} \left(1 - \frac{\alpha P_\Lambda}{2}\right) Acc^{\downarrow}_{1(2)}(U).
\end{aligned}
\tag{2.69}
$$

The counting rate asymmetry is given in this simplified case by

$$
\begin{aligned}
\epsilon_T(\theta_T) &= \frac{\left[\sqrt{\mathcal{A}^{\uparrow}_1 \cdot \mathcal{A}^{\uparrow}_2} + \sqrt{\mathcal{B}^{\downarrow}_1 \cdot \mathcal{B}^{\downarrow}_2}\right] - \left[\sqrt{\mathcal{C}^{\uparrow}_1 \cdot \mathcal{C}^{\uparrow}_2} + \sqrt{\mathcal{D}^{\downarrow}_1 \cdot \mathcal{D}^{\downarrow}_2}\right]}{\left[\sqrt{\mathcal{A}^{\uparrow}_1 \cdot \mathcal{A}^{\uparrow}_2} + \sqrt{\mathcal{B}^{\downarrow}_1 \cdot \mathcal{B}^{\downarrow}_2}\right] + \left[\sqrt{\mathcal{C}^{\uparrow}_1 \cdot \mathcal{C}^{\uparrow}_2} + \sqrt{\mathcal{D}^{\downarrow}_1 \cdot \mathcal{D}^{\downarrow}_2}\right]} \\
&= \frac{\alpha P_\Lambda}{2}.
\end{aligned}
\tag{2.70}
$$

To demonstrate the way in which the counting rates $N^{\uparrow/\downarrow}_{1/2}$ are obtained in this analysis, and their application to compute the polarization of the Λ hyperons, an example shall be given here.

The mass distributions of the eight disjoint subsamples of the full 2007 data set are plotted as shown in Fig. 2.16. The signal peaks are fitted with a Gaussian, the background distributions are best described by a 3rd degree polynomial. The counting rates $N^{\uparrow}_1(U)$, $N^{\uparrow}_2(U)$, $N^{\downarrow}_1(D)$, $N^{\downarrow}_2(D)$, $N^{\uparrow}_1(D)$, $N^{\uparrow}_2(D)$, $N^{\downarrow}_1(U)$ and $N^{\downarrow}_2(U)$

correspond to the signal event numbers in the respective mass peaks and allow to derive the counting rate asymmetry $\epsilon_T(\theta_T)$. Thus, it can be seen that by assuming simple symmetry arguments of the COMPASS spectrometer it is not necessary to apply extensive Monte Carlo simulations to correct for apparatus acceptance effects. The polarization of the Λ hyperons $P_\Lambda = 2\epsilon_T(\theta_T)/\alpha$ can be extracted straightforward by applying these symmetry arguments and fitting the signal peaks of the eight disjoint subsamples of the 2007 data set [66].
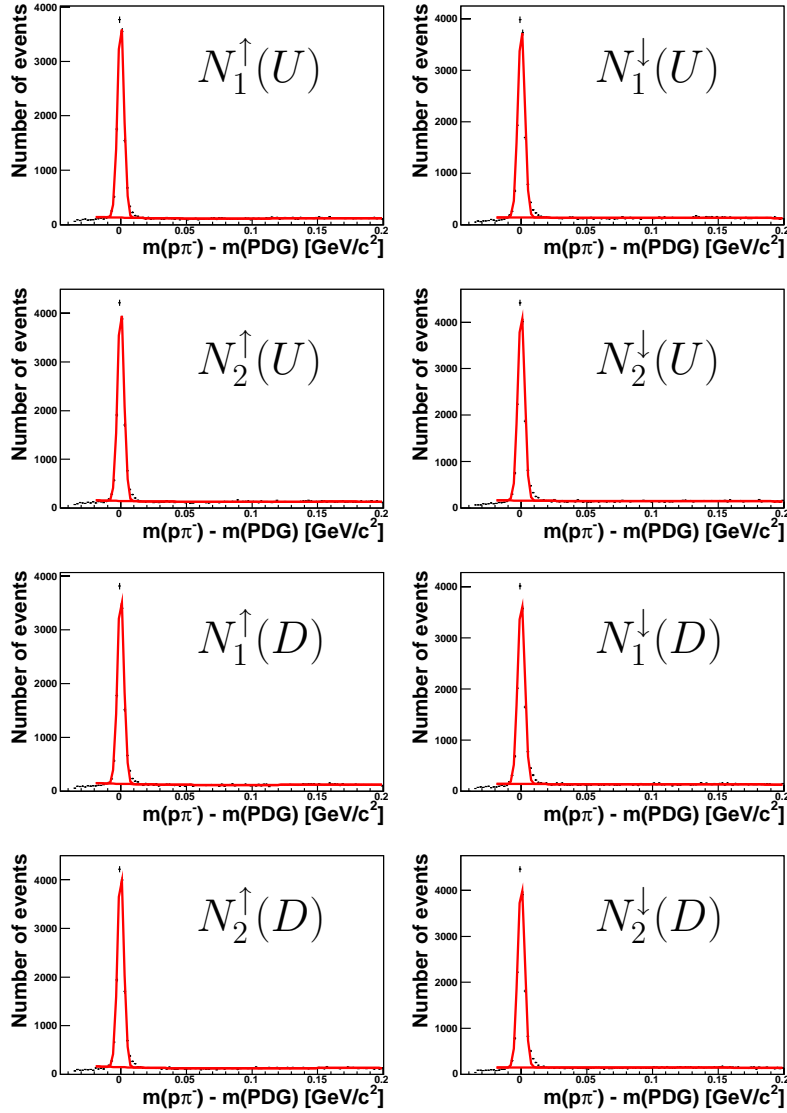
Figure 2.16: Mass fits of the eight disjoint subsamples $N^{\uparrow/\downarrow}_{1/2}(U/D)$ of the full 2007 data set, where each signal peak is described with a Gaussian fit and each background distribution is described with a 3rd degree polynomial. In the fit procedure the invariant Λ mass is shifted by $m(p\pi^-) - m_{PDG}$, where $m_{PDG} = 1.115683$ GeV/c² is the value of the Λ mass as published by the Particle Data Group [24].

Chapter 3

COMPASS Spectrometer

3.1 General Overview

The "COmmon Muon and Proton Apparatus for Structure and Spectroscopy", in short COMPASS [71], is a fixed target spectrometer which is located at the end of the M2 beam line of the SPS (Super Proton Synchrotron) at CERN. COMPASS' diverse physics program features measurements with a polarized muon beam as well as hadron (pion π, proton p, and Kaon K) beams which collide on nuclear targets. The muon program of COMPASS performs studies of the nucleon spin structure by scattering polarized muons off of polarized nucleons. The goal is to find the composition of the nucleon spin. The COMPASS hadron program includes the investigation of the hadron structure and the spectroscopy of charmed baryons.

The physics program of COMPASS was approved in 1997. In 2001 the commissioning of the spectrometer was conducted, and from 2002 to 2007 physics data were recorded with a muon beam. A pilot run with a pion beam was taken in 2004, and in 2008 the hadron program was able to collect physics data. Today the collaboration focuses the efforts of almost 240 physicists from 28 institutes in 11 countries.

In this chapter the COMPASS spectrometer and its main components are described. An overview of the COMPASS apparatus in the muon beam setup is shown in Fig. 3.1. A complete description can be found in [72] and in the citations therein.

In order to be able to detect potentially interesting physics events, the spectrometer must fulfill a range of specific requirements, such as covering a large range of scattering angles and, thus, a large Q^2 region. At the same time the apparatus must work efficiently in a high luminosity environment which also necessitates a good time resolution to select and record physics events. This demands an efficient trigger and a data acquisition system which can record high flux data. Track reconstruction and particle identification play a crucial role in identifying physics events. To fulfill these requirements, the COMPASS spectrometer is designed in two stages, the Large Angle Spectrometer (LAS) and the Small Angle Spectrometer (SAS). Both
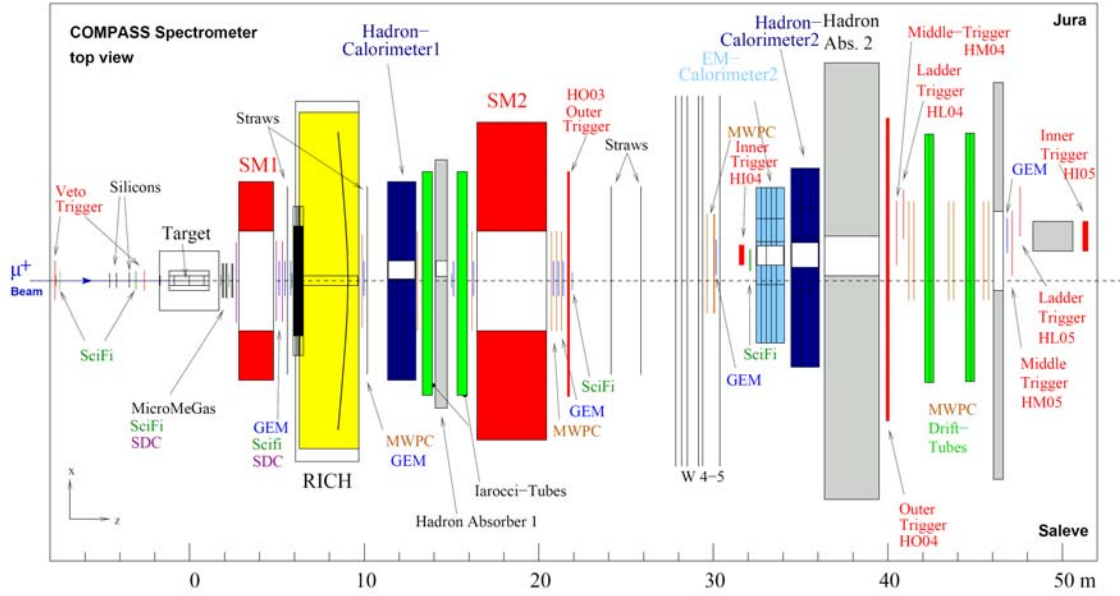
Figure 3.1: Top view of the COMPASS muon setup [72].

stages are located downstream of the target, the LAS starts with the SM1 magnet
downstream of the target. The deflection of particles in a magnetic field depends
on the charge of the particle, and the deflection radius is proportional to the ratio
of magnetic field strength and particle momentum. When particles are scattered at
large angles from the target, the large polar acceptance of the LAS of ±180 mrad
allows the detection and identification of these particles. The LAS is built around
the analyzing dipole magnet SM1 with a bending power of 1.0 Tm, which is used to
deflect and separate tracks of the lower-momentum particles at large angles. A va-
riety of detectors is built in the first stage of the spectrometer to measure the tracks
which are bent in the magnetic field, thus, allowing the determination of the mo-
menta of the scattered particles. The LAS also features a RICH detector to measure
the velocity of charged particles. The combination of information on both momenta
and velocities allows the derivation of the mass of the particles. Apart from small
effects of multiple scattering in the gas radiator, the RICH detector does not inter-
fere with the particle trajectories. Particles that are travelling further downstream
reach the last components of the LAS, the hadronic calorimeter and the muon wall.
The hadronic calorimeter measures the energy of passing hadrons and contributes
to hadron identification. The muon filter features a large amount of material to
absorb all passing particles except muons with their high penetration length. The
most downstream component of the LAS is the muon wall where those muons are
finally detected. Starting in 2006, a new electromagnetic calorimeter, ECAL1, was
implemented in the LAS to detect electrons and photons.

Further downstream and ≈ 15 m from the target is the second stage, the SAS, which

features an acceptance of $\pm$30 mrad and a length of 30 m. Particles which are scattered off the target at small polar angles and high momentum can be detected and identified in the second stage of the spectrometer. The setup of the SAS is similar to the components of the LAS, except that the second stage of the spectrometer does not feature a RICH detector. The components of the SAS are built around the SM2 analyzing dipole magnet with a higher bending power of 4.4 Tm to deflect particles in the higher-momentum range. The SAS includes an electromagnetic calorimeter, ECAL2, which is used to detect electrons and photons.

The experimental setup as shown in Fig. 3.1 also displays the COMPASS reference system. The z-axis is defined to be along the muon beam line entering from the left side, while the x-axis follows the horizontal direction and the y-axis the vertical direction. The origin of all axes is defined to be in the target. Positive values of x are often referred to be on the "Jura side", while negative values of x are correspondingly called to be on the "Saleve side" - this connotation follows the location of those mountains around the experiment with respect to the spectrometer.

3.2   Polarized Muon Beam

The polarized muon beam which is used for COMPASS is produced by colliding a high-energy proton beam on a production target. The mechanisms and accelerators involved are briefly described in this chapter and are shown in Fig. 3.2.

In the Proton Synchrotron (PS) a primary proton beam is first accelerated to a nominal momentum of 14 GeV/c and then injected into the Super Proton Synchrotron (SPS). The SPS accelerates the primary proton beam further to a nominal momentum of 400 GeV/c, at which it is successively extracted with an intensity of 1.2×10^{13} protons within a spill time of 4.8 s during a SPS cycle (which includes injection, acceleration and extraction and in total lasts 16.8 s). The extracted protons collide on the production target T6, which is 500 mm thick and made of Beryllium. A schematic view of the vertical plane of the M2 muon beamline is shown in Fig. 3.3. This produces a secondary beam of mainly pions with a small contamination of kaons and protons. At the production target the pion flux has a kaon contamination of about 3.6 %. The pion beam momentum is selected to a nominal value of 172 GeV/c with a $\pm$10 % momentum spread by deflecting the pion beam with bending magnets B1-B3 and scrapers (collimators made of magnetized iron that deflect low momentum particles away from the beam) in the M2 beam line, which is about 1 km long. The pion beam is then traversing a 600 m long decay tunnel, in which roughly 5 % of the pions decay into a muon and a neutrino. Since this decay is parity-violating, the muons are naturally polarized completely in the pion center-of-mass system. In the laboratory system the fraction of muons which are polarized depends on the beam phase space of the experimental setup.
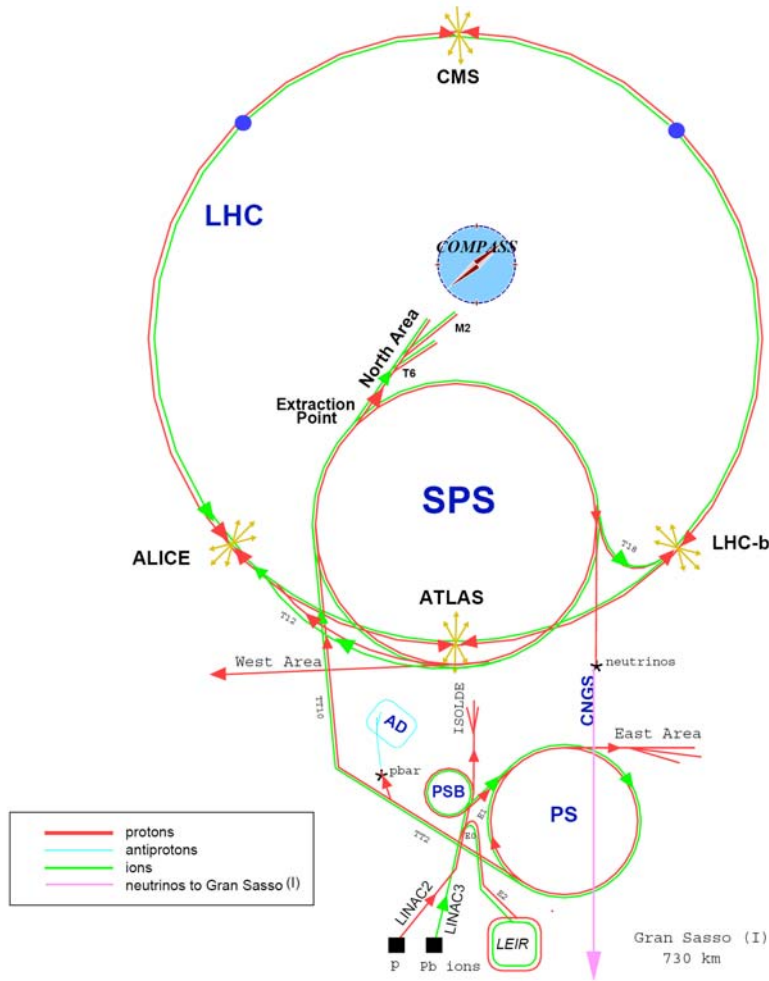
Figure 3.2: The accelerator complex at CERN, in which the locations of the PS and SPS accelerators and the COMPASS experiment are indicated.
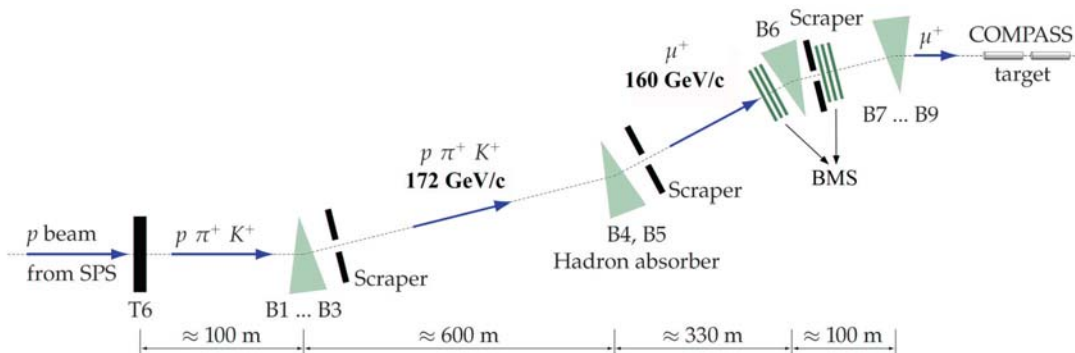
Figure 3.3: Schematic view of the vertical plane of the M2 muon beamline.
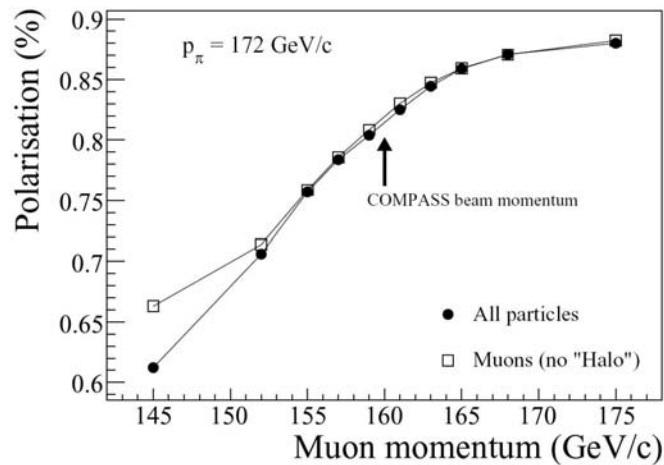
Figure 3.4: The muon beam polarization as a function of muon momentum, assuming a hadron momentum of 172 GeV/c [73].

The level of muon polarization which is achieved depends, therefore, on the fraction of the parent pion momentum carried by the decay muon [73]. This dependence is illustrated in Fig. 3.4 where the muon polarization is shown as a function of the muon momentum, assuming a fixed pion momentum of 172 GeV/c. The final muon polarization value is optimized to a value of (-80 ± 4) % in the 2004 run, where also a small correction due to the kaon component of the pion stream is included. At the final muon beam polarization the beam intensity reaches its maximum with a beam flux of 2×10^8 muons per SPS spill. At the end of the decay tunnel, hadronic absorbers remove the hadron contamination of the beam. Those hadron absorbers are made of Beryllium and each of the nine Beryllium blocks is 1.1 m long. Only the muons in the beam pass the double bend upward. The muons lose approximately 2-3 GeV/c of their momentum on their way through the hadron absorbers. After filtering the muon beam according to the desired muon momentum of 160 GeV/c with two bending magnets B4 and B5 and scrapers, the muon beam is deflected by magnets from the underground SPS level to the surface level of the experimental hall. To make maximum use of the incident flux, the momentum spread of the beam as defined by the beam optics can reach up to 5 %. It is important to accurately assess the kinematic parameters of the beam, therefore, an accurate measurement of the momentum of each individual muon is required. This is done by the Beam Momentum Station (BMS). Before entering the experimental hall, the momentum of the muon beam is exactly measured by the BMS. The BMS consists of a bending magnet B6 surrounded by six hodoscopes. Three BMS hodoscopes are located in front of bending magnet B6 and the other three BMS hodoscopes are situated behind B6. When the charged particles in the beam have different incoming momenta, their change of angular direction in the vertical magnetic bending plane allows the measurement of the momentum of each beam particle. The time resolution of the

BMS is 0.3 ns, while the reconstruction efficiency of each beam track is $\approx$ 93 % and the momentum resolution is better than 1 %. At the end of the beam line a set of multiple quadrupole magnets, B7-B9, focuses the beam onto the COMPASS target. The described setup allows for an incoming muon flux of approximately 2×10^8 muons per SPS cycle. Around the beam is a halo, which consists of muons which are not properly absorbed or deflected. Within a range of 15 cm from the beam line, the "near" halo accounts for $\approx$ 16 % of the beam intensity. Outside of this region, the "far" halo still accounts for $\approx$ 7 % of the beam intensity.

3.3   Polarized Target

The main task of COMPASS is to find the origin of the nucleon spin. The measurement of such spin effects is conducted by using a polarized solid state target and finding asymmetries between periods of data taking with opposite polarizations of the target cells.

From 2002 to 2006, ^{6}LiD was chosen as a deuteron target because of its high polarizability [74]. In a first approximation ^{6}LiD can be pictured as being formed by a spin-0 ^{4}He nucleus and two spin-1 deuterons. Two ^{6}LiD target cells are independently polarized in opposite directions. After a period of taking data the direction of polarization in both target cells is reversed. Each of the two target cells has a diameter of 3 cm and a length of 60 cm. A 0.1 mm copper foil is located in the middle of a 100 mm gap between the two target cells. This copper foil works as a microwave stopper to isolate the two different microwave frequencies which are present in the two target cells as will be explained now.

The target is polarized longitudinally with respect to the direction of the muon beam by a dynamic nucleon polarization (DNP) technique [75]. The target material is placed inside a microwave cavity in which a microwave frequency modulation is applied at a temperature of 200 to 300 mK. The irradiation of the target material with microwaves slightly below or above the electron spin resonance (Larmor) frequency transfers the high electron polarization to the nucleons by resonant absorption of the microwaves. This transition is conducted efficiently in a magnetic field of 2.5 T with 10^{-4} homogeneity of a solenoid magnet.

The change of the target spin configuration is performed by a combination of two different techniques. The first technique is a microwave reversal, which is explained as DNP above. The microwave reversal is applied for changes of the target spin polarization in the longitudinal direction. By applying different microwave frequencies, different polarization directions of the target cells can be achieved. Since the target spin needs about one week to reach the maximum polarization, this technique is not applicable for frequent changes of the target spin configuration. The second technique to change the target spin orientation is a field rotation, which is done by

changing the solenoid current while maintaining a transversal dipole field. Since the nuclear spin follows the direction of the external magnetic field, it is possible to change the direction of the target spin more quickly than by microwave reversal. The field rotation is applied every 8 hours to reduce possible systematic effects on the spectrometer acceptance and the different amount of target material in the two target cells. The average target polarization has been measured with a nuclear magnetic resonance (NMR) probe [76] to be 54 % in the upstream cell and 47 % in the downstream cell.

The COMPASS muon program includes the measurement of the transverse spin-dependent structure function with a transversely polarized target. The transverse spin polarization of the target can be realized by stopping the field rotation of the solenoid at a maximum dipole and zero solenoid field. This is the so-called transverse mode (nucleon spin orthogonal to the beam direction, see Fig. 3.5 for 2007 target setup). During data taking in transverse mode, the polarization of the target material is maintained by a transverse 0.42 T dipole field and the target material is kept in "frozen spin" at a temperature below 90 mK to avoid thermal relaxation. Due to the very long relaxation time of the target material at such a low temperature being in the order of 1000 hours, the polarization of the target material stays at an approximately constant level during the data taking.
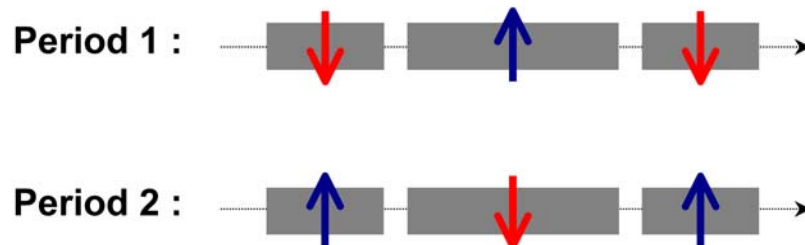
Figure 3.5: Schematic of direction of target cell polarizations in transverse mode during two consecutive data taking periods in 2007. The projected beam traverses the target cells from the left to the right side of the sketch. Red arrows indicate a target spin orientation in downwards direction, blue arrows show an upward target spin orientation.

Until 2006, a solenoid from the precessor experiment SMC was used since the solenoid designed for COMPASS was not available yet. The SMC solenoid has a limited acceptance of ± 70 mrad compared to the new COMPASS superconducting solenoid magnet; the limited acceptance for data taken before 2006 is indicated in Fig. 3.6. In 2006 the new superconducting COMPASS solenoid magnet was implemented and, therefore, the full COMPASS acceptance of ± 180 mrad can now be successfully studied.
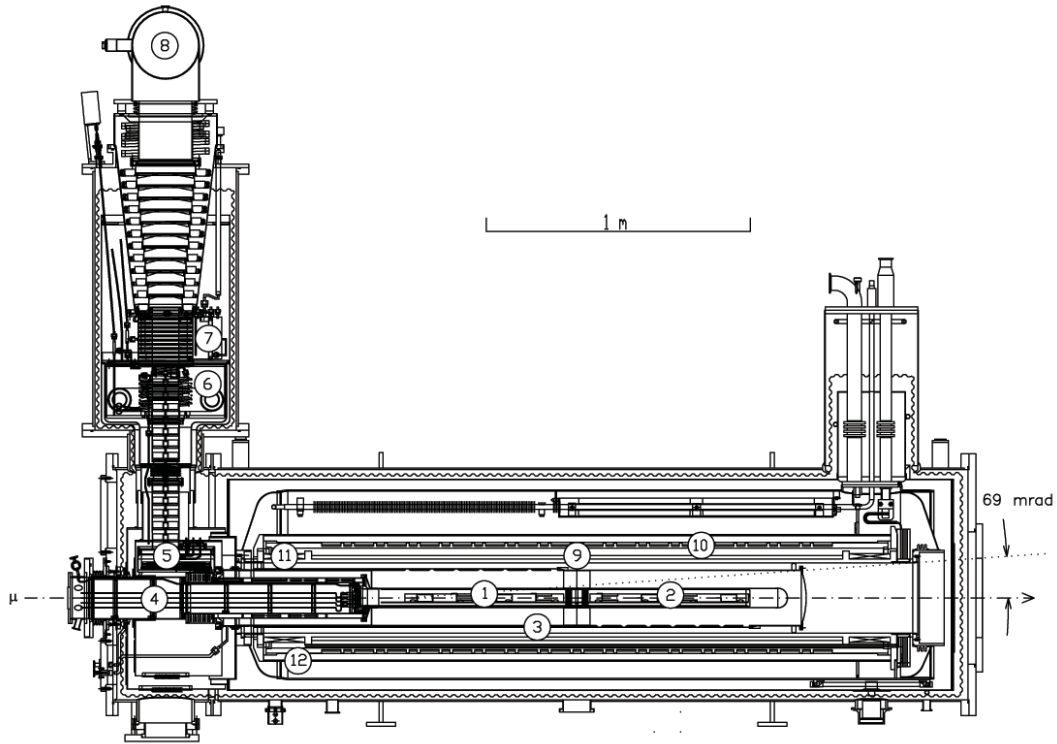
Figure 3.6: Side view of the COMPASS polarized target [72]: (1) upstream and (2) downstream target cell, (3) microwave cavity, (4) target holder, (5) still (^{3}He evaporator), (6) ^{4}He evaporator, (7) ^{4}He liquid/gas phase separator, (8) ^{3}He pumping port, (9) solenoid coil, (10-11) compensation coil, (12) dipole coil. The muon beam enters from the left. The two halves of the microwave cavity are separated by a thin microwave stopper.

Starting in 2007 COMPASS utilizes a polarized NH_3 (ammonia) target, which consists of three target cells with 4 cm diameter. The upstream and downstream cells are each 30 cm long, the middle cell has a length of 60 cm. The target cells of this "proton target" are polarized in opposite directions during two consecutive periods of data taking as shown in Fig. 3.5. The principle of polarizing the target material is identical to the procedure described above. The polarization values of the proton target reach > 80 %.

The structure of the target cells is visible in Fig. 3.7, which shows the distribution of the reconstructed vertices along the beam axis for data taking with the deuteron target (2002-2004) and with the proton target (2007). The analysis presented in this thesis comprises data taken in transverse mode in 2007.
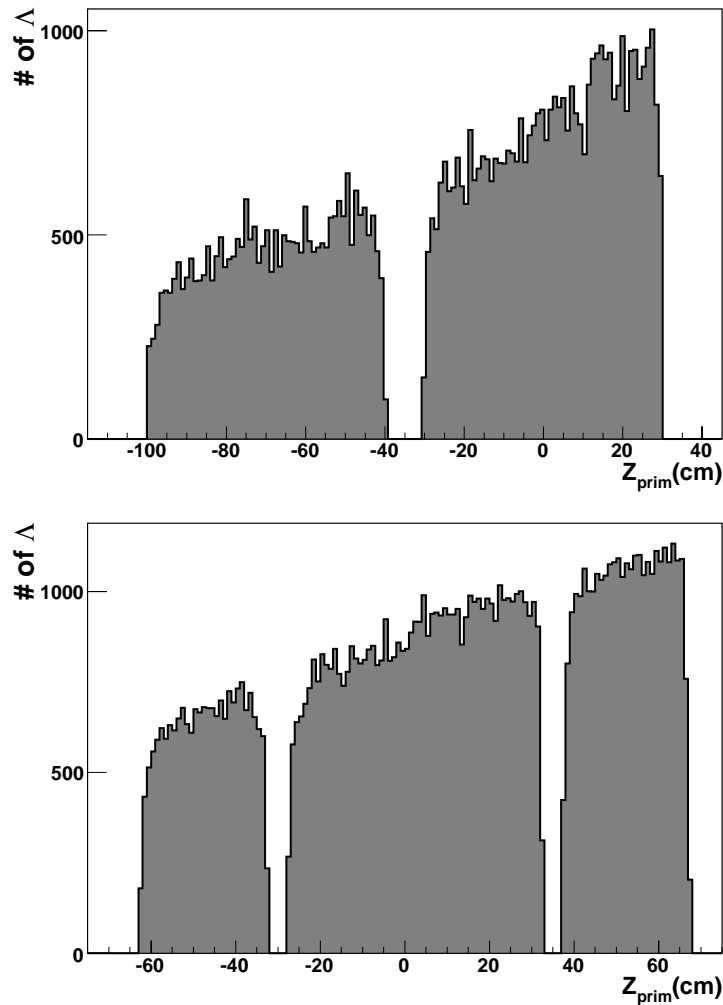
Figure 3.7: Distribution of reconstructed vertex position within the target cells along the beam axis. During the data taking of 2002-2004, two target cells were used (top), while in the 2007 data taking three target cells were implemented (bottom) in a modified position along the z-axis with respect to the 2002-2004 setting.

3.4   Tracking System

Since the COMPASS spectrometer features a large overall acceptance, a variety of tracking stations are employed during the experiment to measure track projections in the plane transverse to the beam direction. The features of the tracking stations change with requirements: Near the beam axis the tracking stations need to work in a high particle flux environment and have a good time and position resolution, while further away from the beam, a larger surface region needs to be covered. The tracking detectors are divided into three groups, which are the Very Small Area Trackers, Small Area Trackers and Large Area Trackers.

The Very Small Area Trackers (VSAT)

The VSAT group consists of two different types of detectors which cover the beam region up to a radial distance of 2.5 cm. Since the beam has a high intensity and the particle rate reaches up to 10^5 s^{-1}mm^{-2}, detectors with a very high time and spatial resolution are needed. Eight stations with scintillating fibres (SciFi) [77] and three silicon detectors (SI) [78] measure the tracks of the incoming beam muons and scattered muons and of the produced hadrons which are traversing at very small polar angles. Each SciFi station is equipped with different planes rotated with respect to each other to measure more than one projection. The scintillating fibres have a diameter between 0.5 and 1 mm and a spatial resolution of 130 to 250 μm. The detection efficiency of the SciFi stations is above 99 % and the time resolution ranges between 350 and 500 ps. The SI detectors are microstrip detectors with an active area of 5×7 cm^2, an average spatial resolution of about 11 μm due to their small pitch of 50 μm, and a time resolution of 2.5 ns. Therefore, the SI detectors are dominantly contributing to the spatial resolution, while the SciFi stations excel in giving a precise timing information of the tracks.

The Small Area Trackers (SAT)

The SAT group covers the intermediate region at a radial distance of 2.5 cm to 40 cm and consists of two types of detectors. The intermediate region features a large hadron multiplicity from the interactions and a high flux from halo muons. Three Micromesh gaseous structure detectors (Micromegas) [79] with an active area of 40×40 cm^2 are positioned between the target and the first analyzing magnet SM1. Additionally, eleven Gas Electron Multiplier detectors (GEM) [80] with an active area of 31×31 cm^2 are stationed throughout the whole spectrometer. Both detector types are gaseous detectors in which the conversion and amplification region are separated, by a thin metal anode grid (micromesh) in the case of the Micromegas and by three 50 μm thin Polyimide foils with a very large number of holes (in the order of 10^4/cm^2) in the case of the GEMs. Both detector types have a central dead zone with a diameter of 5 cm to avoid high occupancy in the high flux area. Likewise, the performances of both detector types is quite similar: The Micromegas feature a detection efficiency of 97 %, time resolution of 9 ns and spatial resolution of 90 μm, while the GEMs exhibit a detection efficiency of 97 %, time resolution of 12 ns and spatial resolution of 70 μm.

The Large Area Trackers (LAT)

The outer radial region shows a lower particle flux and therefore allows for the use of slower detectors, while at the same time ensuring that large angles are also measured by large area trackers. The LAT group contains large area tracking detectors of four different types: Drift chambers (DC) [81], Straw Tube drift chambers (ST) [82], Multi-Wire Proportional Chambers (MWPC) [83] and Large Area Drift Chambers

(DW) [84], which are distributed between the target and behind the second muon filter. Three DC detectors are situated in the first stage of the spectrometer with an active area of 180×127 cm^2 each, with a deactivated center zone of 30 cm diameter to avoid high occupancy. The spatial resolution of the first group of DCs is 190 μm. In the second stage of the spectrometer six more DC detectors are distributed to cover a large area of 500×250 cm^2 (with a 50-100 cm diameter deactivated center zone). The second group of DC detectors are straw tubes made of two layers of thin plastic films. The inner layer consists of a carbon loaded Kapton foil with a thickness of 40 μm which is glued onto the second layer of aluminized Kapton foil of 12 μm thickness. The anode wires are made of gold-plated tungsten with 30 μm diameter. They are centered in the straw tubes by four small plastic spacers, which are positioned at intervals of about 60 cm along each tube. In total 12440 straw tubes are assembled into 15 straw detectors where each detector has an active area of about 280×323 cm^2 with a deactivated center zone of 20×10 cm^2. As a fast counting gas a mixture of Ar-CO$_2$-CF$_4$ is used. For one straw detector (two layers) the average resolution is found to be 190 μm. The ST stations are distributed throughout the spectrometer. The MWPC are mainly responsible for the tracking at large angles. Eleven MWPC stations give a total of 34 planes. The active area of the MWPCs is 178×120 cm^2 with a deactivated center zone of about 2 cm diameter, allowing for a spatial resolution of 1.6 mm. The DW detectors have the largest surface of all LAT detectors and are located further downstream behind the second analyzing magnet SM2. Each chamber has an active area of 5×2.5 m^2 and consists of four sensitive anode wire layers with a wire pitch of 4 cm, separated by layers of cathode wires with a pitch of 2 mm. A mean spatial resolution of 0.5 mm was achieved in the 2004 run.

3.5 Particle Identification

The COMPASS spectrometer features four different types of detectors to ensure an efficient differentiation between detected particles. The first components are Hadron Calorimeters (HCAL). Two HCAL detectors measure the hadron energy, and information from the HCAL detectors is also used in the trigger system. Likewise an Electromagnetic Calorimeter (ECAL) measures the energies of electrons and photons. As described before, the tracks of scattered muons are registered in the Muon Wall (MW) tracking detectors. In the Muon Filters (MF) muons are filtered from tracks of other charged particles. A Ring-Imaging Cherenkov detector (RICH) provides hadron identification of pions, kaons or protons with momenta between 2.5 GeV/c and 43 GeV/c.

The Hadronic Calorimeters (HCAL)

Both Hadron Calorimeters are placed in front of the muon filters and serve two purposes, namely to measure the energy of the hadrons which are produced in the

target material during the scattering process and to trigger on semi-inclusive muon scattering events. The HCALs are sampling calorimeters built with stacks of iron and plastic scintillator plates. Through interactions inside the steel cascading interactions are produced and detected as hadronic showers in the plastic scintillators. To let the high intensity beam pass through the material of the HCALs, a gap is left where beam traversing is anticipated. Since the beam is deflected by SM1 and SM2, the hole is shifted to the Jura side with respect to the center of the HCALs. The HCAL detectors are shielded with lead walls to absorb electromagnetic contamination. The energy resolution of the HCALs are found to be $\sigma/E = 59.4\,\%/\sqrt{E} \otimes 7.6\,\%$ for pions in HCAL1 and $\sigma/E = 65\,\%/\sqrt{E} \otimes 5\,\%$ for pions in HCAL2, where E is given in GeV [85, 86]. The convolution operator $\otimes$ expresses that if the ratio $(\sigma/E)/\sqrt{E}$ results in a value smaller than 7.6 % in HCAL1 or 5 % in HCAL2, respectively, the ratio will not decrease further in value than the values stated behind the $\otimes$ operator.

The Electromagnetic Calorimeters (ECAL)

The Electromagnetic Calorimeter ECAL2 is located in front of HCAL2 and consists of 3000 lead glass modules, which corresponds to 16 radiation lengths in thickness each. A high-energy gamma ray or an electron crossing the lead glass is absorbed fully, and the energy of the photon or electron can be measured. The ECAL2 provides energy information of these electromagnetic interacting particles. Hadrons have a larger interaction length and can only be detected through their full absorption in the HCAL2. Up to the data taking in 2004 only the second stage of the spectrometer featured an Electromagnetic Calorimeter. The energy and spatial resolution of ECAL2 has been measured to be $\sigma/E = 5.5\,\%/\sqrt{E} \otimes 1.5\,\%$ and $\sigma_x = 6\ \text{mm}/\sqrt{E} \otimes 0.5\ \text{mm}$ where E is given in GeV [87]. In 2006 a corresponding Electromagnetic Calorimeter ECAL1 was installed in the first stage of the spectrometer. The ECAL1 contains three types of lead glass blocks, namely GAMS, Mainz and OLGA types. All three types of lead glass blocks were produced from similar materials and have practically the same energy resolution as the ECAL2. Spatial resolution for the GAMS blocks is $\sigma_x = 6\ \text{mm}/\sqrt{E} \otimes 0.5\ \text{mm}$. For the Mainz blocks the spatial resolution is $\sigma_x = 12\ \text{mm}/\sqrt{E} \otimes 0.5\ \text{mm}$. Since the OLGA blocks have a large transverse size of $140 \times 140\ \text{mm}^2$ relatively to the size of an electromagnetic shower, it is only possible to measure spatial information if the electromagnetic shower occurs near the boundary of a block; the spatial resolution is then estimated to be $\sigma_x = 25 - 30\ \text{mm}/\sqrt{E}$. If photons or electrons hit the center of an OLGA block and the full energy of the photon or electron is deposited exclusively inside this particular block, no energy deposit is registered in neighboring blocks and, thus, it is not possible to reconstruct the coordinates of the photon. In this case the spatial resolution is estimated to be $\sigma_x = 140\ \text{mm}/\sqrt{E}$ [88].

The Muon Detectors

Both Muon Wall (MW) detectors cover a large surface of $\approx 4 \times 2\ \text{m}^2$. In the first

stage of the spectrometer, MW1 is placed behind HCAL1 with its 60 cm long iron absorber block (MF1) and works as a gaseous wire chamber with plastic streamer tubes (Iarocci-Tubes) [89]. High energy hadrons are not able to traverse the absorber; only muons with their larger penetration length reach the MW1 detector and create a signal. Thus, the muon walls are able to identify muons. MW1 is built with two planes, each in X and Y direction, and has an average tracking efficiency of $\approx$ 91 % per plane. MW2 is located behind SM2 with a 2.4 m long concrete block working as an absorber (MF2). MW2 consists of drift tubes measuring in three planes X, Y and V, and has an average tracking efficiency of $\approx$ 81 % to 84 % per plane.

The RICH
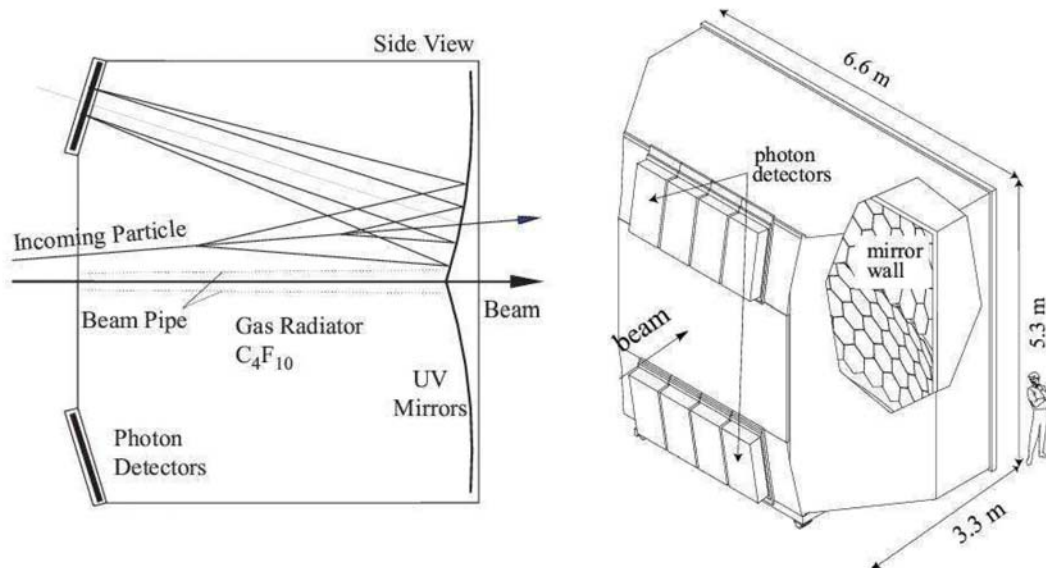
Figure 3.8: COMPASS RICH-1: Principal and artistic view [90].

The Ring-Imaging Cherenkov detector plays a crucial role in identifying hadrons as pions, kaons or protons with momenta in a range from 2.5 GeV/c to 43 GeV/c [91]. The large-size RICH employed in the COMPASS experiment covers the full angular acceptance of $\pm$250 mrad in the horizontal and $\pm$180 mrad in the vertical plane and introduces a minimum of material in the region of the spectrometer acceptance. In Fig. 3.8 the setup of the RICH detector is depicted. The Cherenkov photons which are emitted in the radiator gas are reflected by two spherical mirrors and focused on to the photon detectors. The radiator gas was chosen to be C_4F_{10}, because of its low chromaticity in spite of its high refractive index. Both properties make the gas adequate for hadron identification above 10 GeV/c. In order to obtain enough

Cherenkov photons for this gas the overall length of the radiator vessel needs to be approximately 3 m while the volume of the vessel is 80 m^3. Other requirements for the final setup of the RICH are low background signals, minimum material in the spectrometer acceptance, and the need to operate the CsI photo-cathodes of the proportional chambers (MWPCs) in an environment of reduced particle flux. This reflects in the final setup of the RICH: The photon detectors are located above or below the beam line outside of the spectrometer acceptance. The corresponding mirror system of two spherical mirrors with a total surface larger than 21 m^2 and 6.6 m radius of curvature is located off the beam axis, thus, the Cherenkov ring images are focused on the photon detector surface outside the spectrometer acceptance. The two mirror surfaces are composed of 116 spherical mirror units. The gaps betweens the hexagonal and pentagonal shaped mirrors result in a 4 % loss of reflecting surface. The mirror substrate is borosilicate glass of 7 mm thickness, which corresponds to 5.5 % of a radiation length. The mechanical structure which supports the mirror system has a net-like structure which is designed to minimize the material in the spectrometer acceptance. The overall material used for the support structure is equivalent to 2.5 % of a radiation length. The photon sensitive area of the RICH is 5.6 m^2 in surface and it is covered by eight MWPCs. This is the largest photon detection system of this kind in operation so far. The MWPCs are equipped with CsI photon converter layers which convert the detected photons into electrons. The large photocathode elements must never be exposed to air after being coated with the CsI layer because impurities and water vapour will degrade its efficiency.

Since the luminosity has increased during COMPASS data taking, the RICH detector has been upgraded in 2006 to improve the deadtime of the RICH read-out from 3 μs to 400 ns, which successfully suppresses a larger fraction of uncorrelated background. Two complementary technologies have been implemented in this upgrade. First, both the photon detectors and the readout system in the most sensitive central region are replaced with a new photon detection system based on Multi-Anode Photo-Multiplier Tubes (MAPMT). These MAPMTs replace the four central photo-cathodes of the CsI MWPCs, which corresponds to 25 % of the total active surface. Each MAPMT is coupled to a telescope formed by a field lens and a concentrator lens. Second, in the peripheral region the existing photon detectors are kept while their readout electronics are replaced with a much faster readout system based on a chip which is already used for the readout of the GEM and Silicon detectors at COMPASS. The RICH detector features an improved resolution of 2.5 σ for pion and kaon separation up to a momentum of 43 GeV/c.

3.6   Trigger System

The purpose of a trigger system is to identify events with a specific kinematic signature while effectively suppressing background events in a highly crowded environ-

ment. Since the COMPASS experiment receives high rates of events, it is necessary for the trigger system to react within a decision time of 500 ns and with as little dead time as possible in order to not lose too many relevant events. The trigger system controls the readout of the detectors and the front-end electronics [92].

At the COMPASS experiment the trigger system consists of fast scintillator hodoscopes, a veto system and two hadronic calorimeters. Due to the wide range of physics programs investigated at the COMPASS experiment several types of triggers are needed.
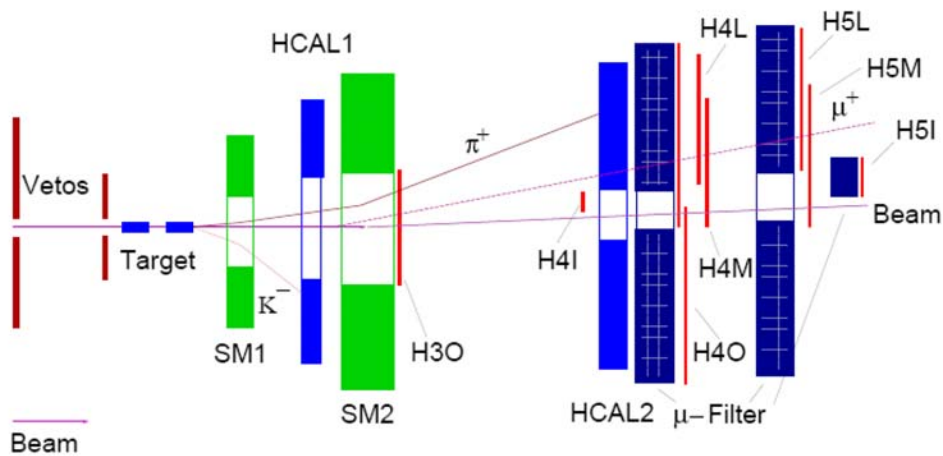
Figure 3.9: Schematic view of the trigger components in the experimental setup. In the shown event the trigger is activated by the planes H4L, H5L, H4M and H5M, which corresponds to a registered muon with $Q^2 < 0.5$ $(\text{GeV/c})^2$. At the same time a pion is detected in HCAL2.

For the investigation of the gluon polarization the trigger is needed to select events containing a muon with $Q^2 \cong 0$ $(\text{GeV/c})^2$ and a large energy transfer $0.2 < y < 0.9$, corresponding to muon scattering angles close to $\theta \approx 0$ mrad. For this purpose three pairs of hodoscope stations (HI, HL and HM)[1] are placed in front of and behind hadron absorbers as shown in Fig. 3.9. The absorbers assure the rejection of electron and hadron tracks in order to trigger exclusively on muon signals. Each hodoscope station consists of 32 vertical scintillating elements whose dimensions are matched with the expected rates at their corresponding locations. The HM features scintillating elements in both projections. The hodoscope stations are located throughout the experiment and are connected via coincidence matrices. The coincidence matrix is adjusted to give a trigger signal when certain deflection angles within the outer magnetic field are detected. The deflection angle is correlated with the energy loss of the muon. Background muons are selected which already started

---

[1]**H**odoscope **I**nner, **L**adder and **M**iddle

with a low initial energy (or which lost energy through muon-electron-scattering or bremsstrahlung). Thus, a minimum energy deposit in the hadronic calorimeters is also required to eliminate background processes without hadron production, such as elastic scattering off electrons and nuclei. The trigger system has to register energy clusters in the hadronic calorimeter larger than a threshold energy value which are absent in background processes. The principle of the trigger setup is demonstrated in Fig. 3.10.
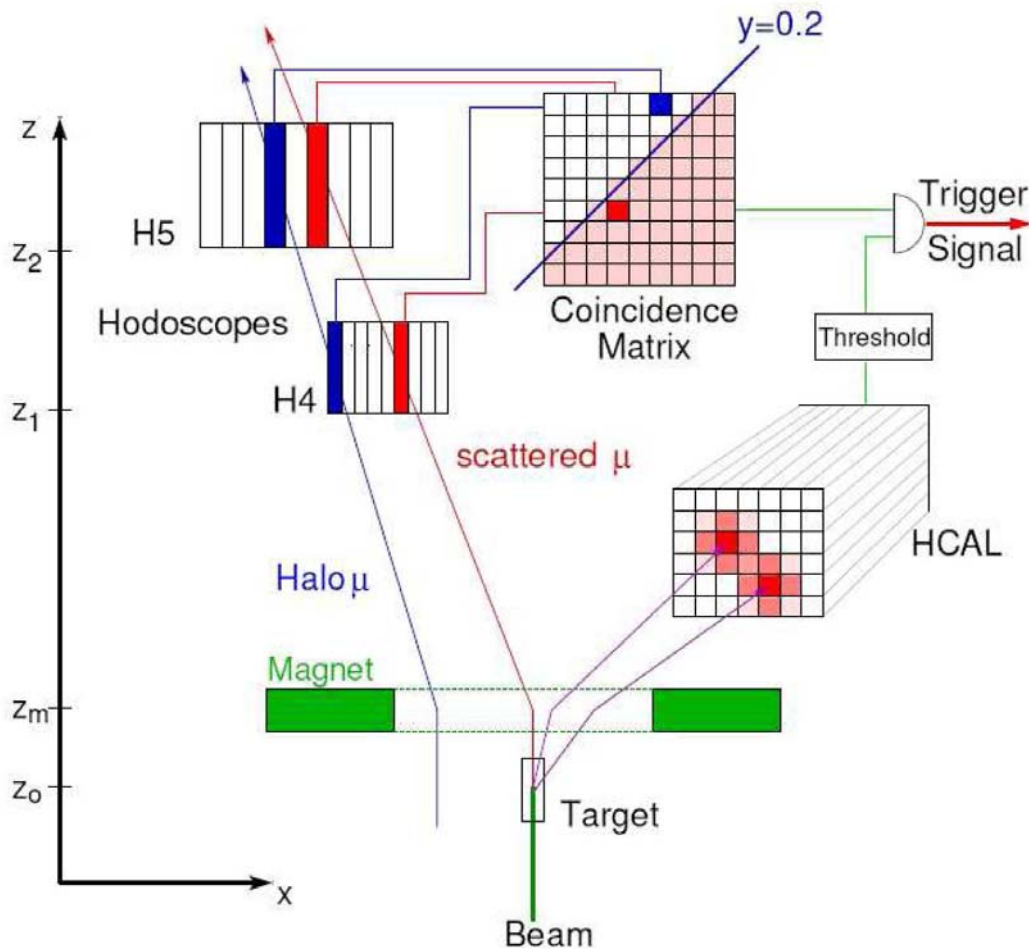
Figure 3.10: Basic scheme of the trigger decision. The scattered muon leads to a coincidence in the activated area of the coincidence matrix while the halo muon fails to do so because its tracks do not point back to the target. In addition, a minimum hadron energy can be required in the calorimeter [72].

To detect a hadron in one of the two hadronic calorimeters it is necessary to find the signal of a cluster with an energy deposition well beyond the value expected for a single muon. To correlate an energy deposition with a scattering event on the

trigger level a time resolution in the order of 1 ns of the calorimeter is necessary to reduce the number of coincidental coincidences. The size of an energy cluster corresponding to a hadron is about 20×20 cm^2. A typical threshold to suppress 90 % of single muon events is 8 GeV/c in the 2004 data taking.

On the other hand one usually requires events where the muon's four-momentum Q^2 is larger than 0.1 (GeV/c)^2 in order to ensure that the virtual photon made a deep-inelastic reaction. At the COMPASS experiment, the trigger for deep-inelastic events selects events with $Q^2 > 0.5$ (GeV/c)^2 in the y-range from 0 to 0.9. The trigger to select events from deep-inelastic scattering consists of two pairs of hodoscopes, HM and H0^2, which filter muons with a certain deflection angle by a coincidence matrix. As described above, the deflection angle is also correlated with Q^2. No hadronic calorimeter information is used in this trigger setup. This trigger setup is especially important for the determination of the Λ polarization discussed in this thesis.

Muons that have a large distance to the beam axis suggest a large loss of their energy and do not cross the target. To suppress false trigger responses due to these halo muons which traverse the detectors at a large distance to the beam axis, a system of segmented veto detectors is located up to 20 m in front of the target. These segmented veto detectors act as anti-coincidences and veto halo muons, thus, allowing the exclusive selection of muons which hit the target at small angles.

The maximum trigger rate is limited by the event size and the bandwidth of the data transmission from the COMPASS data farm to the CERN data storage system, which is about 30 MByte/s. In 2004, a trigger rate of 14 k events per spill for the inner trigger and 7 k events per spill for the ladder trigger were achieved in coincidence with the calorimetric trigger. At the same time, a trigger rate of 18 k events per spill for the middle trigger and 9.5 k events per spill for the outer trigger was obtained without using calorimetric information. The calorimetric trigger collected 22 k events per spill. Combining all the trigger signals, approximately 70 k events per spill were recorded.

Finally the events which are selected by the different types of trigger are supplemented with additional information by a Trigger Control System (TCS) such as number of spill, number of event and exact time stamp. Combined with this information the trigger signal is further relayed to the data acquisition system.

3.7 Data Acquisition System

Since the data acquisition system at COMPASS needs to process high rates and the trigger signals are created by trigger hodoscope signals at the downstream end

---

^{2}**H**odoscope **M**iddle and **O**uter
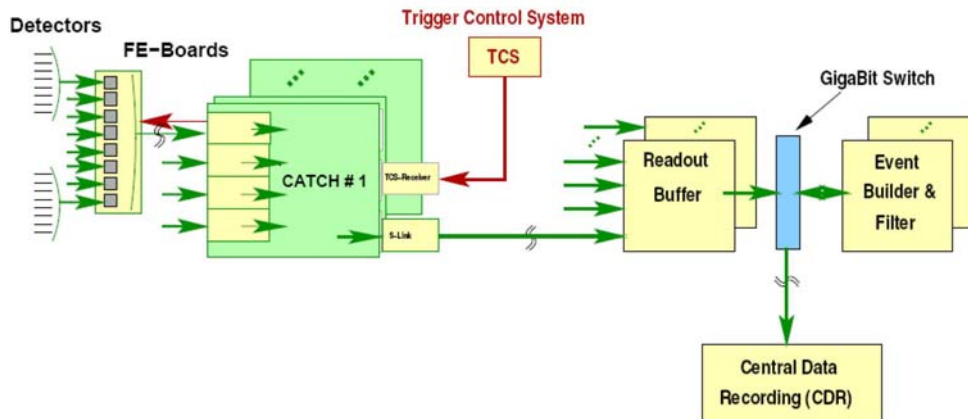
Figure 3.11: General architecture of the data acquisition system at COMPASS. The data recorded by the detectors are transferred via the CATCH system to the readout buffer. After the data have been processed in the event builder they are stored at the CERN computer center.

of the spectrometer, a special concept of pipelining the data was developed. This pipeline concept consists of digitizing and buffering all signals close to the respective recording detectors. In this procedure a time delay is created which allows for the trigger to decide whether the signal is a physics relevant signal or not. A schematic overview of the data acquisition system is shown in Fig. 3.11. The basis of this data acquisition is the same for all types of detectors except for the calorimeters which send their registered information through several hundred meter long delay cables until the trigger decision is received. All other detectors register signal information of the physics events in their front-end cards and digitize the information over so-called CATCH[3] readout-modules. The same CATCH modules are used for all detectors except the GEM detectors and the silicon strip detectors and can, therefore, easily be replaced. Also, the architecture of the data acquisition system in COMPASS is chosen to be very flexible and expandable to allow for upgrades and modifications [93]. The CATCH modules feature a VME[4] technology and are responsible for supplementing the recorded signal data with TCS information. Optical fibres (S-link) transmit the data as optical signals to the readout buffer, where the data are stored for the duration of one spill and tested for consistency. In the break between two spills the data are processed in the event builder. Afterwards the data are transferred to the main computer storage system of CERN, CASTOR[5], which is located several kilometers from the COMPASS experiment. The data are temporarily stored on hard disks and successively migrated to magnetic tapes at the hierarchical CASTOR system. Since the data recording of 2004 a online filter

---

[3]**COMPASS A**ccumulate, **T**ransfer and **C**ontrol **H**ardware
[4]**V**ersa **M**odule **E**urocard bus
[5]**CERN A**dvanced **Stor**age system

within the event builder is used to increase the efficiency of the trigger and, thus, reduce the data volume stored on data tapes. The readout system also transfers configuration information from computers to the detectors.

In the years 2002, 2003 and 2004, 700 TB of data were recorded on tapes; in the data taking of 2007, approximately 1000 TB of data were saved on tapes. The data are summarized in runs which usually consist of 100 to 200 spills (corresponding to 1.5-2 million events). The runs are grouped to periods of approximately one week each with the exact same experimental conditions. In the case of transversity measurements the data are grouped so that each period consists of data which are recorded with the same target polarization while it is still important to note that the exact same experimental setup needs to be in place between periods. I.e., if one detector was not working properly in one period, the information of this specific detector must also not be used in the other period of the corresponding pair of periods.

As soon as the configuration details of each detector are available, the raw data can be processed. Runs which show anomalies are excluded. The software CORAL[6] decodes the recorded data and provides additional information such as vertex positions, particle tracks and RICH information. The additional information also allows the further reduction of data volume based on physics quantities, thus, the data can afterwards be processed faster. The processed data are stored in a mDST[7] format. The investigation of physics signatures of the mDST's is conducted with the PHAST[8] software package which has been designed by the COMPASS collaboration.

---

[6]**CO**MPASS **R**econstruction and **A**nalysis Framework
[7]**m**ini **D**ata **S**ummary **T**ape
[8]**P**hysics **A**nalysis **S**oftware and **T**ools

Chapter 4

Reconstruction of Λ^0 Events

An analysis has been conducted to gain insight into the spin transfer from a quark to Λ hyperons during the fragmentation process by extracting the polarization of the produced Λ hyperons. In this chapter the topology of events which were used to extract the Λ polarization as well as the specific cuts and techniques which were used to obtain the final data set are described. The kinematic properties of the selected events of the final set are also demonstrated.

4.1 Data Reconstruction

The analysis of this thesis is based on the data collected with a transversely polarized proton target at the COMPASS experiment in the year 2007. The data set included in this analysis consists of pairs of data taking periods W25 & W26, W27 & W28, W30 & W31, W39 & W40, W41 & W42a and W43 & W42b.

The data which are collected by the detectors are stored by the DAQ system as raw data files. The raw data files usually consist of one run which equals 200 spills and roughly one hour of beam time and contain digitized detector information. In order to access the physics events the raw data have to be processed first, which means that the physical information has to be extracted from the recorded detector signals. This procedure is performed by the COMPASS Reconstruction and Analysis software CORAL [94], which is a fully object-oriented program written in C++ with a modular architecture.

To compute the track and vertex reconstruction two initial phases are required. The first phase is called decoding; here the hit information from the detector channels are extracted from the raw data. The second phase is called clusterization, which means that the detector channels are grouped together according to the passage of the same particle. Here, the hit position of the particle traversing through every detector plane is stored in terms of absolute values in the main reference system of the apparatus. The exact geometrical position of each detector is read from a file where the alignment information is stored. The hit clusters are consecutively

selected based on time calibration. After this selection, charged and neutral particles are identified and their tracks are reconstructed. To reconstruct the trajectories of charged particles on their way through the spectrometer, information from the tracking detectors are used. Calorimetric information is used to differentiate between muons and hadrons and to compute the energy of photons.

Track reconstruction is achieved by processing the data in three distinct phases, which are pattern recognition, bridging and global fitting. The procedure of pattern recognition selects hits in all detector planes which are expected to stem from a single particle and groups them to track segments according to five separate zones of the spectrometer. The track segment candidates are expected to be straight lines. The track segments which are found are combined by extrapolation and a χ^2 fit to form a complete track of a particle traversing the spectrometer, which is the bridging procedure. This procedure includes deviations from a straight line of the traversing particle in magnetic fields by taking magnetic fields and material maps of the spectrometer into account. The best estimators for the parameters of the reconstructed tracks are computed and the track candidates are selected with a quality function which includes a χ^2 fit. This concludes the global fitting procedure.

After the track reconstruction, a vertex reconstruction is applied. Whenever various tracks seem to originate from a common point in space within a physics event, it is aimed to find the best estimator of the three coordinates of the vertex position from each track that is assumed to stem from this interaction point. A χ^2 fit is performed to judge the probability of this particular vertex to exist. An approximation of the primary vertex is achieved by computing the average point of closest approach between one beam track and all possible outgoing tracks.

After the reconstruction phase, all physics information such as track parameters, vertices, calorimetric clusters, particle identification probabilities, detector hit patterns etc. are stored into output ROOT trees in a mDST file. The data reduction factor between raw input data and mDST output data is approximately 100. The output mDST files are stored on the CASTOR storage system of CERN. When a file is requested by an user, the CASTOR downloads a copy of this file from tape on to a local disc for access.

The reconstructed data in the mDST files are analyzed with the software package PHAST [95], which was developed for the needs of the COMPASS experiment and its analyses. The PHAST package is based on the standard ROOT framework [96] which has been developed at CERN for high energy physics and which is a useful tool to display, store and fit complex physics data. In this analysis, PHAST version 7.058 has been used in the batch system of CERN to analyze mDST files.

4.2 Event Topology and Selection
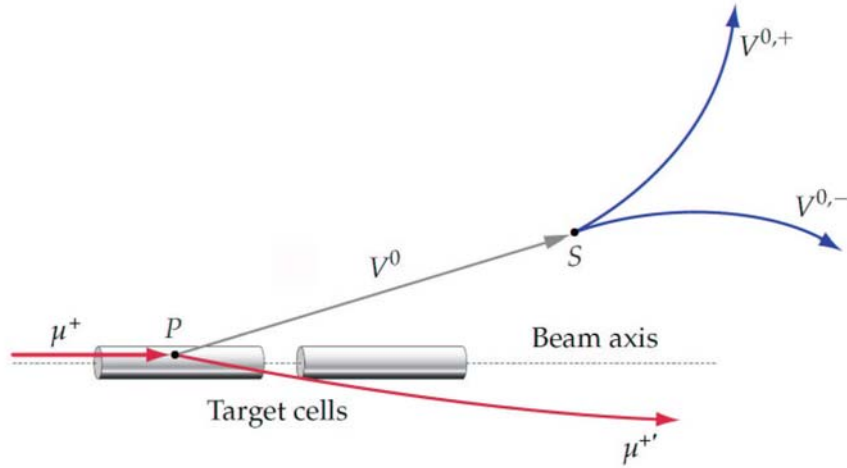
Figure 4.1: Typical topology of a V^0 event with a neutral V^0 particle [97] in a magnetic field: An incoming beam muon μ^+ scatters off of a target nucleon in the primary vertex point P. A neutral V^0 particle is created which cannot be detected in the apparatus. At the secondary interaction point S the V^0 particle decays into two tracks with opposite charges.

The Λ hyperon is a neutral particle and, therefore, it cannot be detected in the detectors. The only possibility to identify the Λ hyperon is to detect its two charged decay particles in the Λ decay channel $\Lambda \to p\pi^-$ (B.R. 64 %), which are a positively charged proton and a negatively charged pion. In the case of a $\overline{\Lambda}$, the hyperon decays into an antiproton and a positively charged pion. The typical signature of such a Λ decay in a magnetic field is shown in Fig. 4.1: The V^0 particle cannot be seen in the spectrometer; from a secondary vertex S two oppositely charged tracks appear downstream of the target.

The identification of charged particles can in principle be achieved by employing the RICH detector which is described in Section 3.5. However, the traditional way of particle identification through the RICH is not applied in this analysis, because the threshold to identify pions and protons is relatively high and would, therefore, limit the statistics of Λ hyperons too much. The threshold of the RICH to identify a proton requires the proton momentum to be larger than 17 GeV/c, while most of the proton momenta in the data of this analysis are below this threshold.

The event selection in this analysis is performed in two steps: In a first step a generic V^0 data set is selected by applying kinematic cuts. The Λ hyperons are reconstructed from their charged decay particles. In a second step, a novel RICH veto condition is used to further reduce the background by rejecting electrons, pions and kaons which were falsely assumed to be the decay proton of the Λ decay. By

applying the RICH particle identification as a veto condition it is possible to reduce the background without limiting the signal statistics due to the high thresholds; this procedure will be explained in Section 4.2.4.

As mentioned above, the analysis of this thesis is based on the data collected with a transversely polarized proton target at the COMPASS experiment in the year 2007. The data set included in this analysis consists of the data taking periods W25, W26, W27, W28, W30, W31, W39, W40, W41, W42 and W43. The data set which has been used in this analysis is produced in production slot "0hn" for all data taking periods except W27, W39 and W42. These three periods were included in this analysis in their production version "0hm" to fulfill internal quality standards. For the 2007 data set, a bad spill list, which has been computed as a quality check for the 2007 transversity data set [98], has been taken into account in the event selection.

4.2.1   Selection of Primary Vertices

The following selection cuts have been applied to select the primary events. The detectors which are employed for these cuts are shown in Fig. 3.1. In Table 4.2 the number of events of the whole 2007 data set after applying each of these cuts is summarized.

1. Bad runs and bad spills are excluded to ensure a stable data quality.

2. The best primary vertex is selected by requiring the maximum number of tracks and smallest χ^2 of the vertex (if more than one primary vertex was reconstructed).

3. If a scattered muon of the muon beam is detected, the corresponding hit in the hodoscope behind the second muon filter must have an extrapolated primary track pointing to the entrance of the target within a 5 cm radius and a distance of less than 1.9 cm from the beam axis.

4. If no scattered muon is detected in the hodoscopes, a muon recovery function in the PHAST procedure, GetMW1ScatMuon, is executed. A recovered scattered muon is identified if the track has at least 4 hits in the first half and 6 hits in the second half of the muon wall 1.

5. The scattered muon must not traverse into the yoke of SM2, where the magnetic field is not described in CORAL.

6. The scattered muon must traverse at least 30 radiation lengths, $X/X_0 > 30$, because traversing through this amount of material ensures that the particle is a muon.

7. The primary vertex must be within the three target cells with $r < 1.9$ cm, where $r = (x^2 + y^2)^{1/2}$. In reality, the target radius is 2 cm. The smaller cut is meant to compensate for imperfect alignment of the target.

8. The incoming muon must have a projected trajectory that crosses all target cells to equalize the beam flux through the target cells.

9. The squared momentum transfer Q^2 must be $Q^2 > 1.0$ GeV/c^2 to select DIS events.

10. The fractional energy transfer of the projectile from the incoming lepton to the nucleon y must be in the range $0.1 < y < 0.9$: On one hand, the events at low values of y correspond to quasi-real photon events with small Q^2. Since we investigate events in the DIS region with high Q^2, we therefore select events with $y > 0.1$. The lowest possible value of y is mainly limited by the inner trigger of the COMPASS setup. On the other hand, events with a high value of y are discarded because they are affected by radiative effects, and consequently their systematic uncertainties become too large to be included.

4.2.2   Selection of Secondary Vertices

The following selection cuts have been applied to select the $\Lambda(V^0)$ events. The detectors which are employed for these cuts are shown in Fig. 3.1. In Table 4.2 the number of events of the whole 2007 data set after applying each of these cuts is summarized.

1. Both decay hadrons must traverse less than 10 radiation lengths, $X/X_0 < 10$.

2. To be able to precisely measure the momenta of the decay particles and, thus, reconstruct the V^0 mass, the daughter tracks are required to fully traverse the first spectrometer magnet SM1. This is accomplished by requiring that the last measured hit associated with the track must have a z-coordinate larger than 350 cm. This cut was introduced due to the fact that fringe field tracks of the decay hadrons which end before the SM1 magnet have a much lower reconstruction precision.

3. Tracks with very low momenta are extremely sensitive to magnetic fields, thus, making track and vertex reconstruction unreliable due to the complicated interference of the magnetic fields of the target solenoid and the SM1. Therefore, the momenta of both decay particles are required to be larger than 1 GeV/c, $p^\pm > 1$ GeV/c.

4. Both V^0 tracks must not have their origin assigned to any primary vertex in order to further reduce the background.

5. In the decay of V^0 exactly one positively and one negatively charged outgoing track has to be present.

6. The daughter hadron tracks $h^\pm$ must not cross into the yoke of SM2, where the magnetic field is not described in CORAL.

7. The collinearity angle between the reconstructed Λ momentum and the direction of primary and secondary vertex, $\theta_{col} = acos\left(\frac{\vec{p}_{V^0}\cdot\vec{r}(r_{prim},r_{sec})}{|\vec{p}_{V^0}|\cdot|\vec{r}(r_{prim},r_{sec})|}\right)$, is required to be smaller than 10 mrad, as shown in Fig. 4.2. This criterion ensures that the Λ is produced in the direct production mechanism and that it stems from the primary vertex. Another way to produce a Λ hyperon is the decay from heavier hyperons like Σ or Ξ. In this production mechanism, the created Λ has a higher transverse momentum with respect to the heavier hyperons due to an additional γ or π track. These events are reduced by limiting the collinearity angle.
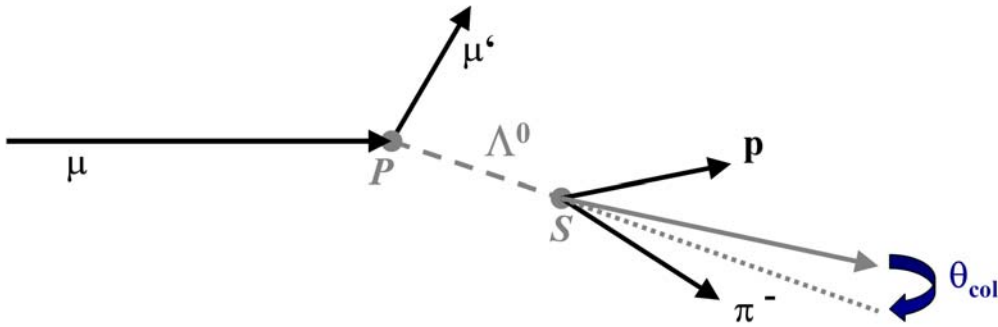
Figure 4.2: Typical topology of a V^0 event: An incoming beam muon μ scatters off a target nucleon in the primary vertex point P and is deflected to be an outgoing muon μ'. A neutral Λ^0 particle is created which cannot be detected in the spectrometer. At the secondary interaction point S the Λ^0 particle decays into two tracks with opposite charges, a positively charged proton p and a negatively charged pion π^-. The collinearity angle θ_{col} is the angle between the extension of the connecting vector between the primary and secondary vertices and the combined reconstructed momentum vector of the proton and the pion.

8. The transverse momentum p_T of the positive decay particle with respect to the V^0 momentum is required to be larger than 23 MeV/c, $p_T > 23$ MeV/c, in order to eliminate the background of e^+e^- pairs from γ conversion which display a broad background distribution at low p_T.

9. The decay length D must be larger than 7.5 times the error of the decay length σ_D given by the errors of the two vertices, $D > 7.5\sigma_D$. If the Λ decay is too close to the primary vertex, the Λ particles cannot be properly reconstructed. In Fig. 4.3 the Figure of Merit $\left(FoM = \frac{S^2}{S+B}\right)$, number of Λ particles, and the mass resolution σ_Λ from the Gaussian fit of the invariant mass distributions with application of the $D > x \cdot \sigma_D$ cut in a range from $x = 0$ to 10 are shown. The mass resolution σ_Λ stays constant regardless of the value of the FoM cut. Since the FoM has its maximum value at $7.5\sigma_D$, while the number

of Λ hyperons does not decrease by a lot at this FoM cut, the cut is most effective at this value.
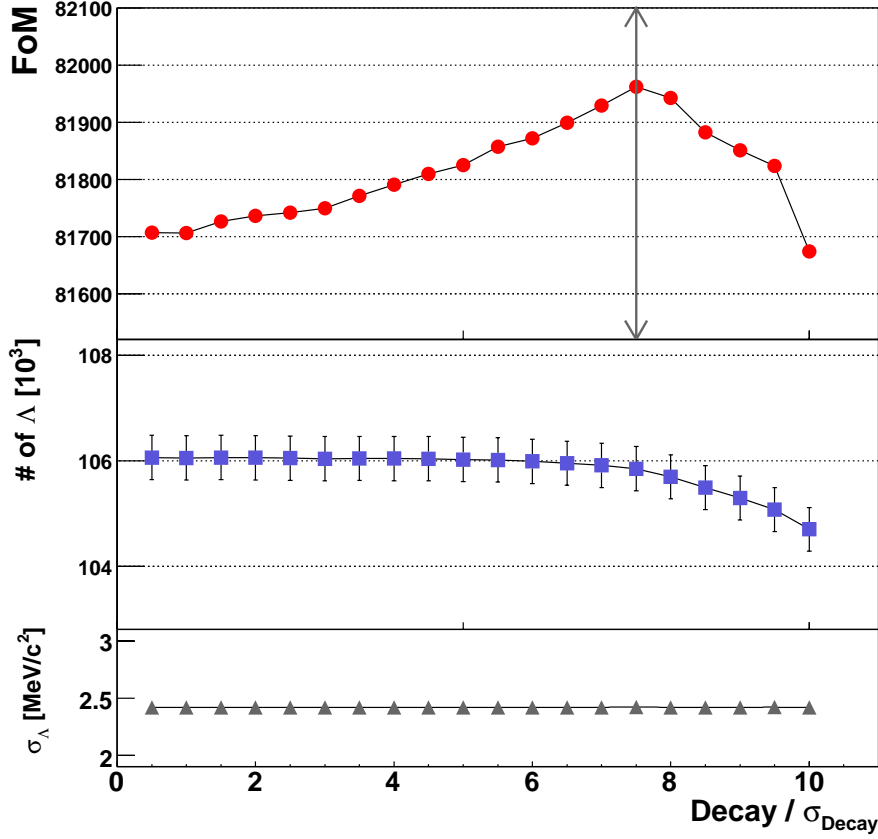
Figure 4.3: The Figure of Merit $\left(FoM = \frac{S^2}{S+B}\right)$, number of Λ particles, and the mass resolution σ_Λ from the Gaussian fit of the invariant mass distributions with application of the $D > x \cdot \sigma_D$ cut in a range from $x = 0$ to 10 are shown. The grey arrow in the top panel indicates the optimized value of the FoM at $D > 7.5\sigma_D$.

4.2.3 Armenteros-Podolanski Plot

A novel method to investigate the decays of neutral particles was developed by R. Armenteros and J. Podolanski in 1954 [99]. The measured four-momenta of the two daughter particles of the V^0 decays are used to calculate two variables, the transverse momentum p_T and the longitudinal momentum asymmetry $\alpha = \left(p_L^+ - p_L^-\right)/\left(p_L^+ + p_L^-\right)$. Here, the subscript "$L$" indicates that the direction of motion of the V^0 rest frame in the laboratory frame is defined as the longitudinal direction "L". The longitudinal momentum p_L^* of the decay hadrons in the V^0 rest frame is given by the expression $p_L^* = p\cos\theta$, where p is the momentum and θ is the polar angle with respect to the V^0 direction of motion L. The two decay particles in the V^0 rest frame are connected via the expression $p_L^{*+} = -p_L^{*-}$. By taking the

velocity of the V^0 in the laboratory frame β into account, a Lorentz transformation from the V^0 rest frame to the laboratory frame results in

$$p_L^{\pm} = \gamma \left(p_L^{*\pm} + \beta E^{*\pm} \right), \tag{4.1}$$

with

$$
\begin{aligned}
E^{*\pm} &= \frac{1}{2m_{V^0}} \left(m_{V^0}^2 + \left(m^{\pm} \right)^2 - \left(m^{\mp} \right)^2 \right), \\
\gamma &= \left(1 - \beta^2 \right)^{-\frac{1}{2}}.
\end{aligned} \tag{4.2}
$$

The momentum asymmetry α is calculated from the longitudinal momenta $p_L^{\pm}$ in the laboratory frame,

$$
\begin{aligned}
\alpha &= \frac{p_L^+ - p_L^-}{p_L^+ + p_L^-} \\
&= \frac{\gamma \left(p \cos \theta + \beta E^+ \right) - \gamma \left(-p \cos \theta + \beta E^- \right)}{\gamma \left(p \cos \theta + \beta E^+ \right) + \gamma \left(-p \cos \theta + \beta E^- \right)} \\
&= \frac{2p \cos \theta + \beta \left(E^+ - E^- \right)}{\beta \left(E^+ + E^- \right)} \\
&= \frac{2p \cos \theta + \beta \left(\left(m^+ \right)^2 - \left(m^- \right)^2 \right) / m_{V^0}}{\beta m_{V^0}} \\
&= \frac{2\sqrt{\left(p^2 - p_T^2 \right)}}{\beta m_{V^0}} + \alpha_c,
\end{aligned} \tag{4.3}
$$

where

$$\alpha_c = \frac{\left(m^+ \right)^2 - \left(m^- \right)^2}{m_{V^0}^2}. \tag{4.4}$$

This method to plot the transverse momenta p_T versus the momentum asymmetry α results in a typical distribution, which is called the Armenteros-Podolanski distribution. Different V^0 decays are clearly distinguished in the Armenteros-Podolanski plot as different elliptic arcs, which makes it convenient to differentiate between the different decays of Λ, $\overline{\Lambda}$ or K_S^0 in terms of their respective combination of p_T and α. If the two decay particles have the same mass, the distribution of their decay is symmetrical around $\alpha = 0$ in the Armenteros-Podolanski plot; if they have different masses, the center of the corresponding arc is shifted towards a positive or negative value of α. The center of the arc is given by α_c as stated in Eq. 4.4, while the maximum value of the transverse momentum p_T [100] can be calculated by

$$p_T^{max} = \frac{\sqrt{\left(m_{V^0}^2 - \left(m^+ + m^- \right)^2 \right) \left(m_{V^0}^2 - \left(m^+ - m^- \right)^2 \right)}}{2m_{V^0}}. \tag{4.5}$$
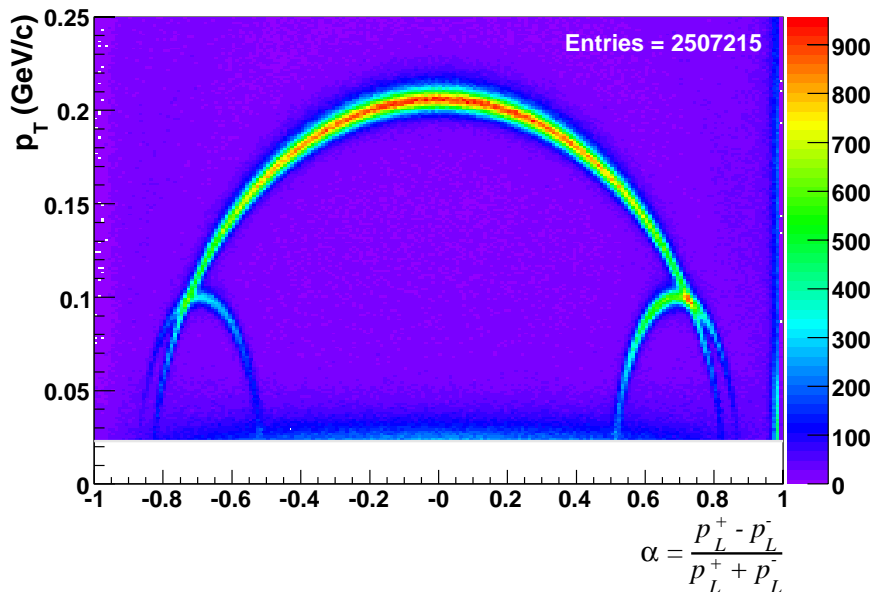
Figure 4.4: Armenteros-Podolanski plot of the V^0 sample after selection cuts. The transverse momenta of the decay particles p_T versus the longitudinal momentum asymmetry α is drawn in order to compare the resulting arcs, which correspond to different decays of Λ, $\overline{\Lambda}$, or K^0. Three prominent ellipses from $\Lambda \to p\pi^-$ at the right side, $\overline{\Lambda} \to \overline{p}\pi^+$ at the left side, and $K_S^0 \to \pi^+\pi^-$ at the top are visible. The decay $\gamma \to e^+e^-$ is suppressed in the range of $p_T < 23$ MeV/c by a kinematical cut.

In Fig. 4.4 the Armenteros-Podolanski plot of the reconstructed V^0 sample of the 2007 data is shown. Three arcs are clearly visible: from $\Lambda \to p\pi^-$ at the right side, $\overline{\Lambda} \to \overline{p}\pi^+$ at the left side, and $K_S^0 \to \pi^+\pi^-$ at the top. The calculated values of the maximum p_T for the K^0 are $p_T^{max} = 0.206$ GeV/c and for the Λ and $\overline{\Lambda}$ are $p_T^{max} = 0.101$ GeV/c, which can be verified by the maximum value of the respective elliptic distribution in Fig. 4.4. The decay $\gamma \to e^+e^-$ is suppressed in the range of $p_T < 23$ MeV/c by the previously described kinematical cut.

In Fig. 4.4 it can be seen that there is an overlap of the arcs from Λ and $\overline{\Lambda}$ events and the background K^0 events at $|\alpha| \approx 0.75$ and $p_T \approx 0.100$ GeV/c. The background K^0 are difficult to eliminate from the sample because they have a similar kinematic signature as the Λ and $\overline{\Lambda}$ decays and, thus, cannot be suppressed by the kinematic cuts which were described in the previous sections. In principle it is possible to suppress the K^0 background by a cut on the invariant mass, however, this cut also removes a non-negligible fraction of the Λ and $\overline{\Lambda}$ events. Since the statistics of the Λ sample is already low to begin with, it is deemed unfavourable to apply an invariant mass cut. A novel veto condition of the RICH detector has been implemented to eliminate the K^0 background while not imposing too strict a limitation on the Λ and $\overline{\Lambda}$ signal sample. This will be described in the following Subsection 4.2.4.

4.2.4 Using RICH as Veto

The RICH detector provides information on particle identification. An outgoing hadron can be identified as pion, kaon or proton in a momentum range from 2.5 GeV/c to 43 GeV/c. The vessel of the RICH detector is filled with C_4F_{10} radiator gas which was chosen to ensure a good resolution also in the high momentum domain. The radiator gas C_4F_{10} features a low chromaticity and a relatively high refractive index. Cherenkov photons which are emitted in this radiator gas are reflected by two spherical mirror surfaces towards a system of photon detectors, where the Cherenkov ring images are registered. The measured Cherenkov angles θ_{ch} in relation with the momentum information (from the magnets and tracking information) enable particle identification in different regions of momenta. The minimum Cherenkov thresholds to identify particles are

- 2.5 GeV/c for pions π

- 9.5 GeV/c for kaons K

- 17 GeV/c for protons p

which is demonstrated in Fig. 4.5. In the momentum region larger than 43 GeV/c the different bands of particles begin to overlap, thus, no reliable particle identification can be made.
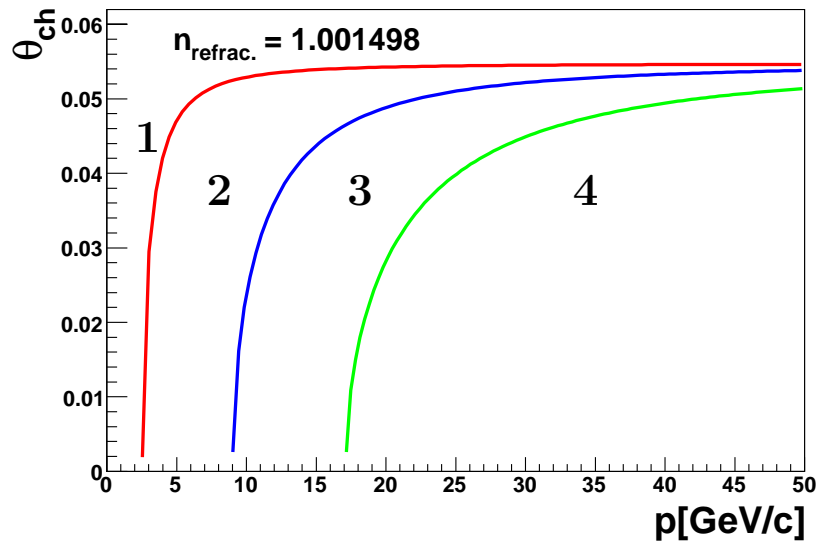
Figure 4.5: Calculated Cherenkov angle θ_{ch} versus momentum p: Momentum thresholds are shown for the detection of three different particles π (in red), K (in blue) and p (in green) at a refractive index n=1.001498. Four different regions (**1**, **2**, **3** and **4**) are defined by those thresholds of momenta [66].
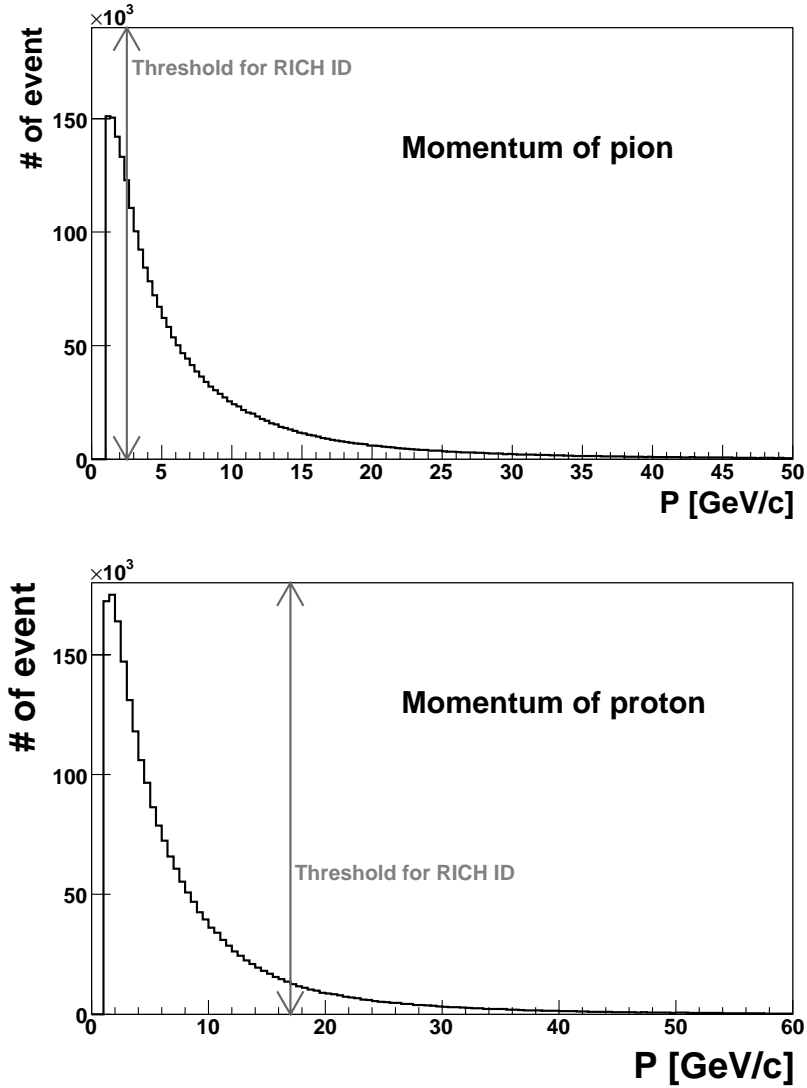
Figure 4.6: Top: Momentum distribution of the pions present in the Λ signal. Bottom: Momentum distribution for protons which contribute to the Λ signal. The grey arrows indicate the thresholds for pion and proton identification by the RICH. A significant amount of data were cut-off if RICH particle identification was implemented in this analysis.

The decays $\Lambda \to p\pi^-$ and $\overline{\Lambda} \to \overline{p}\pi^+$ each have an (anti-)proton and (anti-)pion in their final state. However, since the threshold of momentum to identify a proton or a pion is relatively high, the positive identification of a proton in the decay signature limits the available statistics too much to be applied in this analysis. A momentum distribution of the pions and protons present in the Λ signal is shown in Fig. 4.6. It becomes obvious that the implementation of a positive particle identification by the RICH limits the available statistics noticeably. Therefore, the selection of Λ and $\overline{\Lambda}$ relies solely on rejection of non-proton particles.

The RICH information is used to reject electrons, pions, and kaons (where a proton is expected in the signal signature) from the sample. If a particle in the signature of the Λ decay is identified by the RICH likelihood function to be an electron, pion, or kaon, although instead a proton is expected in the Λ decay, the event is discarded. The hadron identification with the information of the RICH detector is based on a likelihood method. For each track that is considered in the signal sample of this analysis, the likelihood function is calculated for five mass hypotheses, namely that this track originates from an electron, pion, kaon, proton, and background. To apply the rejection of non-proton candidates with RICH information, four different momentum regions according to the thresholds of π, K^0, and p identification as shown in Fig. 4.5 are considered,

- Region 1: $p <$ Threshold(π). Rejection of e is possible.

- Region 2: Threshold$(\pi) < p <$ Threshold(K). Rejection of e and π is possible.

- Region 3: Threshold$(K) < p <$ Threshold(p). Rejection of e, π and K is possible.

- Region 4: Threshold$(p) < p$. Rejection of e, π and K is possible.
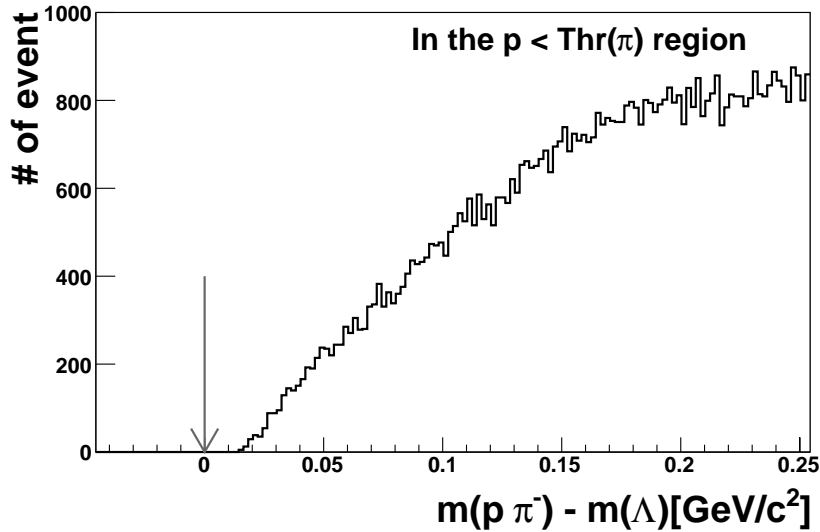
Figure 4.7: Invariant mass distribution in the region of $p < Thr(\pi)$. It can be seen that low momentum particles do not contribute to the non-existent Λ signal at the expected location as indicated by the grey arrow.

In region 1 at momenta of the proton candidate below ≈ 2.5 GeV/c, the rejection of electrons is not necessary. In Fig. 4.7 the invariant mass distribution in the region of $p < Thr(\pi)$ is shown, where it becomes obvious that protons in the low momentum domain do not contribute to an expected Λ signal peak which is indicated

by the grey arrow. To see a reconstructed Λ signal, the momentum of the proton candidate must be larger than 2.5 GeV/c. Furthermore, the threshold to detect a pion is about 2.53 GeV/c at a refractive index $n = 1.001498$, therefore, no RICH cut needs to be applied in region 1. In region 2, rejection is achieved for e and π but not for K since kaons cannot be identified in this momentum region. Since the effect of e contamination in the momentum range of regions 3 and 4 is negligible and the contaminated events lie quite far away from the signal window in the invariant mass distribution, a veto on e can safely be omitted, while a rejection condition of π and K is implemented.

To reject $e^{\pm}$, $\pi^{\pm}$, and $K^{\pm}$, some cuts on the calculated likelihood functions $LH_{e,\pi,K}/LH_{background}$ have been optimized. A maximum Figure of Merit $\left(FoM = \frac{S^2}{S+B}\right)$ can be found after applying the RICH likelihood cut with varying ratios of $LH_{e,\pi,K}/LH_{background}$ for each of those four threshold regions separately. The FoMs and the numbers of signal are shown for each region in Fig. 4.8 for Λ and in Fig. 4.9 for $\overline{\Lambda}$, respectively. The optimized likelihood cut corresponds to the respective maximum value of the FoM and is summarized in Table 4.1.

Table 4.1: Summary of the RICH cuts to reject electrons e, pions π, kaons K by means of likelihood calculations for e, π, K and background bk.

Threshold of momentum	Rejection of	Likelihood cut
Λ		
p < Thr(π)	e	No
Thr(π) < p < Thr(K)	e & π	LH(e)/LH(bk) < 2.3 & LH(π)/LH(bk) < 2.2
Thr(K) < p < Thr(p)	π & K	LH(π)/LH(bk) < 2.5 & LH(K)/LH(bk) < 3.0
Thr(p) < p	π & K	LH(π)/LH(bk) < 2.5 & LH(K)/LH(bk) < 2.4
$\overline{\Lambda}$		
p < Thr(π)	e	No
Thr(π) < p < Thr(K)	e & π	LH(e)/LH(bk) < 1.9 & LH(π)/LH(bk) < 1.9
Thr(K) < p < Thr(p)	π & K	LH(π)/LH(bk) < 2.2 & LH(K)/LH(bk) < 3.0
Thr(p) < p	π & K	LH(π)/LH(bk) < 2.4 & LH(K)/LH(bk) < 2.2
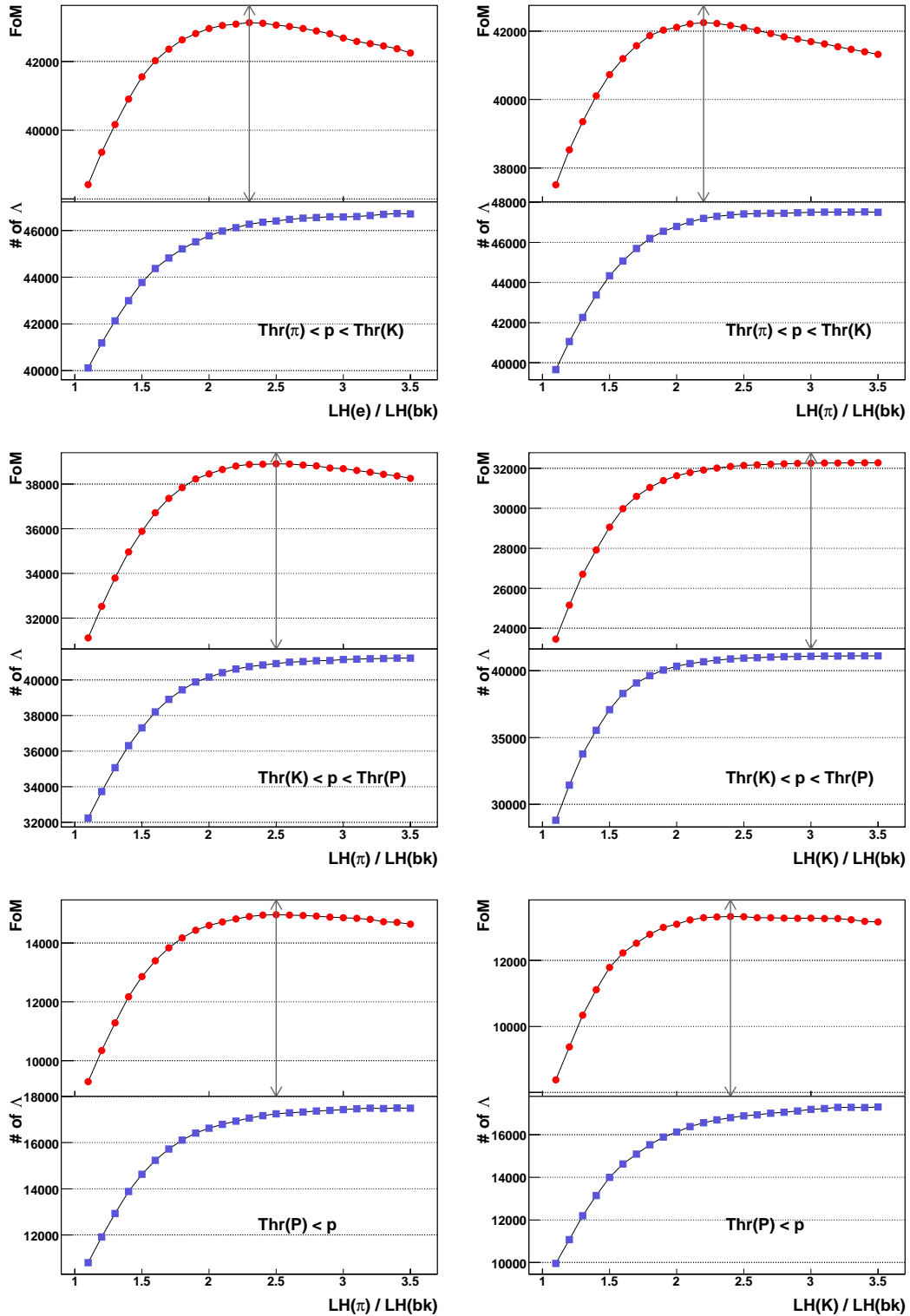
Figure 4.8: Figure of Merits (FoM) in the range of momentum at $\mathrm{Thr}(\pi) < \mathrm{p} < \mathrm{Thr}(K)$, $\mathrm{Thr}(K) < \mathrm{p} < \mathrm{Thr}(p)$, and $\mathrm{Thr}(p) < \mathrm{p}$ for Λ selection.

Figure 4.9: Figure of Merits (FoM) in the range of momentum at $\mathrm{Thr}(\pi) < \mathrm{p} < \mathrm{Thr}(K)$, $\mathrm{Thr}(K) < \mathrm{p} < \mathrm{Thr}(p)$, and $\mathrm{Thr}(p) < \mathrm{p}$ for $\overline{\Lambda}$ selection.

The Armenteros-Podolanski plot of the signal sample after applying the RICH likelihood rejection is shown in Fig. 4.10. The signal sample contains much less contamination from K^0 events, while still maintaining a good statistics of the Λ and $\overline{\Lambda}$ signal events. The veto of the RICH likelihood on false proton candidates proves useful in the area of $|\alpha| \approx 0.75$ and $p_T \approx 0.100$ GeV/c in the Armenteros-Podolanski distribution as now the K^0 background which could not be suppressed by kinematic cuts is greatly reduced as compared to Fig. 4.4 where no RICH likelihood rejection was implemented.
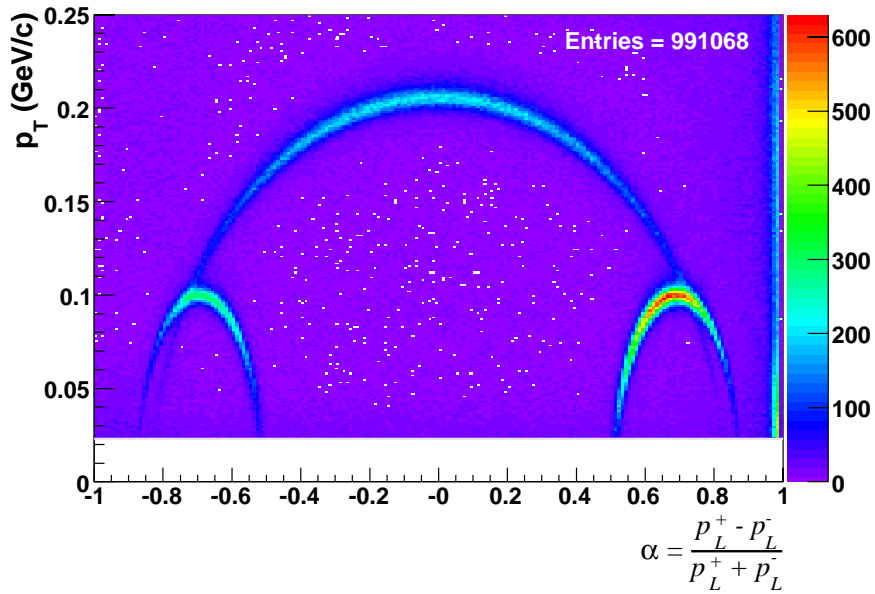
Figure 4.10: Armenteros-Podolanski plot of the V^0 sample after selection cuts and after RICH cut. Two prominent ellipses from Λ and $\overline{\Lambda}$ are visible, the K^0 background is strongly reduced.

4.2.5 Invariant Mass Distributions for Λ and $\overline{\Lambda}$ Hyperons

For the V^0 events which passed all introduced cuts, a mass assumption is made for the two decay particles in order to calculate the invariant mass. Those combinations of decay tracks for which the mass assumption is correct will accumulate in a signal peak close to the V^0 mass. The peaks have the natural width, which is correlated to the lifetime of the corresponding particle, e.g. 2.50 μeV for Λ and $\overline{\Lambda}$, and 7.35 μeV for K^0, but they are smeared out by measured widths $\sigma_\Lambda \approx 2.3$ MeV/c and $\sigma_{K^0} \approx 6.3$ MeV/c. Thus, the widths of the measured peaks reflect solely the resolution of the spectrometer.

In Figs. 4.11 and 4.12 the mass distributions and a section of the Armenteros-Podolanski plot are shown for the Λ and $\overline{\Lambda}$ hyperon of the 2007 data, respectively. In the left-up panel, the invariant mass distributions of the hyperons with and without
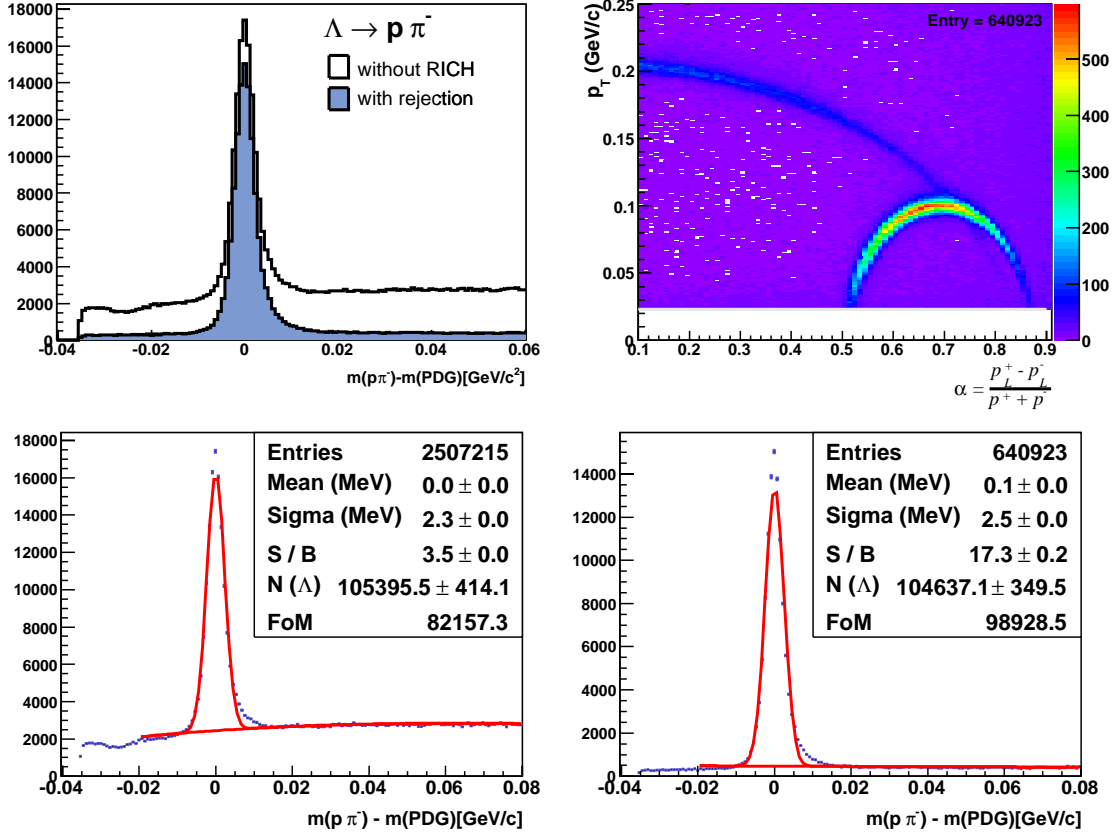
Figure 4.11: Left-up: Invariant mass distribution of Λ with and without RICH cut. Right-up: Armenteros-Podolanski plot with RICH cut in $\alpha > 0$. Left-down: Result of Gaussian fit for data without RICH cut. Right-down: Result of Gaussian fit for data with RICH cut.

the RICH cut are compared. It is clearly visible that the background, consisting mostly of kaon events which decay into $\pi^+\pi^-$, is reduced while the number of signal events is maintained. In the same way, the right-up panel shows sections of the Armenteros-Podolanski plot with a positive value of α for the Λ and a negative value of α for the $\overline{\Lambda}$ hyperons. Here, the larger arc at the top representing the decays $K^0 \rightarrow \pi^+\pi^-$ is visibly reduced in the regions which overlap the Λ and $\overline{\Lambda}$ decays. Thus, the K^0 background events are successfully reduced by the RICH cut. In the left-down panel the invariant mass distribution is shown with a Gaussian fit for the data before applying the RICH cut, while the right-down panel shows the same invariant mass distribution with a Gaussian fit after the RICH cut has been applied to the data. The invariant Λ mass m is shifted by $m - m_{PDG}$ in the fit procedure, where $m_{PDG} = 1.115683$ GeV/c^2 is the value of the Λ mass as published by the Particle Data Group [24]. The invariant mass distributions are plotted in the range from $1.07 - m_{PDG}$ GeV/c^2 to $1.37 - m_{PDG}$ GeV/c^2, divided into 150 bins. The invariant mass distributions are fitted with a Gaussian peak, which describes the signal events, superimposed by a 3rd degree polynomial background parametriza-
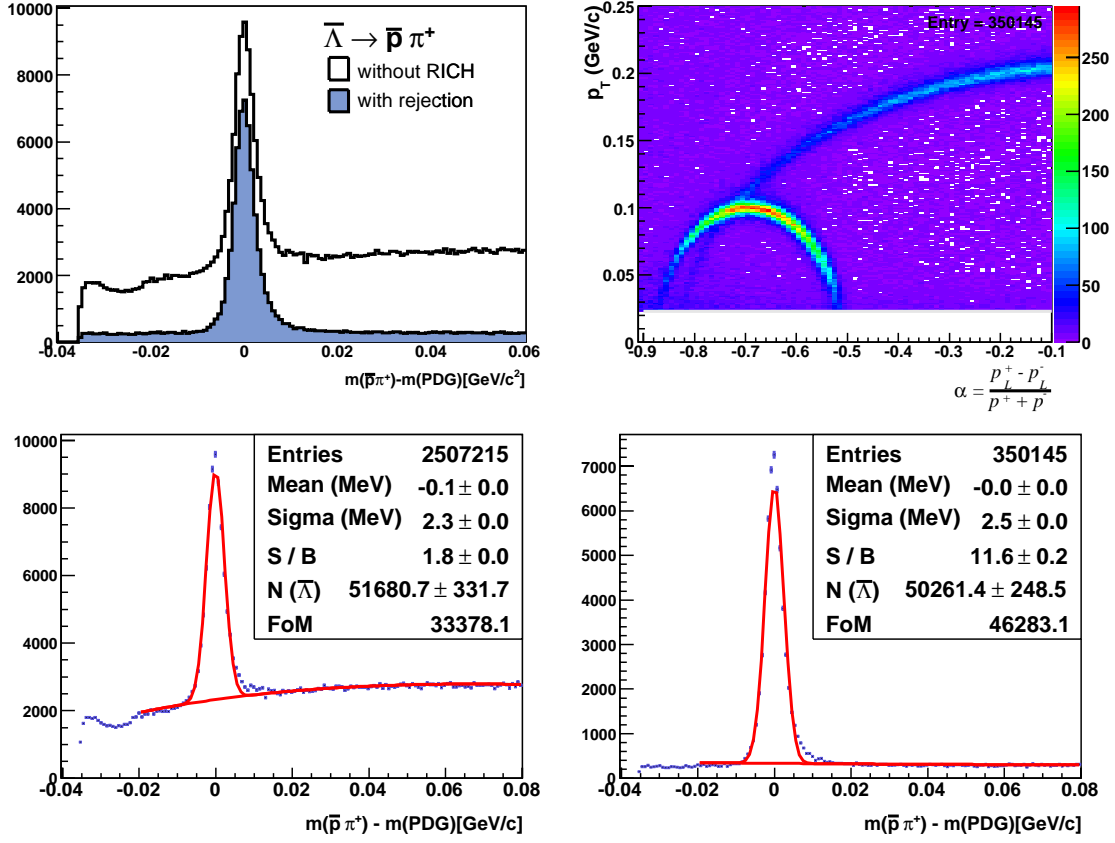
Figure 4.12: Left-up: Invariant mass distribution of $\overline{\Lambda}$ with and without RICH cut. Right-up: Armenteros-Podolanski plot with RICH cut in $\alpha < 0$. Left-down: Result of Gaussian fit for data without RICH cut. Right-down: Result of Gaussian fit for data with RICH cut.

tion in the range from -0.02 to 0.08 GeV/c². Again, it is clearly visible that the background distribution after using RICH information is significantly reduced and distributed perfectly flat, which is important for minimizing the values of the parameters of the polynomial background parametrization and, thus, improving the fit quality and convergence. Equally important, the number of signal events in the Λ and $\overline{\Lambda}$ peaks stays almost constant before and after applying the RICH cut, which means that the RICH cut reduces true background events while maintaining the number of signal events in the data. Furthermore, the error of the number of Λ events, which is estimated from the fit parameter, is also reduced significantly by applying the RICH cut. This fact is important for reducing the statistical error of the Λ polarization, which is extracted from the invariant mass distributions. The mean position of the signal peak lies very close to the invariant mass value, which is given by the Particle Data Group [24], and the signal width of 2.5 MeV/c both for Λ and $\overline{\Lambda}$ indicates that the calibration and alignment of the COMPASS spectrometer worked very well during the data acquisition in 2007.

4.2.6 Final Statistics in the Selection of Λ Hyperons

The full data of the 2007 data acquisition were used to calculate the Λ polarization. The data which were included in this analysis were checked for data quality and several cuts, which were explained in the previous sections, were applied. In Table 4.2, the number of events are given, which survived the respective kinematic cut, the RICH rejection, and the number of signal events, which are located within the signal peak of the Gaussian fit in the Λ and $\overline{\Lambda}$ invariant mass distributions.

Table 4.2: Summary of the events used in the calculation of Λ polarization: The table lists how the different cuts reduce the absolute and relative number of events. N_P and N_S denote the number of primary and secondary vertices after application of the cut, respectively. N_Λ states the number of events identified as Λ hyperons.

Cut	Number of Events	
	N_P	Rel.ratio
Best primary vertex after badspill selection	139226958	1.000
Definition of scattered μ' with μ' recovery	137900016	0.990
μ' does not cross SM2 yoke	133790909	0.961
μ' traverses $X/X_0 > 30$ cm	126976218	0.912
Target cuts: V_{prim} in target cells; μ crosses all cells	103177878	0.741
$Q^2 > 1.0$ (GeV/c)^2	102897838	0.739
$0.1 < y < 0.9$	60460742	0.434
	N_S	Rel.ratio
Decay track : $X/X_0 < 10$ cm	238182905	1.000
Removal of fringe field tracks : $z_{last} > 350$ cm	212007531	0.890
Momentum of both daughter particles : $p^\pm > 1$ GeV/c	195225470	0.820
Both tracks are not associated to any primary vertex	21701920	0.091
Require exactly one positive & one negative track	21699263	0.091
Both tracks do not cross SM2 yoke	21685389	0.091
Angle of collinearity : $\theta_{col} < 10$ mrad	3650732	0.015
Transverse momentum of decay particle : $p_T > 23$ MeV/c	2591169	0.011
Decay length D larger than 7.5 times σ_D : D $/\sigma_D > 7.5$	2507215	0.011
	N_S	Rel.ratio
Using RICH cut for Λ	640923	0.003
Using RICH cut for $\overline{\Lambda}$	350145	0.001
	N_Λ	
Gaussian fit in the invariant mass of Λ	104637	
Gaussian fit in the invariant mass of $\overline{\Lambda}$	50261	

4.2.7　Kinematic Distributions for Λ and $\overline{\Lambda}$

The events which survived the kinematic cuts and the RICH rejection are assumed to result mainly from Λ and $\overline{\Lambda}$ hyperons. The background distribution in the Λ invariant mass distribution is fitted by a 3rd degree polynomial; consecutively the assumed background events in the mass window of the Λ signal peak which lie underneath the Λ signal peak and in an area described by an extrapolation of the 3rd degree polynomial between the left-hand side and the right-hand side of the Λ signal peak are subtracted from the assumed true Λ hyperons in the Λ signal peak.

The typical kinematic distributions of the events after passing all selection cuts, which lie within the invariant mass window of the Λ and $\overline{\Lambda}$ mass after subtracting the events from underneath the 3rd degree polynomial, are shown in Fig. 4.13 for the Λ hyperons and in Fig. 4.14 for the $\overline{\Lambda}$ hyperons. The distributions correspond to the kinematically descriptive parameters Q^2 (squared momentum transfer), x_{Bj} (Bjorken scaling variable), y (energy fraction of the projectile transferred from the incoming lepton to the nucleon), W (mass of the hadronic final state), x_F (Feynman scaling variable) and z (fraction of the virtual photon energy carried by a hadron) of the final Λ and $\overline{\Lambda}$ samples. Predominantly true Λ and $\overline{\Lambda}$ events are anticipated in those kinematic distributions. If the kinematic distributions of the events in the Λ mass window are not polluted by unexpected resonances or otherwise differing characteristics of the remaining background events, the kinematic distributions display the behaviour of the Λ and $\overline{\Lambda}$ hyperons. The mean values which are quoted in each of the distributions are approximately the same for Λ and $\overline{\Lambda}$. The x_F distribution peaks at 0.18 for the Λ and 0.17 for the $\overline{\Lambda}$, which corresponds to the fact that most of the events in the sample belong to the current fragmentation region. The invariant mass of the hadronic state W is larger than 4 GeV/c^2 for both Λ and $\overline{\Lambda}$, which indicates that the Λ and $\overline{\Lambda}$ originate from quark interaction and not from hadronic resonances.
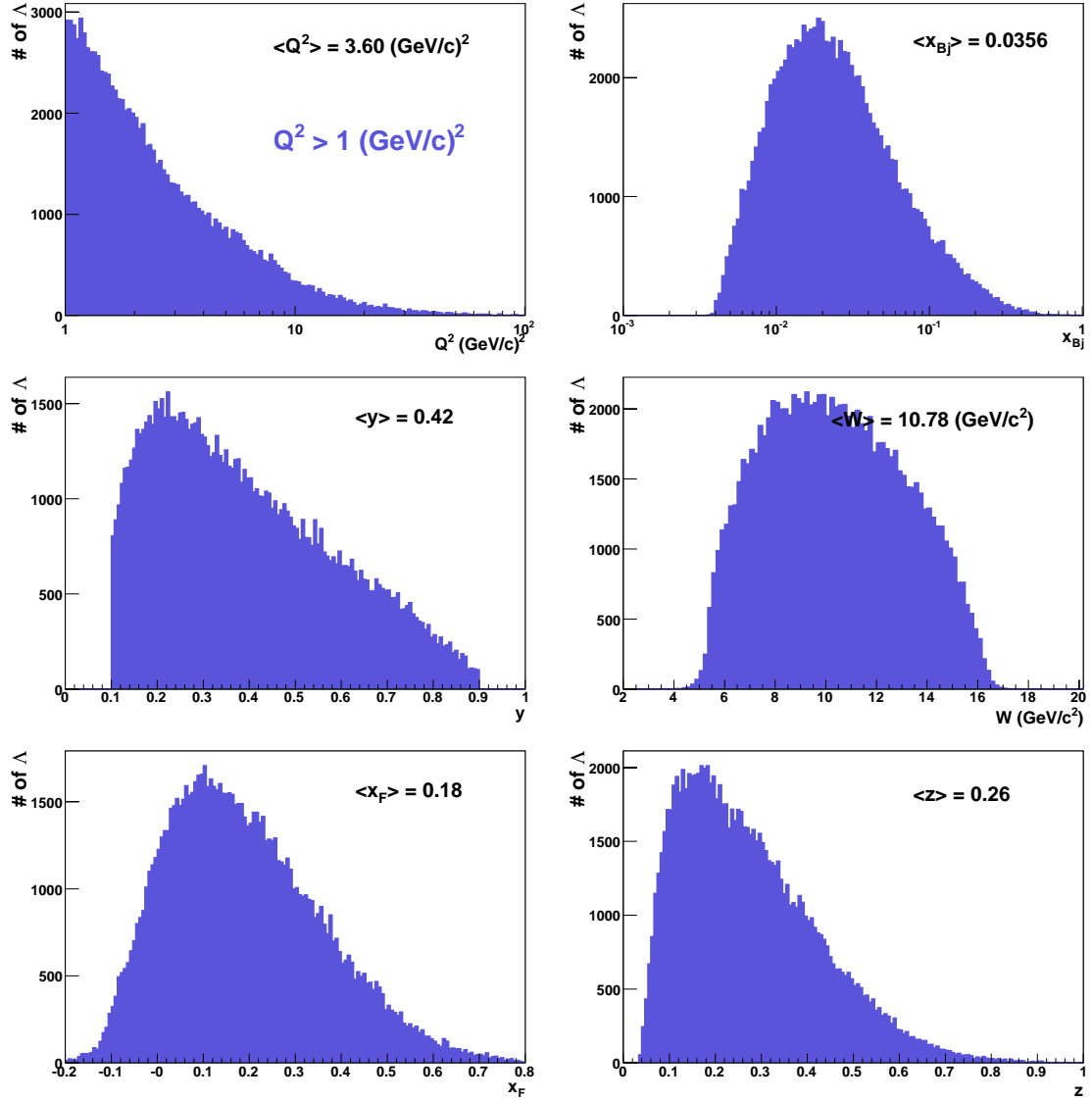
Figure 4.13: Q^2 (squared momentum transfer), x_{Bj} (Bjorken scaling variable), y (energy fraction of the projectile transferred from the incoming lepton to the nucleon), W (mass of the hadronic final state), x_F (Feynman scaling variable) and z (fraction of the virtual photon energy carried by a hadron) distribution of Λ hyperons with application of RICH cut. The mean values are shown in each plot.
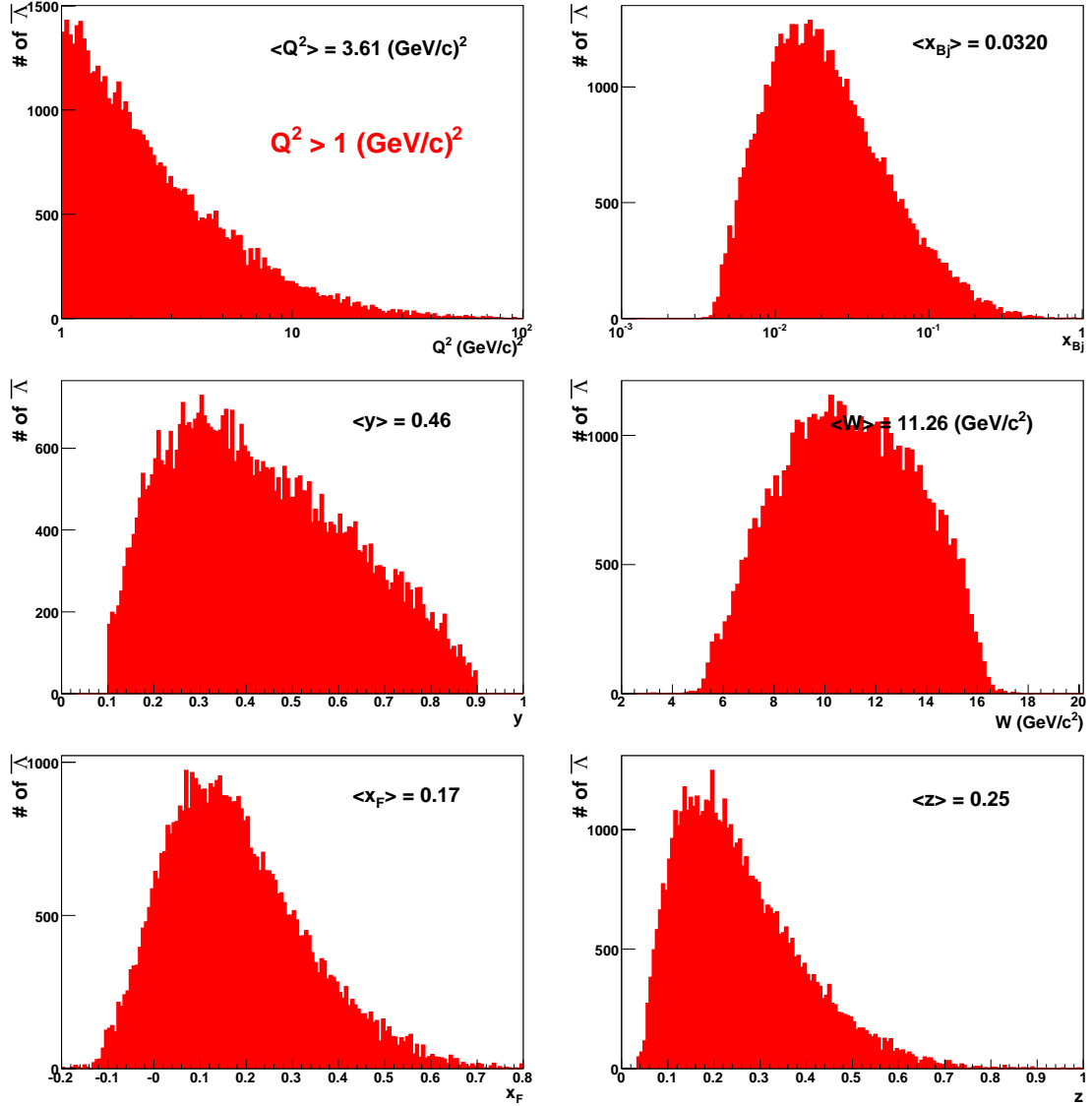
Figure 4.14: Q^2 (squared momentum transfer), x_{Bj} (Bjorken scaling variable), y (energy fraction of the projectile transferred from the incoming lepton to the nucleon), W (mass of the hadronic final state), x_F (Feynman scaling variable) and z (fraction of the virtual photon energy carried by a hadron) distributions of $\overline{\Lambda}$ hyperons with application of RICH cut. The mean values are shown in each plot.

Chapter 5

Results

In the previous chapter the selection criteria for signal events were explained; furthermore, kinematic properties and invariant mass distributions of the final Λ and $\overline{\Lambda}$ data were demonstrated. The technique to extract the Λ hyperon polarization was described in Section 2.7. In this chapter, the results of the Λ and $\overline{\Lambda}$ polarization are presented as well as an estimate of the systematic errors.

5.1   Results of Transverse Λ and $\overline{\Lambda}$ Polarization
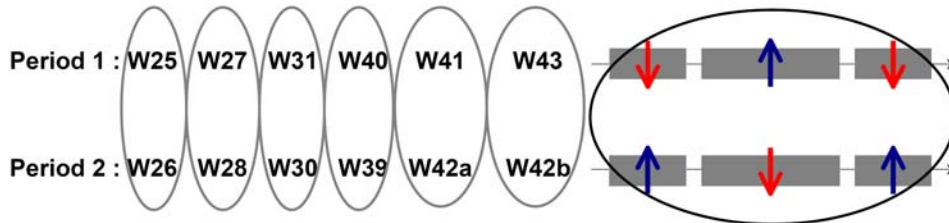
Figure 5.1: Standard target configuration during data taking periods used in the calculation of Λ polarization. The red arrows display the target spin orientation downwards, while the blue arrows state the target spin orientation to be upwards [66].

The Λ and $\overline{\Lambda}$ polarizations were extracted using a target configuration of six target cell spin orientations. In Fig. 5.1 the standard target spin orientations are shown. Here, the top line refers to a target cell spin orientation of $-+-$ $=\downarrow\uparrow\downarrow$ for the up-, center-, and down-stream target cell, respectively, for the quoted data taking periods W25, W27, W31, W40, W41 and W43. The remaining 2007 data taking periods W26, W28, W30, W39, W42a and W42b correspond to the reverse target cell spin orientation $+-+$ $=\uparrow\downarrow\uparrow$ as shown in the bottom line of Fig. 5.1. Due to the fact that eleven data taking periods were recorded, period W42 had to be splitted

into two subperiods W42a and W42b with comparable statistics to be able to form six pairs of opposite target spin orientation periods.

The Λ and $\overline{\Lambda}$ polarization P_Λ is studied by dividing the sample into five subsamples of x_{Bj} bins and independently five subsamples of z bins. The x_{Bj} and z bins were chosen in a way to represent roughly the same statistics in each bin; these x_{Bj} and z bins of similar statistics are shown in Fig. 5.2 for the Λ and $\overline{\Lambda}$ hyperon, respectively.
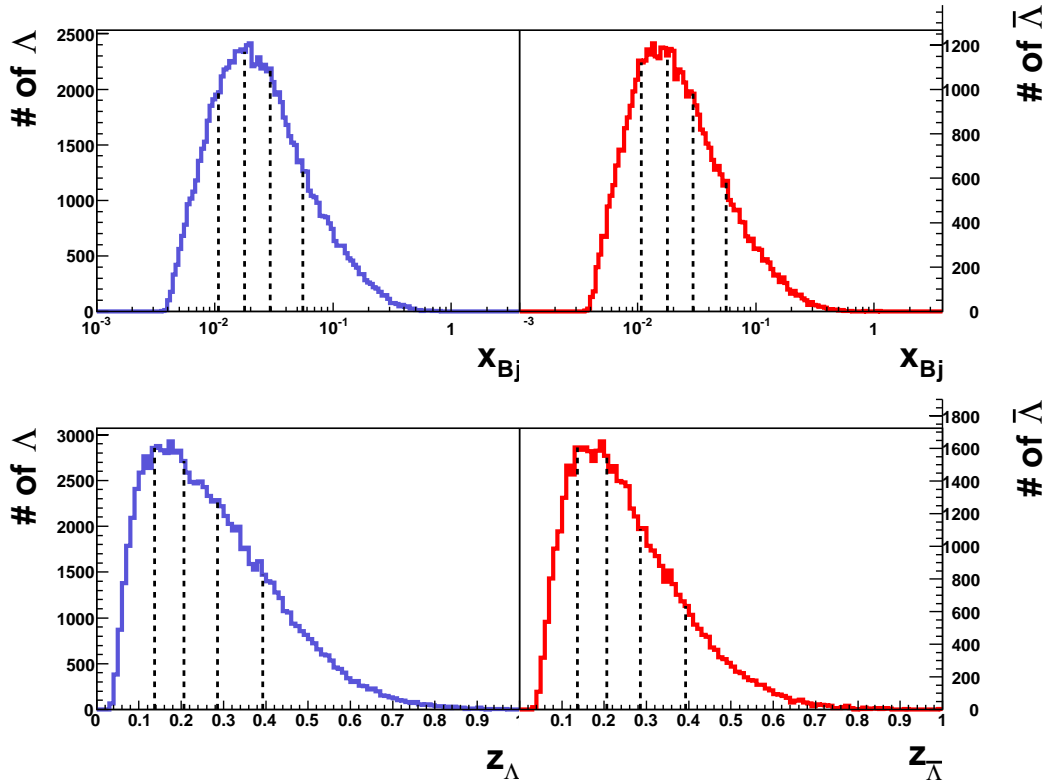
Figure 5.2: Distributions of x_{Bj} and z of the Λ and $\overline{\Lambda}$ hyperon, respectively. The 5 bins of similar statistics used in this analysis are indicated by dashed lines.

The x_{Bj} and z dependence of P_Λ is investigated, where P_Λ is calculated for each pair of opposite target spin orientation periods, e.g. P_Λ is extracted for data taking period pairs W25 & W26, W27 & W28, W31 & W30, W40 & W39, W41 & W42a (which means, run number ≤ 63609), and W43 & W42b (which means, run number ≥ 63610). The six pairs of data taking periods, for which six values of P_Λ are calculated individually, are shown on the left of Fig. 5.1. The polarizations P_Λ for the individual data taking period pairs in dependence of x_{Bj} and z are for completeness shown in Fig. 5.3. The polarizations which are extracted from the individual data taking period pairs all lie in a very similar range, which is expected as deviations could be described by a change of the experimental setup only.
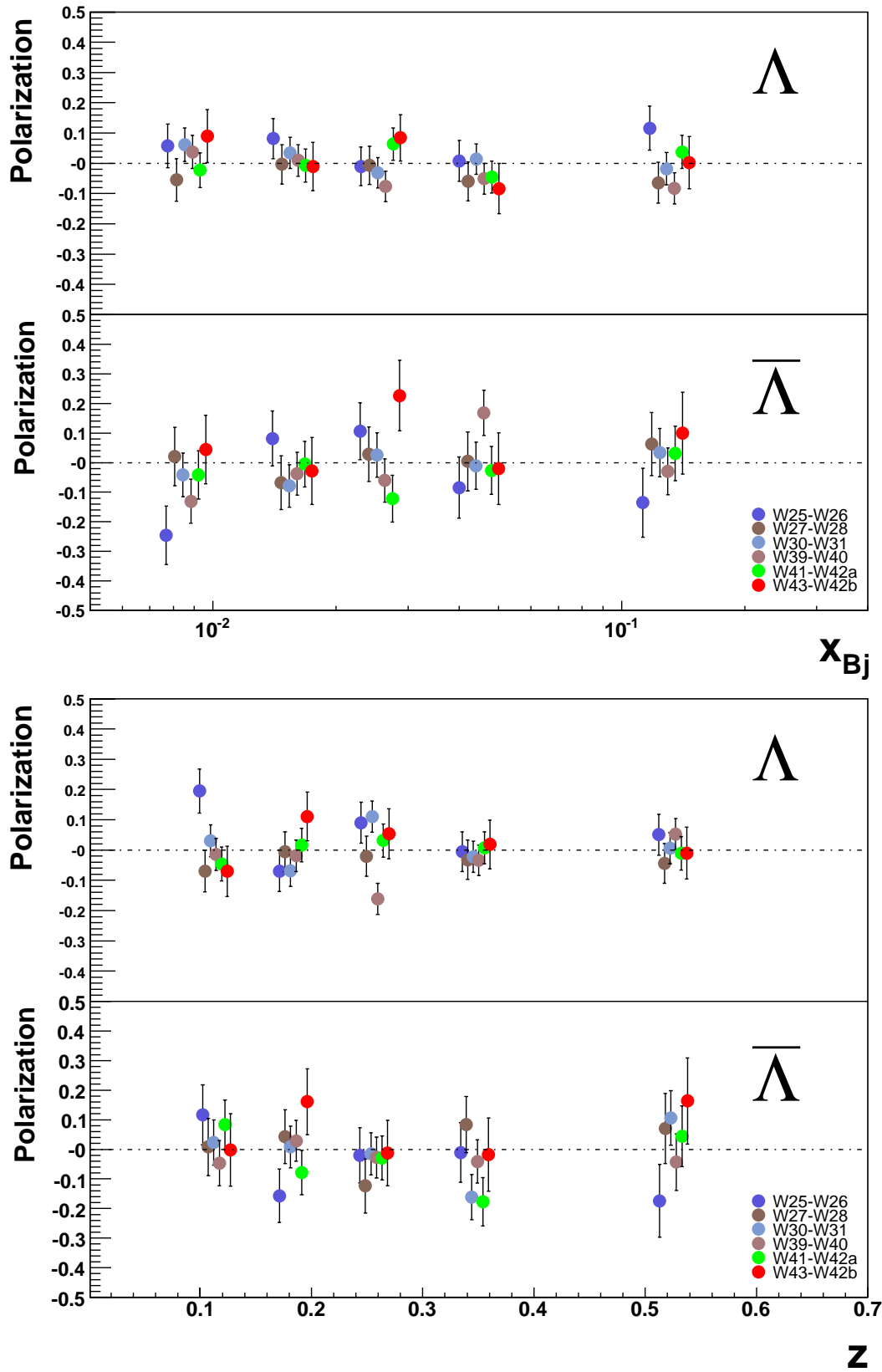
Figure 5.3: Dependence on x_{Bj} and z of the Λ and $\overline{\Lambda}$ polarization extracted from the six individual data taking period pairs.

The weighted mean of P_Λ of those six data taking period pairs was calculated for each x_{Bj} and z bin, as shown in Fig. 5.4. The results are compared for signal events which passed all selection cuts without applying the RICH veto condition versus signal events which passed all selection cuts including the RICH veto condition. The P_Λ distributions in Fig. 5.4 show no significant deviation from zero in the complete investigated range of x_{Bj} and z. Moreover, the values of P_Λ do not show any tendency in regions of high x_{Bj} and z values. The error bars in the plots take into account the statistical errors only, since the systematic errors are estimated to be smaller than the statistical errors as will be shown in Subsection 5.2.4.
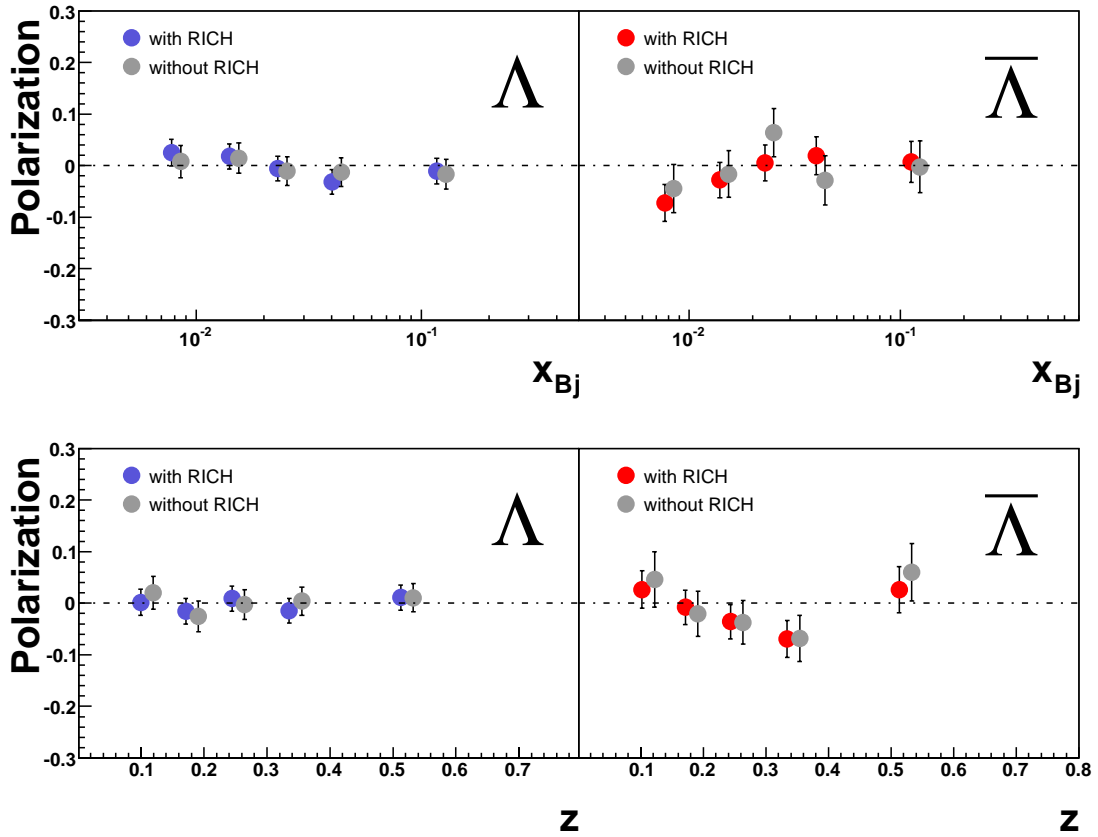
Figure 5.4: Dependence of the Λ and $\overline{\Lambda}$ polarization on x_{Bj} and z with RICH cut and without RICH cut.

5.2   Estimation of Systematic Errors

This section will investigate the influence of biases of the presented analysis method on the results of the Λ and $\overline{\Lambda}$ polarization. Possible systematic errors are estimated using the so-called pulls distributions. The abundant background of spinless kaons provide a good opportunity to investigate biases of the analysis method, since their decay signature is topologically the same as for the Λ and $\overline{\Lambda}$ hyperons, but with an expected polarization of rigorously zero. The fitting procedure of the Λ and $\overline{\Lambda}$ invariant mass also might introduce systematic errors due to the nontrivial fit procedure in every $\cos\theta_T$ bin. The systematic effect of the target cell spin orientation is investigated in up-down and right-left asymmetries of the target setup to control the efficiency of the apparatus acceptance correction. The effect of the target spin orientation is essential to this analysis as the Λ polarization could be severely affected by the target spin orientation.

5.2.1   Compatibility of Subperiods

A unique and accurate way to investigate the compatibility of the final Λ and $\overline{\Lambda}$ polarization for each x_{Bj} and each z bin in each of the target cell spin configurations is obtained by building the pulls distributions [101]. For this purpose, the polarizations P_Λ and their errors are extracted separately in each bin of x_{Bj} and z and for each subperiod pair. Consecutively, each one of those polarizations P_Λ and its error from one subperiod pair in one bin of x_{Bj} or z is compared with the mean $\langle P_\Lambda \rangle$ of all subperiods and its error in the respective x_{Bj} or z bin. This procedure is repeated for each x_{Bj} and z bin individually. In the same way the compatibility of the $\overline{\Lambda}$ polarizations of each subperiod pair in each x_{Bj} and z bin and the corresponding errors are compared to the mean $\langle P_{\overline{\Lambda}} \rangle$ of all subperiods and its error. The pulls distribution is defined as

$$Pull \quad = \quad \frac{\left(P_i - \langle P_{\Lambda/\overline{\Lambda}} \rangle \right)}{\sqrt{\sigma^2_{P_i} - \sigma^2_{\langle P_{\Lambda/\overline{\Lambda}} \rangle}}}, \quad \text{where } i = 1, 2, ..., 120 \tag{5.1}$$

$$\tag{5.2}$$

where P_i are the 120 extracted polarizations, $\sqrt{\sigma^2_{P_i}}$ are the corresponding errors and i is the configuration of the specific P_i ($i = 2 \times 2 \times 5 \times 6$: for 2 particles Λ and $\overline{\Lambda}$, each in 2 kinematics x_{Bj} and z, with 5 bins each, in 6 target cell spin configurations W25 & W26, W27 & W28, W31 & W30, W40 & W39, W41 & W42a, W43 & W42b). $\langle P_{\Lambda/\overline{\Lambda}} \rangle$ is the respective weighted mean for the Λ or $\overline{\Lambda}$ polarizations separately, containing all subperiods in the specific x_{Bj} and z bins, with the corresponding errors $\sqrt{\sigma^2_{\langle P_{\Lambda/\overline{\Lambda}} \rangle}}$. The pulls distribution in Fig. 5.5 is fitted with a Gaussian, which provides a mean value of -0.1253 $\pm$ 0.0984, thus, being approximately compatible with zero within its error, and a width σ of the Gaussian

fit of one. This behaviour of the pulls distribution is expected and shows that the spread of the data is compatible with statistical fluctuations as well as in good agreement with the measured mean polarizations $\langle P_{\Lambda/\overline{\Lambda}} \rangle$.

Pulls	
Entries	120
Mean	-0.03787
RMS	1.127
χ^2 / ndf	7.434 / 12
Constant	18.86 ± 2.27
Mean	-0.1253 ± 0.0984
Sigma	1.034 ± 0.079
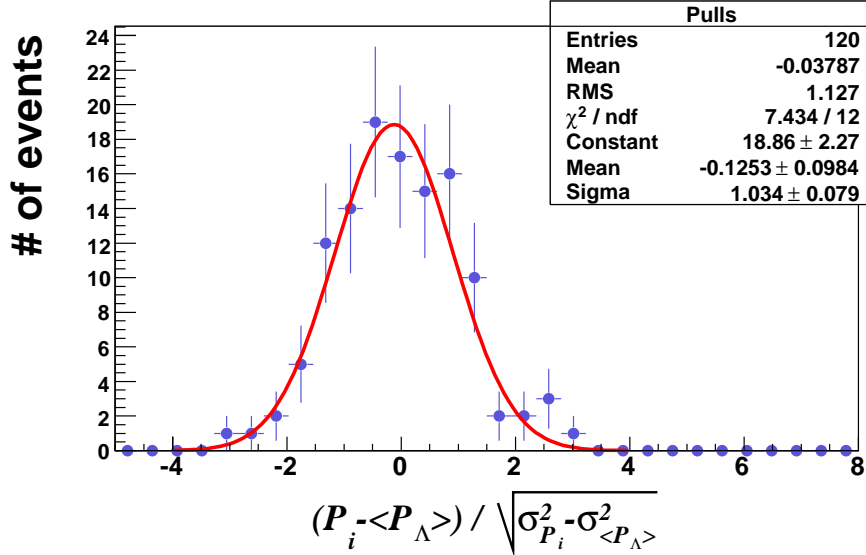
Figure 5.5: Compatibility of the Λ and $\overline{\Lambda}$ results from different periods: Pulls distribution in the x_{Bj} and z bins for the target cell spin configurations as demonstrated in Fig. 5.1, superimposed with a Gaussian fit.

5.2.2   Systematic of K^0 Background

The K^0 events feature a similar decay topology as the Λ and $\overline{\Lambda}$ events and, therefore, contribute to the background of the Λ and $\overline{\Lambda}$ invariant mass peaks. The K^0 are produced in abundance and are spinless. Thus, the K^0 events provide a good opportunity to verify that the analysis is free of obvious biases, since the polarization of the K^0 when extracted in the same way as the Λ polarization is expected to be zero. The K^0 polarization is calculated using the $\cos\theta_T$ angle of the positive decay pion. Since the rejection of background by the RICH has been implemented to veto pions, the RICH cut has to be slightly modified to leave the kaon events untouched in the control data sample. The kaon polarization is shown in Fig. 5.6 where the scale is reduced by a factor of six compared to the Λ and $\overline{\Lambda}$ polarizations in Fig. 5.4 . It can be seen that the overall K^0 polarization (comprising the numerous K^0 sample with a small Λ and $\overline{\Lambda}$ ''contamination'' before the RICH cut) and the kaon polarization of the decay $K^0 \to \pi^+\pi^-$ after applying a RICH likelihood cut on pion identification for both decay particles are both below 1 % and apparently close to zero. The K^0 polarization being perfectly compatible with zero gives confidence that the analysis is non-biased, the acceptance correction is working efficiently and possible apparatus effects are small.
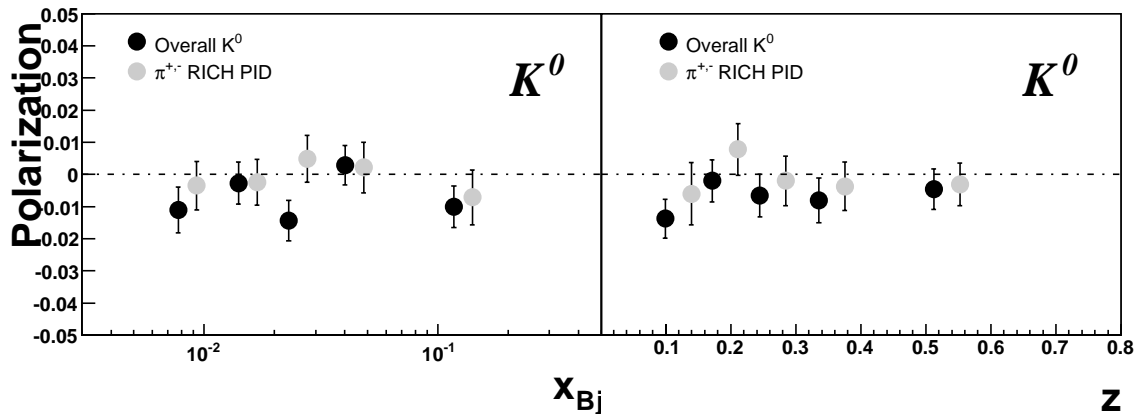
Figure 5.6: Results of K^0 polarization.

5.2.3 Systematic Effects due to Methods
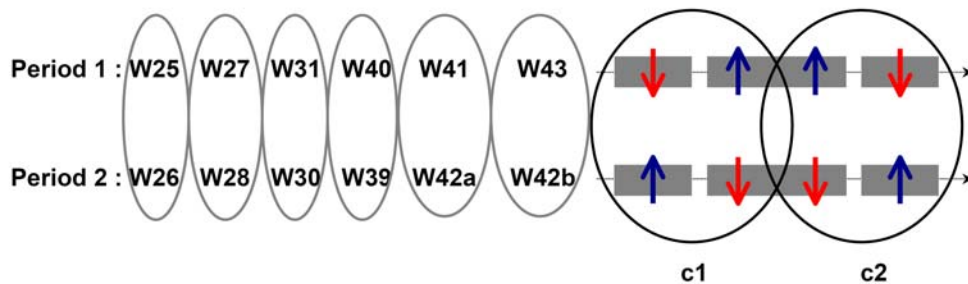
Figure 5.7: Definition of the split six target-periods configuration used to estimate systematic effects. The red arrows display the target spin orientation downwards, while the blue arrows state the target spin orientation to be upwards [66].

Several extensive tests have been performed to investigate systematic effects due to different methods of extracting the Λ polarization. First, a finer grid of target cell spin orientations has been considered to estimate possible systematic shifts of the calculated Λ polarization. Each data taking period is divided into two subperiods c_1 and c_2 with splitting the target as shown in Fig. 5.7. The Λ polarization is extracted for each of the two subperiods and consecutively the weighted mean of the two subperiods c_1 and c_2 is calculated. The weighted mean of the two subperiods is expected to result in the same polarization as the polarization calculated in the standard three target-period configuration shown in Fig. 5.1. In Fig. 5.8 the Λ and $\overline{\Lambda}$ polarizations are compared for both target-period configurations in bins of x_{Bj} and z, respectively. It is clearly visible that the results for both target-period configurations are identical.
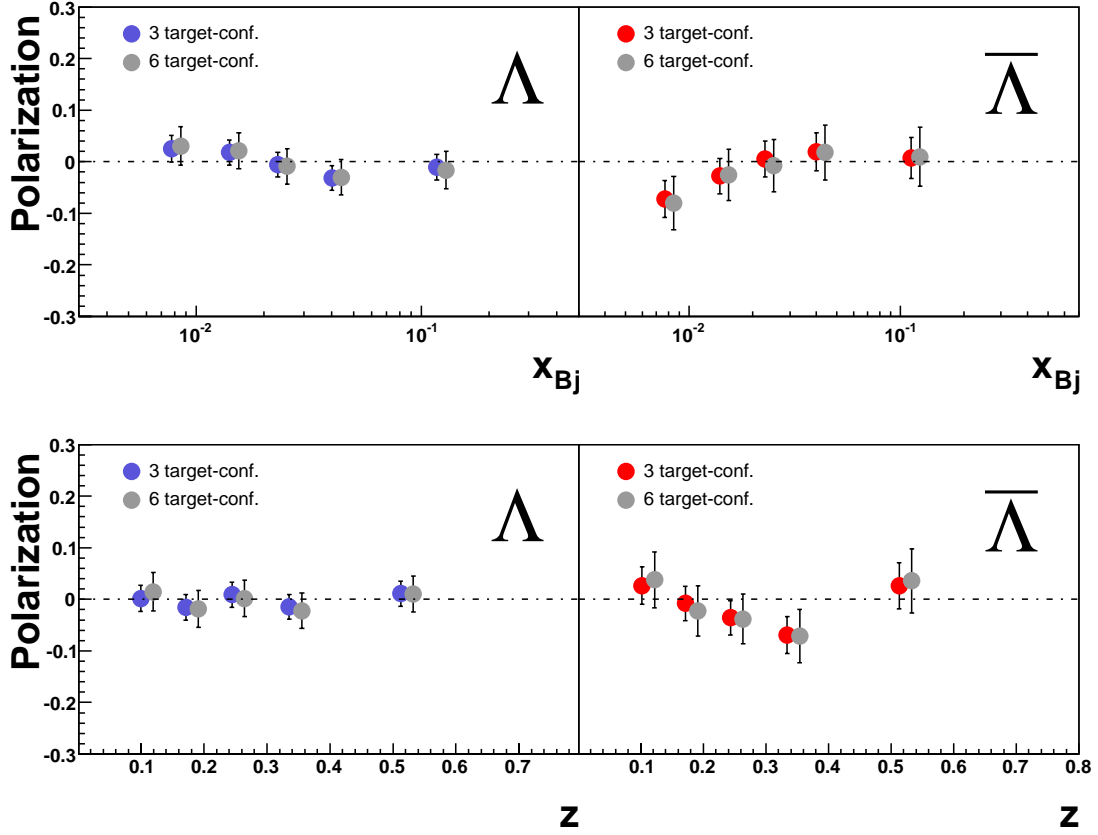
Figure 5.8: The Λ and $\overline{\Lambda}$ polarizations obtained from the six target-periods configuration are compared with the Λ and $\overline{\Lambda}$ polarizations from the three target-periods configuration.

Since the statistics of available Λ and $\overline{\Lambda}$ hyperons is quite limited, it is not possible to use a finer $\cos\theta_T$ binning to extract the polarizations as the fitting errors increase massively with smaller statistics. Instead, the simplified formula of Eq. 2.70 is used to calculate the polarization in two $\cos\theta_T$ bins. Nevertheless, the polarization is calculated in four $\cos\theta_T$ bins to study the influence of the number of $\cos\theta_T$ bins. To perform the analysis in four $\cos\theta_T$ bins, the $\epsilon - (\cos\theta_T)$ distribution has to be calculated. The slope of a linear fit determines the corresponding Λ and $\overline{\Lambda}$ polarizations. In Fig. 5.9 the extracted Λ and $\overline{\Lambda}$ polarizations in bins of x_{Bj} and z obtained in two $\cos\theta_T$ bins are compared with the respective polarizations obtained in four $\cos\theta_T$ bins. It can be seen that the four $\cos\theta_T$ method has no significant systematic influence on the result of the Λ polarization. Due to the fact that the number of produced $\overline{\Lambda}$ is even smaller than the number of produced Λ hyperons, it seems logical that the distributions of the $\overline{\Lambda}$ polarization in bins of x_{Bj} and z look more scattered than the Λ polarization distributions because of the more erroneous fitting procedure of the low statistics $\overline{\Lambda}$ invariant mass spectra.
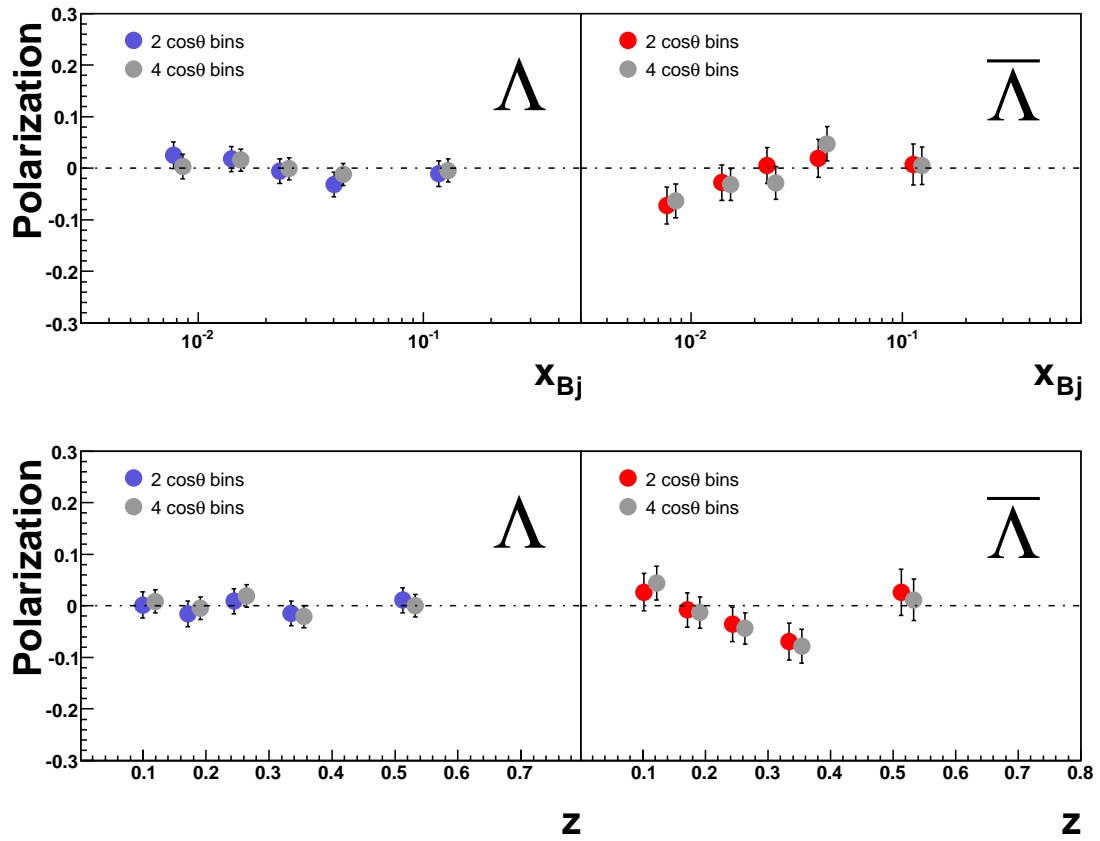
Figure 5.9: The Λ and $\overline{\Lambda}$ polarizations obtained in two $\cos\theta_T$ bins are compared with the Λ and $\overline{\Lambda}$ polarizations obtained in four $\cos\theta_T$ bins.

5.2.4   Influence of Target Setup on Polarization

The systematic effect of the target setup towards false polarizations is tested in three different methods. The first effect to be investigated is the rotation of the target spin direction around the z-axis by an angle generated randomly on an event-by-event basis between $-\pi$ and $+\pi$, as is denoted **Random** in Fig. 5.10, compared to a rotation of the target spin direction around the z-axis by a fixed 90 degree angle, which is denoted **Sideway** in Fig. 5.10. Both directions **Random** and **Sideway** are depicted in the laboratory system. The Λ and $\overline{\Lambda}$ polarizations are extracted in the same way as if the target spin orientation was not artificially altered. The effect of both ways to manipulate the target spin orientation is a polarization which is rigorously zero, which is shown in the top two panels of Fig. 5.11.
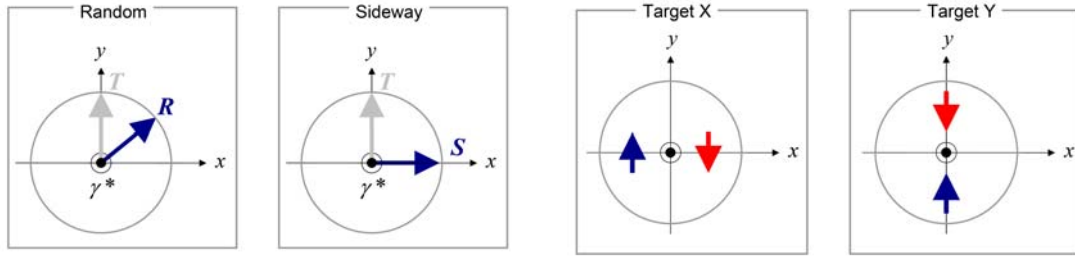
Figure 5.10: From left to right: Definitions of target spin orientation are shown by an event-by-event random rotation **Random** and a sideway direction **Sideway** of the target spin in the laboratory system, as well as defined in a geometrical way in the x-direction **Target X** and y-direction **Target Y** [66].

The second effect which is considered manipulates the target geometry into quadrants of the x-y plane. The Λ polarization is calculated under the assumption that the data of all target cells are divided to belong to either the up- or the down-cell of the target depending on the location of the event's primary vertex. The absolute zero of the COMPASS x-y-coordinate system is defined to be along the beam axis, which corresponds to the z-axis. If the primary vertex of an event has a negative x-coordinate, this event is defined to be in the target cell with target spin orientation pointing upwards, denoted **Target X** in Fig. 5.10. If on the other hand the primary vertex of an event has a positive x-coordinate, the primary vertex is assumed to lie in the target cell with target spin orientation downwards. In a similar manner, the data sample of all target cells are divided to belong to either the up- or the down-cell of the target, denoted **Target Y** in Fig. 5.10. If the primary vertex of an event has a positive value of its y-coordinate, it is defined to be in the down-cell of the target - a negative y-coordinate places the event in the up-cell of the target. Also, the polarizations extracted from these manipulated data are expected to be rigorously zero, which is demonstrated in the bottom two panels of Fig. 5.11.
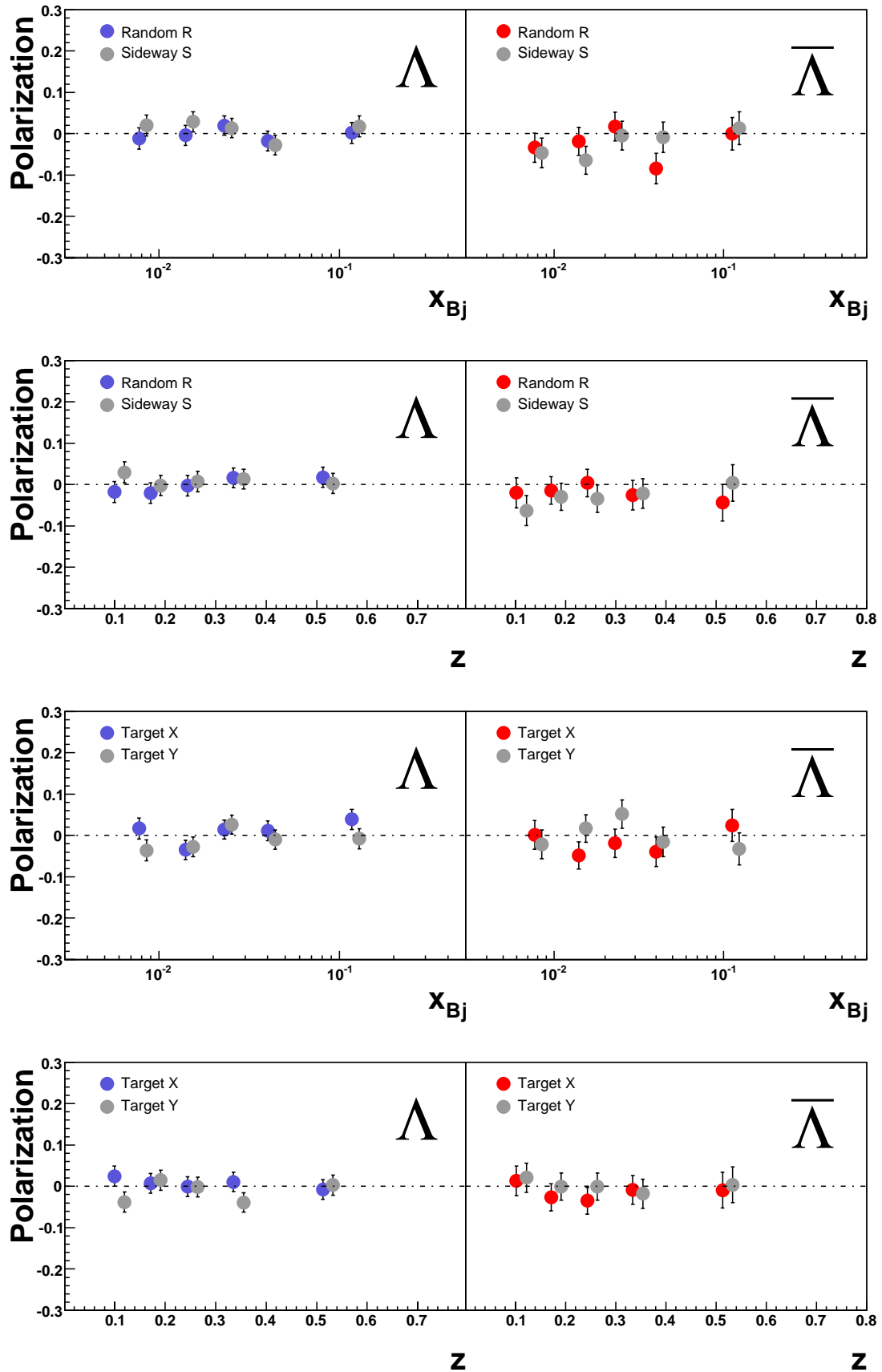
Figure 5.11: In the top two panels, the results of polarization with random and sideway target spin orientation are given. The bottom two panels show the results of polarization with dividing the target in x- and y-direction.

The third effect which is considered selects the events by splitting the middle target cell in two halves of equal length. Two different combinations of opposite target spin orientations are assigned to the two halves of the middle target cell, which is demonstrated in Fig. 5.12. The two different possibilities of false target spin orientations assign wrong signs of target spin orientations to the up- and downstream target cell, as the standard target spin polarization is either ↑↓↑ or ↓↑↓ for the upstream, middle, downstream target cell. The false target configurations, as shown in Fig. 5.12, are expected to result in a zero polarization. The extracted polarizations from this false configuration are shown in Fig. 5.13 and are perfectly compatible with zero.
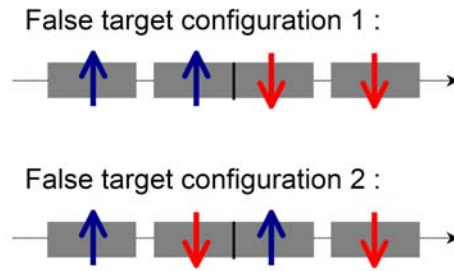
Figure 5.12: False target configurations with splitting the middle target cell [66].

Since the various investigations of systematic effects due to the detector setup show no indication for a systematic shift in the Λ and $\overline{\Lambda}$ polarizations, it is concluded that the systematic errors due to acceptance fluctuations are smaller than the statistical errors. A pulls distribution of all fake polarizations in the x_{Bj} and z bins for the Λ and $\overline{\Lambda}$ hyperons is created to estimate the compatibility of the extracted false polarizations with zero and, thus, to estimate the systematic errors. Calculating the pulls distributions for the purpose to evaluate false polarizations is usually deployed if the result $P_{expected}$ has an anticipated value of zero for a set of measurements $\{P_i, \sigma_i\}$, thus, a Gaussian fit of the pulls distribution is expected to be centered at zero with a width of one. The pulls distribution for this purpose [101] is defined as

$$Pull = \frac{P_{measured} - P_{expected}}{\sqrt{\sigma_{P,measured}^2}}, \tag{5.3}$$

where the expected polarization $P_{expected}$ from the target setup towards false polarizations is rigorously zero. The pulls distributions for the Λ and the $\overline{\Lambda}$ hyperon, which are shown in Fig. 5.14, have 360 entries each. Each of the effects of the false configurations discussed above, Random **R**, Sideway **S**, Target **X**, Target **Y**, False Target Conf. 1 and False Target Conf. 2, contributes 10 polarizations $P_{measured}$ for the x_{Bj} and z bins, for each of the six data taking target-periods: $6 \times 10 \times 6$. The mean values of the Gaussian fits of the pulls distributions for the Λ and $\overline{\Lambda}$ hyperon are 0.0107 ± 0.0631 and -0.1145 ± 0.0504, respectively. Thus, there exists
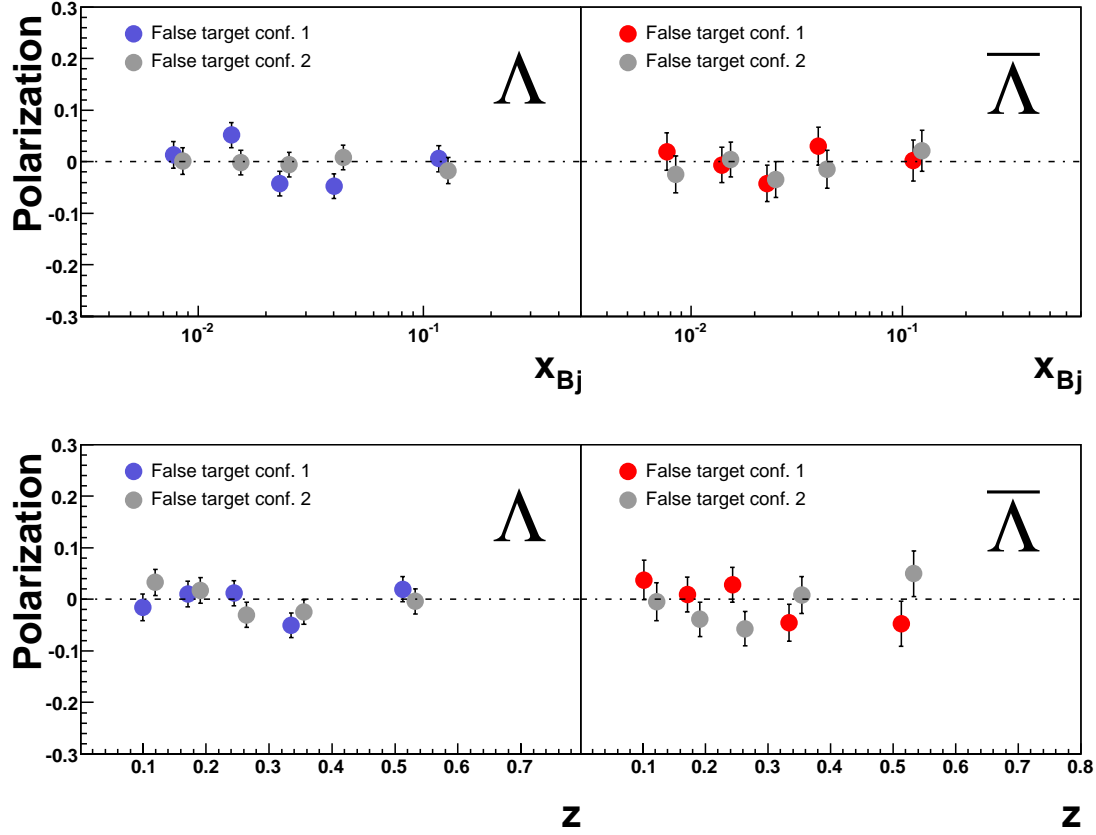
Figure 5.13: Results of polarization with false target configurations.

a small deviation of the mean of the $\overline{\Lambda}$ pulls distributions from the expected mean value of one. The width from the Gaussian fits is compatible with one for the Λ pulls distribution and lies within two standard deviations for the $\overline{\Lambda}$ pulls distribution.

The pulls distribution allows to estimate an upper limit on the systematic error, which is for the unfolded pulls distribution $\sigma_{stat} = 1$. A deviation of the width from 1 is due to a systematic error σ_{sys} [102]. The upper limit of systematic errors is estimated by calculating the deviation from σ and their error with two standard deviations in the unit of the statistical error,

$$
\begin{aligned}
\sigma_{sys} \quad &\leq \quad \sqrt{((\sigma_{Pulls} + 2 \cdot \delta\sigma_{Pulls})^2 - 1) \cdot \sigma_{stat}^2} \qquad\qquad (5.4) \\
&\leq \quad \sqrt{((0.9958 + 2 \times 0.0491)^2 - 1) \cdot \sigma_{stat}^2} = 0.44 \cdot \sigma_{stat} \quad \text{for } \Lambda \qquad (5.5) \\
& \quad \sqrt{((0.9377 + 2 \times 0.0395)^2 - 1) \cdot \sigma_{stat}^2} = 0.18 \cdot \sigma_{stat} \quad \text{for } \overline{\Lambda}, \qquad (5.6)
\end{aligned}
$$

where σ_{Pulls} is the value of **Sigma** and $\delta\sigma_{Pulls}$ is its error in the pulls distributions, which can be found in the bottom line of the statistics box of Fig. 5.14.
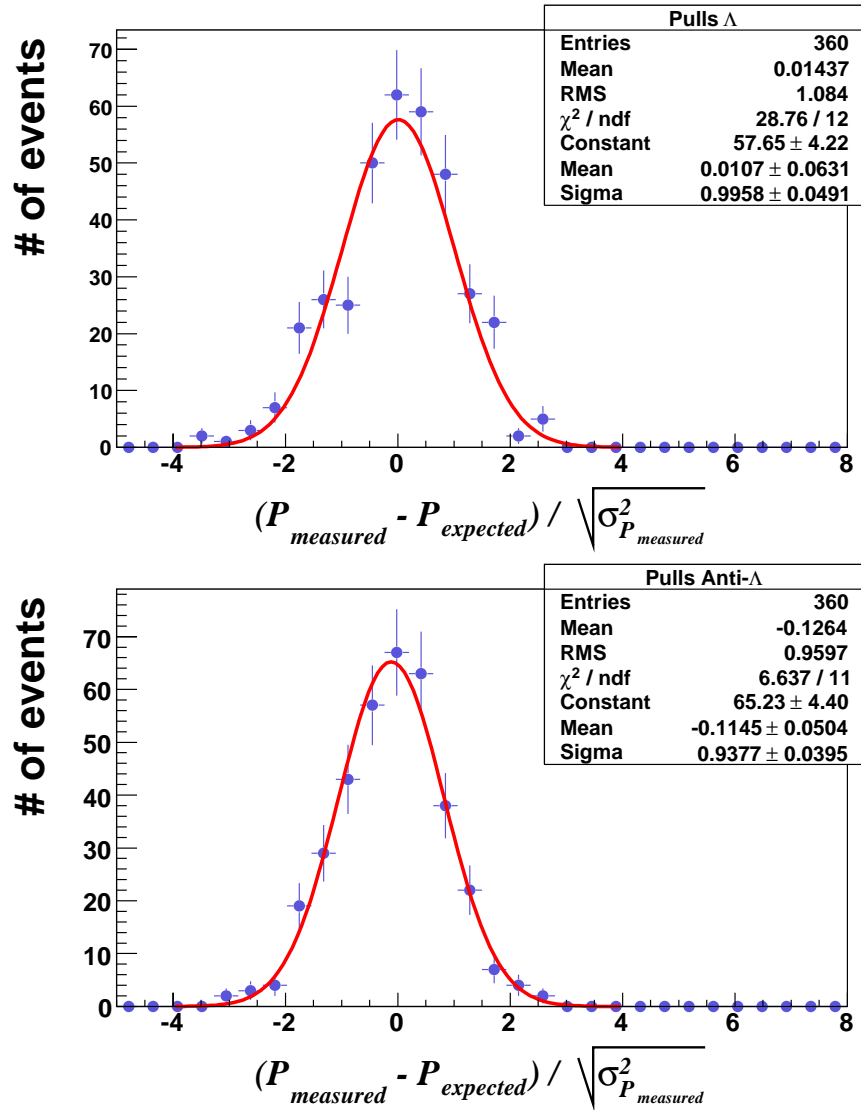
Figure 5.14: Pulls distribution of all false polarizations with a Gaussian fit for Λ (upper panel) and $\overline{\Lambda}$ (lower panel) separately.

The observed systematic error is 44 % of the statistical error for the Λ and below 20 % for the $\overline{\Lambda}$ hyperon. The behaviour that the systematic error of the Λ consists of a higher percentage of the corresponding statistical error than the respective error of the $\overline{\Lambda}$ can be explained by the fact that the statistical errors of each bin of the $\overline{\Lambda}$ polarization are roughly twice as large as the statistical errors of the Λ polarizations in the x_{Bj} and z bins. Thus, the systematic errors both for the Λ and $\overline{\Lambda}$ polarizations are approximately the same in absolute numbers as is anticipated. The systematic error estimated from false polarization is in general smaller than the statistical error. The Λ and $\overline{\Lambda}$ polarizations and their statistical errors as a function of x_{Bj} and z are shown in Fig. 5.15 in comparison with the estimated systematic errors drawn at the bottom of the graphs as grey errorbands.
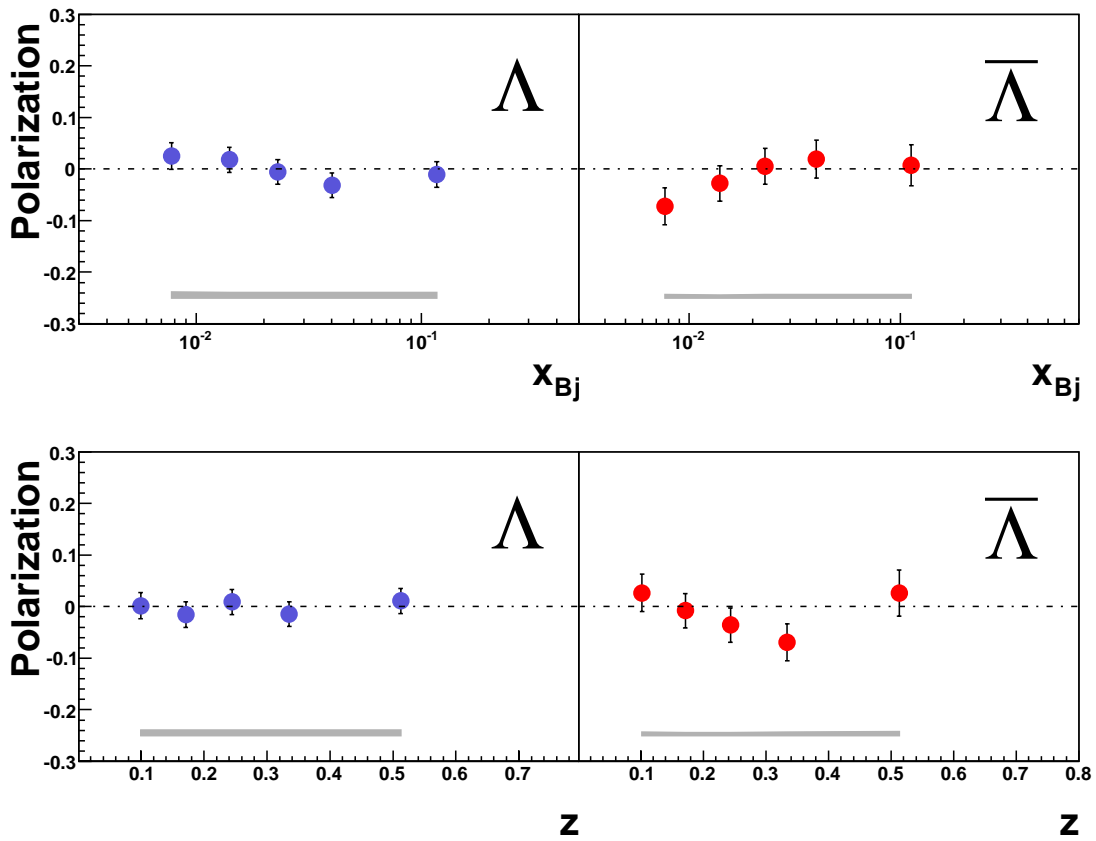
Figure 5.15: Λ and $\overline{\Lambda}$ polarizations with statistical errors as a function of x_{Bj} and z in the 2007 data. The lower band shows the upper limit of the systematic error, estimated by the pulls distribution of false polarizations.

Chapter 6

Discussion of Results

The QCD-corrected Quark Parton Model has been introduced in Section 2.3. In this model, the Λ^0 hyperon is an isospin singlet with quark content uds. Its spin is entirely determined by the strange quark while the u and d quarks are an unpolarized, spinless (singlet) ud pair: $\Delta u + \Delta d = 0$, $\Delta s = 1$, where Δq $(q = u, d, s)$ is the first moment integral for a given flavour of the spin-dependent quark distribution function $\Delta q(x_{Bj})$, e.g. $\Delta q = \int_0^1 \Delta q(x_{Bj})$ [103]. This picture can very successfully describe the static properties of the baryons.

However, the naive Quark Parton Model fails to explain data on the β-decay of hyperons as well as the polarization of u and d quarks in the proton [5, 30, 104, 105]. Experimentally, it follows from inclusive deep-inelastic lepton-nucleon scattering experiments [29, 30, 106, 107] that the spins of the valence quarks account for merely a fraction of the nucleon spin, while the remaining spin stems from the gluon spin and orbital angular momenta. Important findings about specific contributions to the nucleon spin from various quark flavours have been obtained in semi-inclusive DIS experiments in which a final state hadron is detected in coincidence with a scattered charged lepton [108, 109]. It has been deduced from these experiments that for the **proton**

$$\begin{aligned}
\Delta u + \Delta \overline{u} &= 0.51 \pm 0.02, \\
\Delta d + \Delta \overline{d} &= -0.22 \pm 0.06, \\
\Delta s + \Delta \overline{s} &= -0.01 \pm 0.03,
\end{aligned}$$

with $\Delta \Sigma = 0.28 \pm 0.04$ [109]. Here, $\Delta u, \Delta \overline{u}, \Delta d, \Delta \overline{d}, \Delta s, \Delta \overline{s}$ are helicity contributions of u, d, s, and $u, \overline{u}, d, \overline{d}, s, \overline{s}$ are quarks contributing to the nucleon spin, and $\Delta \Sigma = \Delta u + \Delta \overline{u} + \Delta d + \Delta \overline{d} + \Delta s + \Delta \overline{s}$ is the SU(3)$_f$ singlet term (total contribution to the nucleon spin from the quarks of all the flavours).

Using SU(3)$_f$ symmetry and experimental results for the spin-dependent quark distributions of the proton it has been attempted to reproduce those numbers for other members of the baryon spin-1/2 octet. For the Λ **hyperon** it has been predicted

by Burkardt and Jaffe [110, 111] that

$$\Delta u + \Delta \overline{u} \;\; = \;\; \Delta d + \Delta \overline{d} = -0.23 \pm 0.06,$$
$$\Delta s + \Delta \overline{s} \;\; = \;\; 0.58 \pm 0.07.$$

According to this calculation, the u and d quarks are predominantly polarized oppo-
site to the Λ spin. The deep-inelastic lepton-nucleon scattering data [106] together
with this model suggest that the s quark carries only about 60 % of the Λ spin, while
under consideration of the u and d quark contribution the sum of the quarks carries
about -20 % of the Λ spin. A large part of the baryon spin is assumed to originate
from the sea (i.e., the sea quarks, antiquarks, and gluons) as well as from the orbital
angular momenta of the valence quarks and gluons. Hence, it is necessary to find
a picture which is suitable to describe the spin effects in the quark fragmentation
process. Obviously, the answer to this question is a priori unknown, and should be
investigated in both experiments and theoretical models.

Up to now there exists no model which can successfully describe all observed po-
larization effects. However, the model of DeGrand and Miettinen [112], based on
the Thomas precession effect in the quark recombination picture, is able to predict
the relative signs and magnitudes of numerous polarization measurements. Unfor-
tunately, the model itself is derived for a proton beam and not for a lepton beam
which is required to fully describe the 2007 COMPASS data. No other valid models
for the observed effects have so far been derived. Thus, "despite several theoretical
efforts over the last twenty years or so, theory is left behind and has to make urgent
progress to catch up with the puzzling experimental situation" [54].

Experimentally, the transverse Λ polarization has been investigated with all kinds
of beams and targets. An overview of the experimental situation can be found in
[113] and [114]. However, most of the experiments concerning the Λ polarization
have been concluded using a longitudinally polarized target. Therefore, the theo-
retical models which are developed for Λ polarization so far contain a longitudinal
spin transfer in lepton induced processes [115, 116], whereas no valid theoretical
model has been legitimately introduced for a transversely polarized proton target in
combination with a longitudinally polarized lepton beam in the semi-inclusive DIS
domain. For a transversely polarized ^{6}LiD target with an assumed target polariza-
tion of 80 % and a dilution factor of $f = 1$, an estimate of $P_\Lambda \approx 6$ % at $x_{Bj} \approx$
0.2 has been given in [117], where any sea quark contributions are neglected. This
is the only prediction available for the Λ polarization with a transversely polarized
target. Assuming a scaling of P_Λ which is linear both to the target polarization and
the dilution factor, this corresponds to a predicted $P_\Lambda \approx 1.4$ % for the ^{6}LiD target
with $f = 0.38$ and a transverse target polarization of 50 % which was used during
2002-2004 at the COMPASS experiment. In 2002-2005, the HERMES experiment
employed a transversely polarized H-target with 78 % polarization in their RUN II.
However, analyses from the HERMES collaboration on Λ polarization were so far
published only on data taken on a longitudinally polarized or unpolarized target

and a longitudinally polarized beam. Thus, no direct comparison to this analysis is possible.

When measuring the Λ polarization it might happen that the Λ is not created in direct production but through the decay of a heavier particle, such as $\Sigma^0 \to \Lambda^0 \gamma$, $\Xi \to \Lambda^0 \pi$, $\Sigma^*(1385) \to \Lambda\pi$ or $\Xi^*(1530) \to \Xi\pi \to \Lambda\pi\pi$, which will pollute the primary production mechanism and, thus, the measurement of the Λ polarization because the polarization of the heavier hyperon might be transferred to the Λ. These background effects should be excluded in this analysis by the applied kinematic cuts, i.e. the requirement on the vertex position and decay length, and the cut on the invariant mass of the Λ^0 hyperon. The fraction of the produced Λ^0 which are created in some dominant resonances are estimated in [118].

For the data recorded with a transversely polarized proton target and longitudinally polarized lepton beam as in this analysis, there are two ways how the Λ hyperon might have gained its polarization, namely either the polarization is induced by interaction with the polarized beam or it stems from the polarized quark in the target nucleon. If a struck quark q, originating from a nucleon with polarization P_T, fragments into a Λ hyperon, the corresponding Λ polarization has been quoted in Eq. 2.58 to be

$$P_\Lambda(x_{Bj}, z) \quad \propto \quad \frac{\sum_q e_q^2 \, \Delta_T q(x_{Bj}) \Delta_T D_q^\Lambda(z)}{\sum_q e_q^2 \, q(x_{Bj}) D_q^\Lambda(z)},$$

where e_q is the charge of the quark. $q(x_{Bj})$ and $\Delta_T q(x_{Bj})$ are the unpolarized and transversely polarized quark distribution functions of the nucleon, and $D_q^\Lambda(z)$ and $\Delta_T D_q^\Lambda(z)$ are the unpolarized and transversely polarized fragmentation functions, respectively (see Section 2.6.1). It appears that $\Delta_T q(x_{Bj})$ is coupled to $\Delta_T D_q^\Lambda(z)$, showing different factorizations of x_{Bj} and z [69]. Thus, in order to extract the transversity distribution $\Delta_T q(x_{Bj})$, one has to measure the Λ polarization $P_\Lambda(x_{Bj}, z)$ which allows insight into the convolution of $\Delta_T q(x_{Bj}) \cdot \Delta_T D_q^\Lambda(z)$.

In Fig. 6.1 it can be seen that based on the COMPASS, HERMES and BELLE results, experimental evidence clearly proves the existence of transversity functions $\Delta_T q(x_{Bj})$ with opposite signs for the u and d quark. The transversity distribution for the u quark, $\Delta_T u(x_{Bj})$, is positive with a larger amplitude than the negative transversity distribution for the d quark, $\Delta_T d(x_{Bj})$. Both transversity distributions are significantly smaller than their corresponding Soffer limits. The mean in x_{Bj} covered by this analysis is $\langle x_{Bj} \rangle \approx 0.03$ as was shown previously in Figs. 4.13 and 4.14. However, for the last bin in the x_{Bj} range, the mean x_{Bj} is $\langle x_{Bj}^{last} \rangle \approx 0.1$, which is approximately the x_{Bj} range where the transversity distribution function is expected to peak, as can be seen in Fig. 6.1.

A simplifying ansatz to describe the Λ and $\overline{\Lambda}$ polarizations measured in a proton and deuteron target is to neglect the contributions from the sea s quarks and to
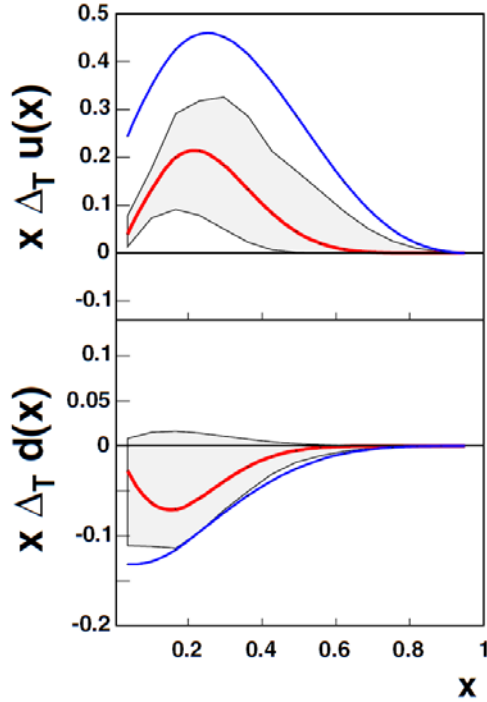
Figure 6.1: The transversity distribution functions for the u and d quark from COMPASS deuteron, HERMES proton and BELLE data [119]. In the top panel $x_{Bj} \cdot \Delta_T u(x_{Bj})$ is shown in red as a function of x_{Bj} with its corresponding statistical uncertainty in grey and $Q^2 = 2.4$ GeV^2; the bottom panel shows $x_{Bj} \cdot \Delta_T d(x_{Bj})$ in the same way. Both plots show the respective Soffer limit $|\Delta_T q(x_{Bj})| \leq \frac{1}{2}[q(x_{Bj}) + \Delta q(x_{Bj})]$ in blue [47], which is explained in Eq. 2.39.

introduce favoured and disfavoured fragmentation functions. The favoured fragmentation functions quantify the fragmentation of the u, d and s quarks into a Λ hyperon (uds), while the disfavoured fragmentation functions describe the u, d and s quarks fragmenting into a $\overline{\Lambda}$ hyperon ($\overline{u}\overline{d}\overline{s}$). The u quark carries a charge $+2/3e$ while the d quark and the s quark have a charge of $-1/3e$, therefore, the u quark contribution is further enhanced by its charge. The isospin invariance of the proton and neutron distribution functions [120] state that the following relations hold

$$
\begin{aligned}
u_{proton}(x_{Bj}) &= d_{neutron}(x_{Bj}) \equiv u(x_{Bj}) \\
d_{proton}(x_{Bj}) &= u_{neutron}(x_{Bj}) \equiv d(x_{Bj}).
\end{aligned}
$$

It has to be noted that the u and d distribution functions contain the contributions both from the valence u and d quarks and from the sea u and d quarks. Differentiating the processes, thus, splits the above expression for the Λ and $\overline{\Lambda}$ polarizations

in a **proton target** to be

$$P_\Lambda(x_{Bj}, z) \quad \propto \quad \frac{4\Delta_T u(x_{Bj}) + \Delta_T d(x_{Bj})}{4u(x_{Bj}) + d(x_{Bj})} \frac{\Delta_T D^\Lambda_{fav}}{D^\Lambda_{fav}},$$

$$P_{\overline{\Lambda}}(x_{Bj}, z) \quad \propto \quad \frac{4\Delta_T u(x_{Bj}) + \Delta_T d(x_{Bj})}{4u(x_{Bj}) + d(x_{Bj})} \frac{\Delta_T D^\Lambda_{dis}}{D^\Lambda_{dis}},$$

and in a **deuteron target** (noticing that a deuteron consists of a proton and a neutron) to be

$$P_\Lambda(x_{Bj}, z) \quad \propto \quad \frac{\Delta_T u(x_{Bj}) + \Delta_T d(x_{Bj})}{u(x_{Bj}) + d(x_{Bj})} \frac{\Delta_T D^\Lambda_{fav}}{D^\Lambda_{fav}},$$

$$P_{\overline{\Lambda}}(x_{Bj}, z) \quad \propto \quad \frac{\Delta_T u(x_{Bj}) + \Delta_T d(x_{Bj})}{u(x_{Bj}) + d(x_{Bj})} \frac{\Delta_T D^\Lambda_{dis}}{D^\Lambda_{dis}}.$$
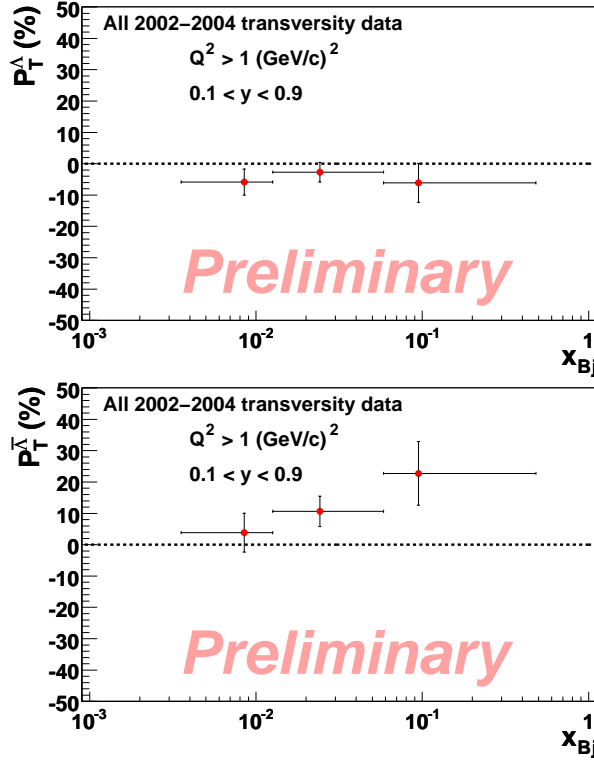
Figure 6.2: Λ and $\overline{\Lambda}$ polarizations with statistical errors as a function of x_{Bj} in the 2002-2004 COMPASS data on a transversely polarized deuteron target with $Q^2 > 1 \ (\text{GeV/c})^2$ and $0.1 < y < 0.9$ [121].

Since the proton is composed of two u quarks and one d quark, therefore, being dominated by the u quark contribution, the transverse Λ polarization is assumed to have a value different from zero if $\Delta_T D^\Lambda_u(z) \neq 0$, due to the fact that a positive $\Delta_T u(x_{Bj})$ is measured and that $P_\Lambda \propto \Delta_T u(x_{Bj}) \cdot \Delta_T D^\Lambda_u(z)$. Contrary to the proton,

in the deuteron both flavours u and d are present in equal numbers, therefore, the polarization P_Λ is anticipated to be approximately zero when measured with a deuteron target and disregarding the influence of the quark charge. Accordingly, the Λ and $\overline{\Lambda}$ polarizations for the transversely polarized deuteron target at COMPASS in the 2002-2004 data have been found to be compatible with zero, as can be seen in Fig. 6.2 as a function of x_{Bj} [121, 122, 123]. Generally, it seems logical that there is no polarization expected for particles which share no quarks with the polarized target nucleon. Thus, for the $\overline{\Lambda}$ the polarization is naively expected to be small, because it shares no valence quark with either the target nucleon or the beam. Surprisingly, there is a slight tendency of a positive polarization for the $\overline{\Lambda}$ hyperon at high x_{Bj}. The small deviation of $P_{\overline{\Lambda}}$ is, nevertheless, statistically compatible with the anticipated value of zero.
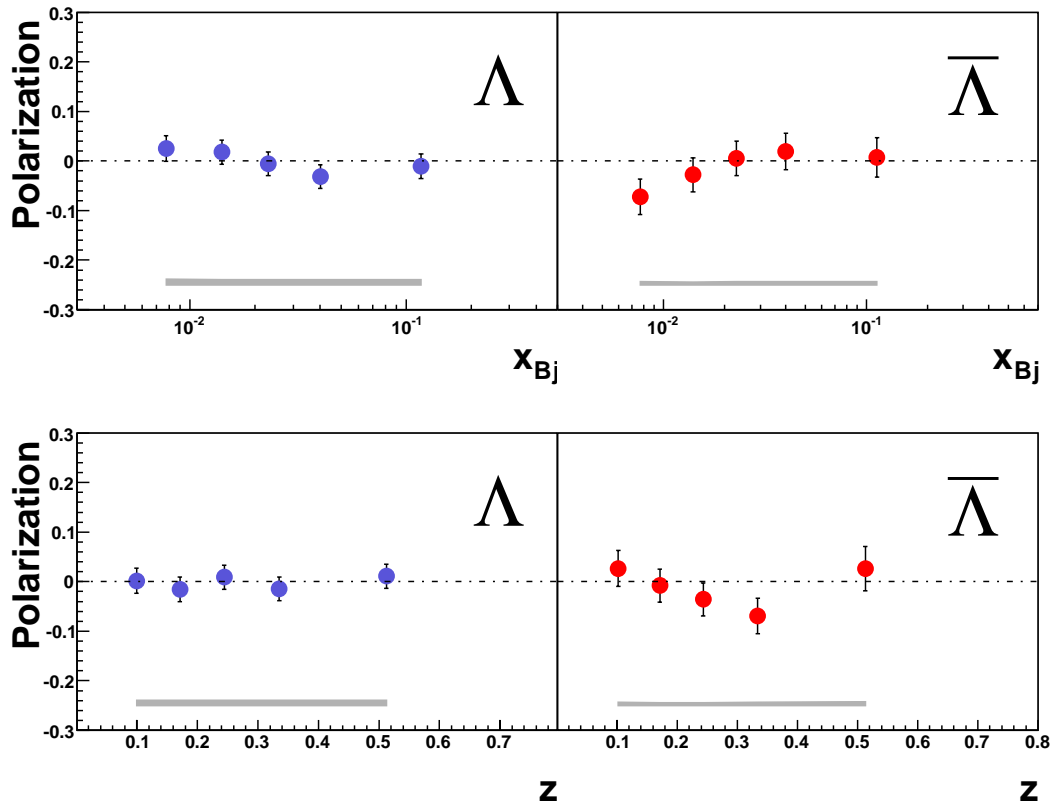
Figure 6.3: Λ and $\overline{\Lambda}$ polarizations with statistical errors as a function of x_{Bj} and z in the 2007 COMPASS data on a transversely polarized proton target with $Q^2 > 1$ $(\text{GeV/c})^2$ and $0.1 < y < 0.9$. The lower band shows the upper limit of the systematic error, estimated by the pulls distribution of false polarizations (same as Fig. 5.15).

For the 2007 data on the proton target a positive polarization P_Λ was expected to be measured. However, the COMPASS data on the proton target and the measurement on the deuteron target both show no proof for transverse Λ and $\overline{\Lambda}$ polarizations within their respective statistical errors. The Λ and $\overline{\Lambda}$ polarizations determined in

this analysis are shown in Fig. 6.3 as a function of x_{Bj} and z.

A possible contribution from the sea s quarks to the Λ polarization can be neglected when considering that they contribute symmetrically to the proton and the deuteron [120],

$$s_{proton}(x_{Bj}) = s_{neutron}(x_{Bj}) = \overline{s}_{proton}(x_{Bj}) = \overline{s}_{neutron}(x_{Bj}). \qquad (6.1)$$

Thus, it can be seen that a possible influence from the sea s quarks towards a measurable polarization difference between the proton and deuteron target can be neglected. The same reasoning applies for the $\overline{\Lambda}$ polarization.

Since the transversity distributions measured at COMPASS, HERMES and BELLE show a value different from zero, the vanishing Λ and $\overline{\Lambda}$ polarizations seem to prove that the fragmentation function $\Delta_T D_q^\Lambda(z)$ to which the transversity distribution $\Delta_T q(x_{Bj})$ is coupled in this process is very small. A vanishing $\Delta_T D_q^\Lambda(z)$ will generate an extremely small polarization P_Λ due to the relation $P_\Lambda \propto \Delta_T q(x_{Bj}) \cdot \Delta_T D_q^\Lambda(z)$. Even if the transversity distributions show quite a large value, this quantity is nevertheless unaccessible via the channel of Λ polarization.

In [124] the transverse Λ polarization was calculated in a phenomenological approach with a numerical parameterization of $\Delta_T D_q^\Lambda(z)$. The conclusions of this model are transverse Λ and $\overline{\Lambda}$ polarizations which are negative and decrease further with increasing z down to a maximum polarization value of -0.2 to -0.6, depending on the parametrization used for the polarizing fragmentation function. Thus, a non-zero polarization is expected for $z > 0.4$. The recorded COMPASS data display a mean of $\langle z \rangle = 0.26$, thus, the mean z value is below 0.4, as is shown in Figs. 4.13 and 4.14. The last bin in z at $\langle z^{last} \rangle \approx 0.52$ accumulates all events with $z > 0.4$ integrated over the whole x_{Bj} range. For the $\langle z^{last} \rangle$ bin, the polarizations of Λ and $\overline{\Lambda}$ are compatible with zero as well. Unfortunately, a two-dimensional cut on the interesting x_{Bj} and z region is not feasible due to the limited statistics. More accurate data are needed to investigate this channel in more detail. This might be a good opportunity for the experiments at the Jefferson Laboratories which cover the high x_{Bj} region [125].

The conclusion that can be drawn from the presented analysis and its results on the transverse Λ and $\overline{\Lambda}$ polarizations is that the fragmentation function $\Delta_T D_q^\Lambda(z)$ seems to be too small to be utilized in an attempt to measure the transversity distributions $\Delta_T q(x_{Bj})$. Therefore, this channel seems not recommendable to investigate transversity distributions with a high precision at this stage. To summarize, in this channel there are too large uncertainties in the quark to Λ fragmentation function and, therefore, it is now deemed more urgent to measure the Λ fragmentation functions before using the Λ fragmentation to probe the quark content of the nucleon [111, 126, 127].

Chapter 7

Summary and Outlook

This thesis concludes an analysis on the transverse polarization of Λ and $\overline{\Lambda}$ hyperons produced in a deep-inelastic scattering process. The immediate aim was to relate the Λ and $\overline{\Lambda}$ polarization P_Λ to the transversity function $\Delta_T q(x_{Bj})$. In a larger frame, any knowledge that can be gained about $\Delta_T q(x_{Bj})$ enhances the understanding of the spin structure of the nucleon which yet lacks completion.

The systematic investigation of the Λ hyperon polarization is interesting due to several reasons: The most striking feature is the so-called "self-analyzing" weak decay of the Λ hyperon which shows a rather large asymmetry of $\alpha = 0.64$, where the angular distribution of its daughter particles is strictly correlated to the Λ hyperon polarization. Thus, the Λ polarization can be determined in experiments by measuring the angular distribution of the decay products. The experimentally easily accessible decay $\Lambda \to p\pi^-$ has a sufficiently high branching ratio of 64 %. Also, the Λ^0 is the lightest hyperon and, thus, produced in abundant numbers.

The Λ polarization P_Λ is directly correlated to a convolution of the transversity function $\Delta_T q(x_{Bj})$ and the fragmentation function $\Delta_T D_q^\Lambda(z)$,

$$P_\Lambda \propto \Delta_T q(x_{Bj}) \cdot \Delta_T D_q^\Lambda(z).$$

By finding P_Λ we gain knowledge about these convoluted distributions, which show different factorizations of the Bjorken scaling variable x_{Bj} and the fraction of the virtual photon energy carried by a produced hadron z, respectively. An aim of this thesis was to extract a possible Λ and $\overline{\Lambda}$ polarization and to investigate the x_{Bj} and z dependence to disentangle the contributions of the transversity and fragmentation functions.

For this analysis, the data of the COMPASS experiment were studied which were recorded in 2007 with a longitudinally polarized 160 GeV muon beam and a transversely polarized proton (NH$_3$) target. Symmetry arguments of the COMPASS apparatus are employed in a geometric-mean method to rid the data of acceptance effects of the spectrometer. The data were compared in period pairs of alternating

target cell spin orientations: each period of ↑↓↑ and ↓↑↓ target polarization was used to extract the polarization of the Λ or $\overline{\Lambda}$ hyperons which are produced through lepton-nucleon SIDIS scattering. The Λ and $\overline{\Lambda}$ events were selected through cuts on the kinematic signature of the Λ decay $\Lambda \to p\pi^-$. Consecutively, a novel veto condition of particle identification information from the RICH detector was applied to further reduce the background while maintaining the number of Λ events. This enabled a fitting procedure on the Λ invariant mass distribution which results in much smaller statistical errors. The Λ and $\overline{\Lambda}$ polarizations are measured in the kinematic region $Q^2 > 1$ $(\text{GeV/c})^2$, where the DIS events are able to probe the spin transfer from a polarized quark fragmenting into a Λ hyperon. The presented analysis contains a final data set of $\approx 105{,}000$ Λ and $\approx 50{,}000$ $\overline{\Lambda}$ hyperons. Several systematic tests are performed to ensure a stable condition during all subperiods of the data taking in 2007 and to give confidence that the behaviour of the apparatus is consistent and well understood.

The Λ and $\overline{\Lambda}$ polarizations P_Λ extracted from the 2007 proton transversity data of the COMPASS experiment are compatible with zero within their statistical errors, for both the investigated kinematic ranges of x_{Bj} and z. It has been demonstrated that the systematic errors are always smaller than the respective statistical errors. Thus, no different behaviour of either $\Delta_T q(x_{Bj})$ or $\Delta_T D_q^\Lambda(z)$ can be extracted via the channel of Λ polarization. It is experimentally established that the transversity distribution for the u quark, $\Delta_T u(x_{Bj})$, has a positive value, while its counterpart for the d quark, $\Delta_T d(x_{Bj})$ shows a negative value [119], both of which are different from zero. In a proton target, consisting of u and d quarks, the abundance of the u quark dominates over the smaller contribution of d quarks, especially when taking the squared quark charges into account. Due to this fact a positive absolute value of the convolution $\Delta_T u(x_{Bj}) \cdot \Delta_T D_q^\Lambda(z)$ was expected, which in turn led to the anticipation of a measurable and non-zero value of P_Λ. The present result of the Λ polarization P_Λ measured at the proton target which is compatible with zero within its statistical errors in combination with a P_Λ measured with a deuteron target also showing no polarization [121] leads to the conclusion that the distribution function $\Delta_T D_q^\Lambda(z)$ must be very small. As of the present status, it is not feasible to apply the measurement of P_Λ towards a high-precision extraction of $\Delta_T q(x_{Bj})$. In fact, the recommendation which is drawn from the result of the presented analysis is that a thorough investigation on $\Delta_T D_q^\Lambda(z)$ is needed before the measurement of P_Λ can possibly be extended in a future attempt to extract the transversity distribution $\Delta_T q(x_{Bj})$.

Bibliography

[1] M. M. Gell-Mann, A schematic model of baryons and mesons, Phys. Lett. 8 (1964) 214

[2] G. Zweig, An SU(3) Model for Strong Interaction Symmetry and its Breaking II, CERN-8419-TH-412 (1964)

[3] R. P. Feynman, Very high-energy collisions of hadrons, Phys. Rev. Lett. 23 (1969) 1415

[4] J. Ashman et al., [EMC Collaboration], Nucl. Phys. B 328 (1989) 1

[5] J. Ashman et al. [EMC Collaboration], A measurement of the spin asymmetry and determination of the structure function g_1 in deep-inelastic muon-proton scattering, Phys. Lett. B 206 (1988) 364

[6] R. L. Jaffe and A. Manohar, The g_1 problem: Deep-inelastic electron scattering and the spin of the proton, Nucl. Phys. B 337 (1990) 509

[7] A. Airapetian et al., [HERMES Collaboration], Phys. Rev. D 71 (2005) 012003

[8] G. Bunce et al., Λ^0 hyperon polarization in inclusive production by 300 GeV protons on Beryllium, Phys. Rev. Lett. 36 (1976) 1113

[9] J. P. Ralston and D. E. Soper, Nucl. Phys. B 152 (1979) 109

[10] X. Ji and R. L. Jaffe, Phys. Rev. Lett. 67 (1991) 552

[11] X. Artru and M. Mekhfi, Z. Phys. C 45 (1990) 669

[12] D. Kang, Longitudinal Λ and $\overline{\Lambda}$ polarization at the COMPASS experiment, PhD thesis, Albert-Ludwigs-University Freiburg (2007)

[13] M. Anselmino, A. Efremov and E. Leader, The theory and phenomenology of polarized deep-inelastic scattering, Phys. Rep. 261 (1995) 124

[14] F. Halzen and A. D. Martin, Quarks and Leptons: Introduction Course in Modern Particle Physics, Wiley (1983)

[15] R. P. Feynman, Proceedings of the 3rd Topical Conference on High Energy Collisions of Hadrons, Stony Brook, N.Y. (1969)

[16] J. D. Bjorken and E. A. Paschos, Inelastic Electron-Proton and γ-Proton Scattering and the Structure of the Nucleon, Phys. Rev. 185, 1975-1982 (1969)

[17] C. G. Callan and S. J. Gross, High-energy electroproduction and the constitution of the electric current, Phys. Rev. Lett. 22 (1969) 156

[18] C. Adloff et al. [H1 Collaboration], Deep-inelastic inclusive ep scattering at low x and a determination of α_s, Phys. Rev. Lett. 22 (1969) 156

[19] S. Chekanov et al. [ZEUS Collaboration], Measurement of the neutral current cross section and F_2 structure function for deep-inelastic e^+p scattering at HERA, Eur. Phys. J. C 21 (2001) 443

[20] A. C. Benvenuti et al. [BCDMS Collaboration], A high statistics measurement of the deuteron structure functions $F_2(x, Q^2)$ and R from deep-inelastic muon scattering at high Q^2, Phys. Lett. B 237 (1990) 592

[21] L. W. Whitlow et al. [SLAC Collaboration], Precise measurements of the proton and deuteron structure functions from a global analysis of the SLAC deep-inelastic electron-scattering cross sections, Phys. Lett. B 282 (1992) 475

[22] M. R. Adams et al. [Fermilab E665 Collaboration], Proton and deuteron structure functions in muon scattering at 470 GeV, Phys. Rev. D 54 (1996) 3006

[23] M. Arneodo et al. [The New Muon Collaboration], Measurement of the proton and deuteron structure functions, F_2^p and F_2^d, and of the ratio σ_L/σ_T, Nucl. Phys. B 483 (1997) 3

[24] Particle Data Group. Review of particle physics, Phys. Lett. B 592 (2004)

[25] T. Pussieux and R. Windmolders, A collection of formulas for spin-dependent deep-inelastic scattering, Note SMC-93/16 (1996)

[26] G. Baum et al. [E130 Collaboration], New measurement of deep-inelastic $e - p$ asymmetries, Phys. Rev. Lett. 51 (1983) 1135

[27] K. Abe et al. [E143 Collaboration], Measurement of the proton and deuteron spin structure functions g_1 and g_2, Phys. Rev. D 58 (1998) 112003

[28] P. L. Anthony et al. [E155 Collaboration], Measurement of the Q^2-dependence of the proton and neutron spin structure function g_1^p and g_1^n, Phys. Lett. B 493 (2000) 19

[29] B. Adeva et al. [Spin Muon Collaboration], Spin asymmetries A_1 and structure functions g_1 of the proton and the deuteron from polarized high energy muon scattering, Phys. Rev. D 58 (1998) 112001

[30] A. Airapetian et al. [HERMES Collaboration], Measurement of the proton spin structure function g_1^p with a pure hydrogen target, Phys. Lett. B 442 (1998) 484

[31] M. Hirai, S. Kumano abd N. Saito [Asymmetry Analysis Collaboration], Determination of polarized parton distribution functions with recent data on polarization asymmetries, Phys. Rev. D 74 (2006) 014015

[32] P. L. Anthony et al. [E142 Collaboration], Deep-inelastic scattering of polarized electrons by polarized ^{3}He and the study of the neutron spin structure, Phys. Rev. D 54 (1996) 6620

[33] K. Ackerstaff et al. [HERMES Collaboration], Measurement of the neutron spin structure function g_1^n with a polarized ^{3}He internal target, Phys. Lett. B 404 (1997) 383

[34] K. Abe et al. [E154 Collaboration], Precision determination of the neutron spin structure function g_1^n, Phys. Rev. Lett. 79 (1997) 26

[35] X. Zheng et al. [Jefferson Lab Hall A Collaboration], Precision measurement of the neutron spin asymmetries and spin-dependent structure functions in the valence quark region, Phys. Rev. C 70 (2004) 065207

[36] R. L. Jaffe and X. Ji, Studies of the transverse spin-dependent structure function $g_2(x, Q^2)$, Phys. Rev. D 43 (1991) 724

[37] P. L. Anthony et al. [E155 Collaboration], Measurement of the proton and deuteron spin structure functions g_2 and asymmetry A_2, Phys. Lett. B 458 (1999) 529

[38] K. Abe et al. [E154 Collaboration], Measurement of the neutron spin structure function g_2^n and asymmetry A_2^n, Phys. Lett. B 404 (1997) 377

[39] Y. L. Dokshitzer, Calculation of the structure functions for deep-inelastic scattering and e^+e^- annihilation by perturbation theory in Quantum Chromodynamics, Sov. Phys. JETP 46 (1977) 641

[40] V. N. Gribov and L. N. Lipatov, Deep-inelastic ep scattering in perturbation theory, Sov. J. Nucl. Phys. 15 (1972) 438

[41] G. Altarelli and G. Parisi, Asymptotic freedom in parton language, Nucl. Phys. B 126 (1977) 298

[42] G. Bunce et al., Part. World 3 (1993) 1

[43] B. Vuaridel et al. [The HELP Collaboration], CERN Reports LEPC 93-14, LEPC/P7 (1993)

[44] O. Nachtmann, Elementarteilchenphysik, Phänomene und Konzepte, Vieweg, Braunschweig (1991)

[45] V. Barone and P. G. Ratcliff, Transverse spin physics, World Scientific (2003)

[46] R. L. Jaffe, Can transversity be measured? (1997) [arXiv:hep-ph/9710465 V2]

[47] J. Soffer, Phys. Rev. Lett. 74 (1995) 1292 [arXiv:hep-ph/9409254]

[48] A. Lesnik et al., Observation of a difference between polarization and analyzing power in Λ^0 production, Phys. Rev. Lett. 35 (1975) 770

[49] K. Abe et al., Inclusive Λ^0 polarization in proton-nucleus collision at 12 GeV, Phys. Rev. D 34 (1986) 1950

[50] A. M. Smith et al. [R608 Collaboration], Λ^0 polarization in proton-proton interaction from $\sqrt{s} = 31$ to 62 GeV, Phys. Lett. B 185 (1987) 209

[51] M. Wiesmann, A first measurement of the transverse polarization of Λ^0 hyperons from quasi-real photo-production, PhD thesis, Technische Universität München (2004)

[52] M. Anselmino, D. Boer, U. D'Alesio, F. Murgia, Λ polarization from unpolarized quark fragmentation, Phys. Rev. D 63 (2001) 054029

[53] D. Hui and L. Zou-Tang, Hyperon polarization in different inclusive production processes in unpolarized high energy hadron-hadron collisions, Phys. Rev. D 70 (2004) 014019

[54] J. Soffer, Is the riddle of the hyperon polarization solved?, In Batavia 1999, Hyperon physics (Hyperon99), arXiv:hep-ph/9911373 (1999)

[55] A. Bravar, Experimental overview of spin effects in hadronic interactions at high energies, 13th Symposium on High Energy Spin Physics [SPIN98] Proceedings (1998)

[56] V. V. Abramov, Universal scaling behaviour of the transverse polarization for inclusively produced hyperons in hadron-hadron collisions, arXiv:hep-ph/0111128 (2001)

[57] D. H. Perkins, Introduction to High Energy Physics, Addison Wesley (1983)

[58] B. E. Bonner et al., Spin-parameter measurements in Λ and K_S production, Phys. Rev. D 38 (1988) 729

[59] F. Baldracchini et al., Fortschritte der Physik 30 (1981) 505

[60] X. Artru and M. Mekhfi, Transversely polarized parton densities, their evolution and their measurement, Z. Phys. C 45 (1990) 669

[61] L. Chun-Xiu and Z. Liang, Spin structure and longitudinal polarization of a hyperon in e^+e^- annihilation at high energies, Phys. Rev. D 62 (2000) 094001

[62] V. N. Gribov and L. N. Lipatov, Deep-inelastic electron scattering in perturbation theory, Phys. Lett. B 37 (1971) 78

[63] V. Barone, A. Drago and B. Ma, Connection between distribution and fragmentation functions, Phys. Rev. C 62 (2000) 062201

[64] B. Ma, I. Schmidt, J. Soffer and J. Yang, Phenomenological relation between distribution and fragmentation functions, Phys. Lett. B 547 (2002) 245

[65] M. Anselmino and F. Murgia, Spin effects in the fragmentation of a transversely polarized quark, Phys. Lett. B 483, (2000) 74-86

[66] D. Kang and T. Negrini, internal COMPASS Note 2008-04 (2008)

[67] A. Ferrero and D. Kang, internal COMPASS Note 2006-09 (2006)

[68] M. Anselmino et al., Phys. Lett. B 481 (2000) 74

[69] M. Anselmino, Transversity and Lambda polarization, Proceedings of the Workshop on Future Physics @ COMPASS (September 26-27, 2002), CERN

[70] F. Hinterberger, Comparison of Geometric Mean Method and Double Ratio Method, internal COMPASS note (November 15, 2005)

[71] The COMPASS collaboration. A proposal for a Common Muon and Proton Apparatus for Structure and Spectroscopy, CERN-SPSLC-96-14 (1996)

[72] P. Abbon et al. [COMPASS Collaboration], The COMPASS Experiment at CERN, Nucl. Instrum. Meth. in Physics Research A 577, 455-518 (2007) [arXiv:hep-ex/0703049]

[73] D. Adams et al., [SMC Collaboration] Measurement of the SMC muon beam polarisation using the asymmetry in the elastic scattering off polarised electrons, Nucl. Instru. Meth. A 443 (2000) 1

[74] J. Ball et al., First results of the large COMPASS ^{6}LiD polarized target, Nucl. Instru. Meth. A 498 (2003) 101

[75] K. Kondo, The polarization measurement and the feature investigation of the COMPASS ^{6}LiD target, PhD thesis, Nagoya University (2003)

[76] K. Kondo et al., Polarization measurement in the COMPASS polarized target, Nucl. Instru. Meth. A 526 (2004) 70

[77] J. Bisplinghoff et al., A scintillating fibre hodoscope for high rate applications, Nucl. Instru. Meth. A 490 (2002) 101

[78] H. Angerer et al., Present status of silicon detectors in COMPASS, Nucl. Instru. Meth. A 512 (2003) 229

[79] C. Bernet et al., The $40 \times 40 cm^2$ gaseous microstrip detector Micromegas for the high-luminosity COMPASS experiment at CERN, Nucl. Instru. Meth. A 536 (2005) 61

[80] C. Altunbas et al., Construction, test, commissioning of the triple-gem tracking detector for COMPASS, Nucl. Instru. Meth. A 490 (2002) 177

[81] S. Panebianco, Performances of Drift Chambers and Micromegas in 2003, COMPASS Collaboration Meeting, Lissabon (October 2003)

[82] V. N. Bychkov et al., The large size straw drift chambers of the COMPASS experiment, Nucl. Instru. Meth. A 556 (2006) 66

[83] A. Amoroso et al., The front-end electronics for the COMPASS MWPCs, Nucl. Instru. Meth. A 518 (2004) 495

[84] M. Leberig, W45 Calibration and Resolution, COMPASS Analysis Meeting, CERN, Geneva (May 2004)

[85] O. Gavrishchuk et al., Calorimeter for Hadron Detection in the Energy Range 10-100 GeV, Tech. Rep. JINR D13-2004-186, Dubna (2004)

[86] N. V. Vlasov et al., A Calorimeter for detecting hadrons with energies 10-100 GeV, Instruments and Experimental Techniques 49 (2006) 41

[87] A. V. Dolgopolov et al., Results of a beam test of the combined lead glass and PWO cells detector for the COMPASS electromagnetic calorimeter, Nucl. Instru. Meth. A 420 (1999) 20

[88] V. Polyakov, private communication

[89] E. Iarocci et al., Plastic streamer tubes and their applications in high energy physics, Nucl. Instru. Meth. 217 (1983) 30

[90] F. Sozzi, Measurement of transverse spin effects in COMPASS, PhD thesis, University of Trieste (2007)

[91] E. Albrecht et al., Status and characterisation of COMPASS RICH-1, Nucl. Instru. Meth. A 553 (2005) 215

[92] C. Bernet et al., The COMPASS trigger system for muon scattering, Nucl. Instru. Meth. A 550 (2005) 217

[93] H. Fischer et al., The DAQ of the COMPASS Experiment, IEEE Trans. Nucl. Sci. 49 (2002) 443

[94] B. Gobbo et al., CORAL webpage, http://coral.web.cern.ch/coral/

[95] PHAST webpage, http://ges.home.cern.ch/ges/phast/

[96] ROOT webpage, http://root.cern.ch/

[97] B. Grube, A trigger control system for COMPASS and a measurement of the Transverse Polarisation of Λ and Ξ Hyperons from Quasi-Real Photo-Production, PhD thesis, Technische Universität München (2006)

[98] H. Wollny, Transversity group communication (March 4, 2009)

[99] R. Armenteros and J. Podolanski, Analysis of V-events, Philos. Mag. 45 (1954) 13

[100] E. Byckling and K. Kajantie, Particle Kinematics, J. Wiley & Sons (1972)

[101] F. James, Statistical Methods in Experimental Physics, 2nd Edition, World Scientific Publishing Company (2006)

[102] J. Bisplinghoff et al., Collins and Sivers asymmetries from COMPASS 2003/2004 transverse run, internal COMPASS note (March 27, 2006)

[103] C. Boros and Z. Liang, Phys. Rev. D 57, 4491 (1998)

[104] K. Abe et al., [E143 Collaboration], Phys. Rev. Lett. 74, 346 (1995)

[105] D. Adams et al., [SMC Collaboration], Phys. Lett. B 329, 399 (1994)

[106] For a review of data, see e.g., G. K. Mallot, in Proceedings of the 12th International Symposium on Spin Physics, Amsterdam, 1996, edited by C. W. de Jager et al. (World Scientific, Singapore, 1997), p. 44

[107] P. L. Anthony et al., E154 Collaboration, Phys. Rev. Lett. 79, 26 (1997)

[108] D. Adams et al., SMC collaboration, Phys. Lett. B420, 180 (1998)

[109] K. Ackerstaff et al., HERMES collaboration, Phys. Lett. B464, 123 (1999)

[110] M. Burkard and R. L. Jaffe, Phys. Rev. Lett. 70, 2537 (1993)

[111] R. L. Jaffe, Phys. Rev. D 54, 6581 (1996)

[112] T. A. DeGrand and H. I. Miettinen, Phys. Rev. D 23, 1227 (1981)

[113] A. D. Panagiotou, preprint CERN-EP/89-131 (1989)

[114] A. D. Panagiotou, Int. J. Mod. Phys. A5, 1197 (1990)

[115] A. Kotzinian, A. Bravar, D. von Harrach, Λ and $\overline{\Lambda}$ polarization in lepton induced processes, Eur. Phys. J. C 2, 329-337 (1998)

[116] J. Ellis, A. Kotzinian, D. V. Naumov, Intrinsic polarized strangeness and Λ^0 polarization in deep-inleastic production, Eur. Phys. J. C 25, 603-613 (2002)

[117] R. A. Kunne et al., LNS-Ph-93-01 (1993)

[118] Ch. Liu, Q. Xu, and Z. Liang, Hyperon polarization in semi-inclusive deeply inelastic lepton-nucleon scattering at high energy, Phys. Rev. D64 (2001) 073004

[119] M. Anselmino et al., Transversity and Collins functions from SIDIS and e^+e^- data, Phys. Rev. D 75, 054032 (2007)

[120] A. Bettini, Introduction to elementary particle physics, Cambridge University Press (2008), p. 208

[121] A. Ferrero, Proceedings of SPIN06, Kyoto, Japan (October 2-7, 2006)

[122] A. Ferrero (on behalf of the COMPASS Collaboration), Proceedings of the International Workshop On Transverse Polarization Phenomena In Hard Processes (*Transversity 2005*), Como, Italy (September 7-10, 2005), Eds. V. Barone and P.G. Ratcliffe, (World Scientific, 2006) p. 61

[123] D. Kang, Proceedings of SPIN-Praha-2008 - Advanced Studies Institute, Symmetries and Spin, Prague, Czech Republic (July 20-26, 2008), to be published in Eur. Phys. J.

[124] M. Anselmino et al., Phys. Rev. D 65 (2002) 114014

[125] H. Avakian et al., JLab LOI 12-06-108 (2008)

[126] B. Ma et al., The quark-antiquark asymmetry of the nucleon sea from Λ and $\overline{\Lambda}$ fragmentation, Phys. Lett. B 488 (2000) 254-260

[127] T. Negrini, in Proceedings of the 18th International Symposium on Spin Physics, Charlottesville (October 6-11, 2008), edited by D. G. Crabb et al. (American Institute of Physics, 2009), ISBN 978-0735406865

Acknowledgements

Working on this thesis has been a great experience, and I would like to thank those people who made this thesis possible and the time spent on it productive and enjoyable.

First and foremost I am very grateful to my supervisor, Prof. Jens Bisplinghoff, whose encouragement and guidance from the initial to the final level enabled me to develop an understanding of the subject. He has made available his support in a number of ways, and I owe my deepest gratitude to Prof. Bisplinghoff for giving me the opportunity to work on my thesis in his group as well as for kindling my enthusiasm to conduct this research project. One simply could not wish for a better or friendlier supervisor.

Special thanks are due to my co-advisor Prof. Karl Maier for his positive and constructive advice. I greatly appreciate his élan and his kind willingness to spend time and effort on my thesis.

It is an honor for me to have Prof. Hans-Werner Hammer and Prof. Pavel Kroupa in my PhD committee, and I would like to thank both of them for their interest in my thesis.

This work would not have been possible without the support and encouragement of my postdoc, Dr. Rainer Joosten. He has been abundantly helpful in many ways, and I deeply thank him for his meticulous corrections of my thesis and his distinctive way to teach me everything he deemed important whilst allowing me the room to work in my own way.

I would like to show my gratitude to Prof. Herbert Hübel for his tremendous support. During the past years I benefited from his suggestions and I am very thankful for the friendly atmosphere during all our conversations.

This thesis profited from the numerous ways in which all members and colleagues from the HISKP contributed to my daily routine and to a pleasant atmosphere. I thank the COMPASS group in the HISKP for being encouraging and helpful colleagues. I offer my sincerest gratitude especially to Dr. Gunnar Mertler for his insightful recommendations and to Prof. Kai-Thomas Brinkmann for his suppport.